EFFECT OF BUILD DIRECTION ON CRACK GROWTH BEHAVIOR OF Ti6Al4V ALLOY MANUFACTURED BY ELECTRON BEAM MELTING

A THESIS SUBMITTED TO
THE GRADUATE SCHOOL OF NATURAL AND APPLIED SCIENCES
OF
MIDDLE EAST TECHNICAL UNIVERSITY

BY

FEYZİYE ÇALIK

IN PARTIAL FULFILLMENT OF THE REQUIREMENTS
FOR
THE DEGREE OF MASTER OF SCIENCE
IN
METALLURGICAL AND MATERIALS ENGINEERING

DECEMBER 2022

Approval of the thesis:

EFFECT OF BUILD DIRECTION ON CRACK GROWTH BEHAVIOR OF Ti6Al4V ALLOY MANUFACTURED BY ELECTRON BEAM MELTING

submitted by **FEYZİYE ÇALIK** in partial fulfillment of the requirements for the degree of **Master of Science** i**n Metallurgical and Materials Engineering, Middle East Technical University** by,

Prof. Dr. Halil Kalıpçılar
Dean, Graduate School of **Natural and Applied Sciences** _____

Prof. Dr. Ali Kalkanlı
Head of the Department, **Metallurgical and Materials Engineering** _____

Prof. Dr.Rıza Gürbüz
Supervisor, **Metallurgical and Materials Engineering** _____

Examining Committee Members:

Prof. Dr. Bilgehan Ögel
Metallurgical and Materials Eng, METU _____

Prof. Dr. Rıza Gürbüz
Metallurgical and Materials Eng, METU _____

Prof. Dr. M. Kadri Aydınol
Metallurgical and Materials Engineering, METU _____

Prof. Dr. Ziya Esen
Materials Science and Eng., Çankaya Uni. _____

Assoc.Prof. Dr. Caner Şimşir
Metallurgical and Materials Engineering, METU _____

Date: 01.12.2022

I hereby declare that all information in this document has been obtained and presented in accordance with academic rules and ethical conduct. I also declare that, as required by these rules and conduct, I have fully cited and referenced all material and results that are not original to this work.

Name Last name: Feyziye Çalık

Signature:

ABSTRACT

EFFECT OF BUILD DIRECTION ON CRACK GROWTH BEHAVIOR OF Ti6Al4V ALLOY MANUFACTURED BY ELECTRON BEAM MELTING

Çalık, Feyziye
Master of Science, Metallurgical and Materials Engineering
Supervisor: Prof. Dr. Rıza Gürbüz

December 2022, 94 pages

The effects of build orientation on the crack propagation behavior of Ti6Al4V fabricated by elecron beam melting which is one of metal additive manufacturing methods were examined in this study. Firstly, Ti6Al4V blocks were manufactured at different building angles (0^0,30^0,45^0 and 90^0) regarding as base plane using EBM. Subsequently, test specimens were machined from these blocks in compliance with ASTM E8, ASTM E399 and ASTM E647 standards for tensile, fracture toughness and crack growth rate specimens, respectively. Computed tomography was used to determine the amount of defects prior to fatigue crack growth test. dadN vs. ΔK graphs of these specimens constructed at four different angles were investigated. Scanning electron microscope was used to analyse fracture surfaces

It was noted that parts produced at 0^0 angle have higher tensile mechanical properties. On the other hand, parts EBM processed with 30^0 have less elongated structure due to the unmelted regions.

Regarding as crack propagation, part EBM processed with 30^0 has the lowest resistance to fatigue crack propagation.

Keywords: electron beam, crack growth rate, additive manufacturing

ÖZ

YAPI YÖNÜNÜN ELEKTRON IŞINIYLA ERİTME YÖNTEMİYLE ÜRETİLEN Ti6AL4V ALAŞIMINDA ÇATLAK BÜYÜME DAVRANIŞINA ETKİSİ

Çalık, Feyziye
Yüksek Lisans, Metalurji ve Malzeme Mühendisliği Bölümü
Tez Yöneticisi: Prof. Dr. Rıza Gürbüz

December 2022, 94 sayfa

Bu çalışmada, metal katkılı imalat yöntemlerinden biri olan elektron demeti eritme yöntemiyle üretilen Ti6Al4V'nin çatlak ilerleme davranışına yapı yöneliminin etkileri incelenmiştir. İlk olarak EBM kullanılarak Ti6Al4V blokları taban düzlemine göre farklı yapı açılarında (0^0,30^0,45^0 ve 90^0) imal edilmiştir. Daha sonra bu bloklardan çekme, kırılma tokluğu ve çatlak büyüme hızı numuneleri için sırasıyla ASTM E8, ASTM E399 ve ASTM E647 standartlarına uygun test numuneleri işlenmiştir. Yorulma çatlağı büyüme testi öncesinde kusur miktarını belirlemek için bilgisayarlı tomografi kullanıldı. Dört farklı açıda oluşturulan bu numunelerin dadN - ΔK grafikleri incelenmiştir. Kırık yüzeyleri analiz etmek için taramalı elektron mikroskobu kullanıldı.

0^0 açısı ile üretilen parçaların çekme mekanik özelliklerinin daha yüksek olduğu kaydedilmiştir. Öte yandan, 30^0 açı ile işlenen EBM parçaları, kırık düzlemde erimemiş bölgelerin fazlalığı nedeniyle daha az uzamış bir yapıya sahiptir.

Çatlak ilerlemesi ile ilgili olarak, 30^0 açı ile işlenen EBM parçası, yorulma çatlağı ilerlemesine karşı en düşük dirence sahiptir.

Anahtar Kelimeler: electron ergitme, çatlak ilerleme hızı, eklemeli imalat

To my precious family

ACKNOWLEDGMENTS

I am grateful to my supervisor Prof. Dr. Rıza GÜRBÜZ for his patience, guidance and insight throughout the research.

I would like to specially thank to Turkish Aerospace for fabrication of specimens used in this study.

There are many precious people who helped throughout the study. I would like to express my deepest appreciation to Kadir KARAMAN, Abdurrahman ADACI and Muharrem ERTÜRK for their all contributions and valuable times. I could not complete the mechanical tests without their support. I am also grateful to Zeynep ÖZEN, Beyza TARHAN and Emin TAYLAN for their practical efforts for microscopic analyses in both optical microscope and SEM (Scanning Electron Microscope). I wish to express my thankful to Seyit Ali ÖRSEL and Salih Kaan KİRDECİLER for their help. I would like to state my thankful to Orhan Mert KUMBASAR and Utku ŞAHİN for their efforts and advises in CT (Computed Tomography) investigations. To summary, I am very grateful for their valuable time and experience to each member of our material and process laboratory team in Turkish Aerospace. Thank you so much for everything, I could not achieve this research if you were not.

Finally, I must indicate my deepest gratitude to my parents for their endless moral support in this period.

TABLE OF CONTENTS

LIST OF TABLES

TABLES

LIST OF FIGURES

FIGURES

CHAPTER 1

INTRODUCTION

Additive manufacturing (AM), also called as 3D printing, is a rapidly growing manufacturing technology due to its capacity to fabricate functional and complex structures which might be hard and impossible to fabricate with conventional production methods and thus additive manufacturing allows to reduce the amount of waste material and production time. The additve manufactruing principle is based on the layer by layer production by using computer aided design. Electron beam melting (EBM) is one of the 3D manufacturing methods capable of obtaining functional metallic products specially in aerospace applications. In aerospace industry, Ti6Al4V components have particularly gained considerable attention because of its favorable mechanical qualities such as corrosion resistance and high specific strength which means high stregth to weight ratio.

The fatigue fracture properties of AM parts mainly depend on material, build orientation, post processes such as machining and heat treatment as well as machine settings. Limited studies with respect to fracture properties of EBM processed Ti6Al4V are available in literature although tensile properties have been well documented for different surface conditions and heat treatments.

Therefore, in this study, Ti6Al4V parts manufactured by EBM at different angles were examined to evaluate the fracture toughness and fatigue crack growth properties

CHAPTER 2

LITERATURE REVIEW

2.1 Titanium Alloys

Titanium has two types of crystal structure called as alpha (a) and beta (b), For pure titanium, the stable structure in temperatures below $882 \pm 2\ ^0C$ is hexagonal closed packed (hcp) a phase crystal structure. At higher temperatures than 882^0C ,the stable phase is body-centered cubic (bcc) b phase. While temperature goes beyond 882°C, hexagonal close packed (hcp) α-phase undergoes an allotropic transformation to a body-centered cubic (bcc) b phase. Figure 2.1 represents the relation between two allotropic structures and temperature.

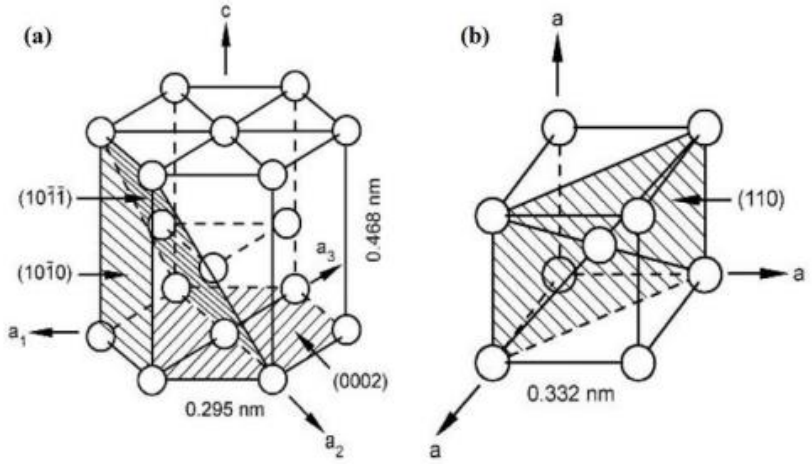

Figure 2-1. The atomic unit cell of titanium; (a) α-phase (bcc), (b) β-phase (hcp) [1]

Allotropic transformation temperature, also known as beta transus temperature , can be changed by adding alloying elements. Alpha stabilizers consist of interstitial alloying elements (N, C, O)) and substitutional alloying elements (Al, Sn, Ga, Gr, La) Conversely, the alloying elements including V, Fe, Cr, Nb, Mo act as beta stabilizers. The effects of alloying elements addition on the transformation temperature is shown Figure 2.2.

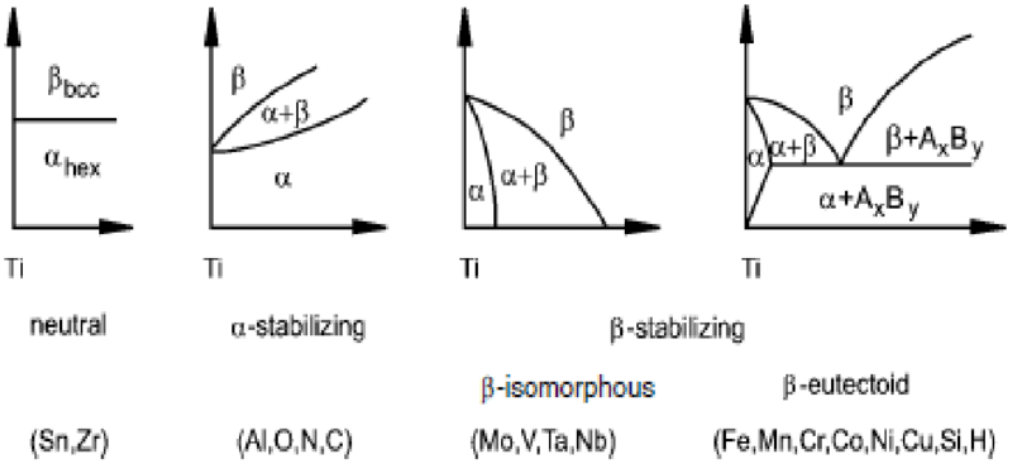

Figure 2-2. The affects of alloying elements on phase diagrams [1]

2.1.1 α Alloys

Commercially pure titanium contains alpha stabilizers and neutral elements. Nearly 100% hcp alpha phase maintains the stability at low temperatures. Alpha alloys are not heat treatable and consequently their mechanical and microstructural properties cannot be altered by heat treatment. However, solution annealing by intersitial elements such as O and N can be used to develop the strength mechanism of these alloys. Ti-5Al-2.5Sn is an all-alpha alloy and has good oxidation resistance up to 1050 F. Moreover, superior weldability, high toughness behavior at low temperatures are two important property of alpha alloys. Due to the combination of high creep resistance and high strength, near alpha alloys are mainly preferable for cryogenic applications. Ti-8Al-1Mo-1V alloy is a near-alpha composition developed for improved creep resistance and thermal stability up to about 850 F. [2,3] Ti-3Al-2.5V and Ti-5Al-2.5Sn are frequently used alpha (a) alloys.

2.1.2 α+β Alloys

α+β alloys are considerably used in aerospace and medical components.They are heat treatable ; that is, mechanical properties of these alloys can be enhanced by

various heat treatment and thermomechanical processes regarding with the amount and type of alloying elements. By this way, α+β alloys are the best option for different mechanical combinations such as high tensile strength vs fracture toughness or good creep resistance vs low cycle fatigue. Ti-6Al-4V are dominating effect on the titanium market compared to other alloy groups.

2.1.3 β Alloys

A beta titanium alloy with 100% beta phase is formed by quenching to room temperature without martensitic structure formation in the existence of sufficient beta stabilizer. Metastable beta alloys contain a small amount of alpha stabilizer. The strength of these alloys can be increased high values more than 1400 MPa. (3) BETA C and TIMETAL 10-2-3 alloys are able to show high strength and high toughness due to optimization of their complex microstructures.(5) Moreover, SP700 alloy has extremely superior superplastic behavior at low tempertaures like 700 C. There have been limited beta alloy application because of high dense complex structure and low corrosion resistance compare to α+β alloys. (2)(4)

2.2 Ti-6Al-4V Alloy

The most extensively used titanium alloy is Ti-6Al-4V, which is called as“Grade 5 Titanium” and “workhorse of industry”. Ti6Al4V is most principally used for aerospace and medical industries. Aircraft parts including fuselage, langing gear parts, wings and tail assmeblies, static and rotating components such as blades and fan discs can be exemplified for aerospace applications. Apart from aerospace industry, Ti-6Al-4V is mainly used for bone screws, vessels and implants owing to its biocompatibility in medical fields. [7]

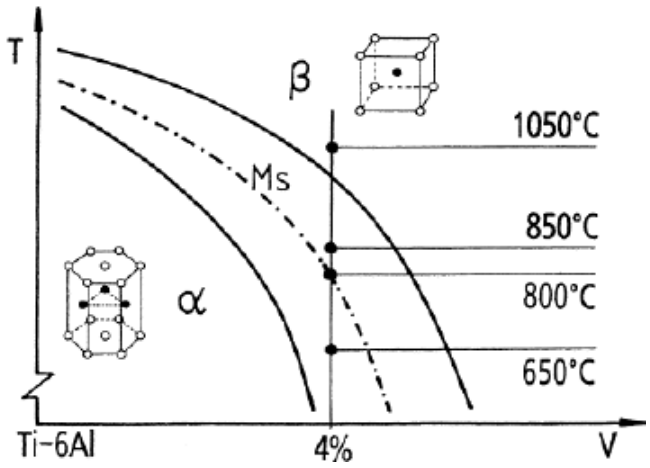

Figure 2-3. Pseudo-binary phase diagram of Ti6Al4V [6]

Al addition by 6% acts as an alpha stabiliser while beta phase is the result of V addition by 4% which is a beta stabilizer. According to the pseudo-binary phase diagram basically shown in Figure 2.3. Alpha + beta phase region are stable at low temperatures with V addition by %4. Elemental composition of Ti6Al4V alloys per different production processes is shown in Table 2.1.

Table 2-1. Chemical composition for cast, wrought and additive manufactured Ti6Al4V per ASTM standards

Element	**Chemical Composition (wt%)**		
	ASTM F1108-14 (Cast)	**ASTM F136-13 (wrought)**	**ASTM F2924-14 (AM)**
Al	5.50 to 6.75	5.50 to 6.50	5.50 to 6.75
V	3.50 to 4.50	3.50 to 4.50	3.50 to 4.50
Fe	0.30 max.	0.25 max.	0.20 max.
O	0.20 max.	0.13 max.	0.20 max.
C	0.10 max.	0.08 max.	0.08 max
N	0.05 max.	0.05 max.	0.05 max
H	0.015 max.	0.015 max.	0.015 max.
Ti	0.015 max.	Balance	Balance

The allotropic transformation temperature of Ti6Al-4V is about 995 ± 20 °C. [12]. Mechanical properties of Ti6Al4V are highly based on the morphology and the arrangement of alpha and beta phases in compliance with cooling rate through quenching from β phase region. Consequently, primary or globular α, martensitic, basketweave and Widmanstätten morphologies can be obtained. These microstructural changes regarding with cooling conditions are represented in the Figure 2.4.The α grain size decreases with high cooling rate during quenching from high temperatures resulting increase in the yield strength and high cycle fatigue. Additionally, ductility decreases due to the martensitic microstructure with smaller α plaths constituted by rapid cooling. [9,10] Moreover, casting Ti6Al4V contains alpha lamellar structure while equiaxed grains with coarse alpha lamellae can be observed in annealed Ti6Al4V. [11]

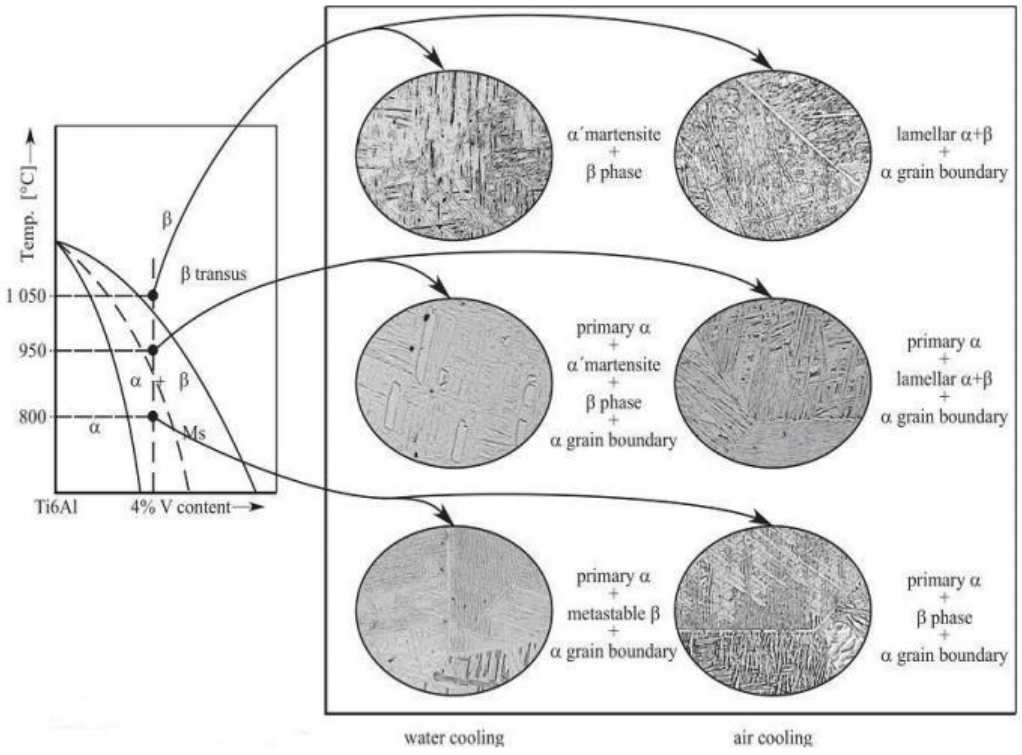

Figure 2-4. The microstructures developed after solution treatment of the Ti6Al4V model titanium alloy [8]

2.3 Additive Manufacturing

According to ASTM F2792-12a, AM is defined as “a process of joining materials to make objects from 3D model data, usually layer upon layer, as opposed to subtractive manufacturing methodologies”.[13]

AM technologies are usually based upon layer by layer production style of components. General production flow diagram of AM is shown in Figure 2.5. First of all, the process starts with the creation of CAD model of the component. The model is turned into STL (Stereolithography) file which digitally slices 3D model into numerous layers. Subsequently, the component is fabricated in AM process layer by layer. Finally, the component is removed from the production platform and different post processes including heat treatment, cleaning or grinding are applied depending on additive manufacturing techniques.

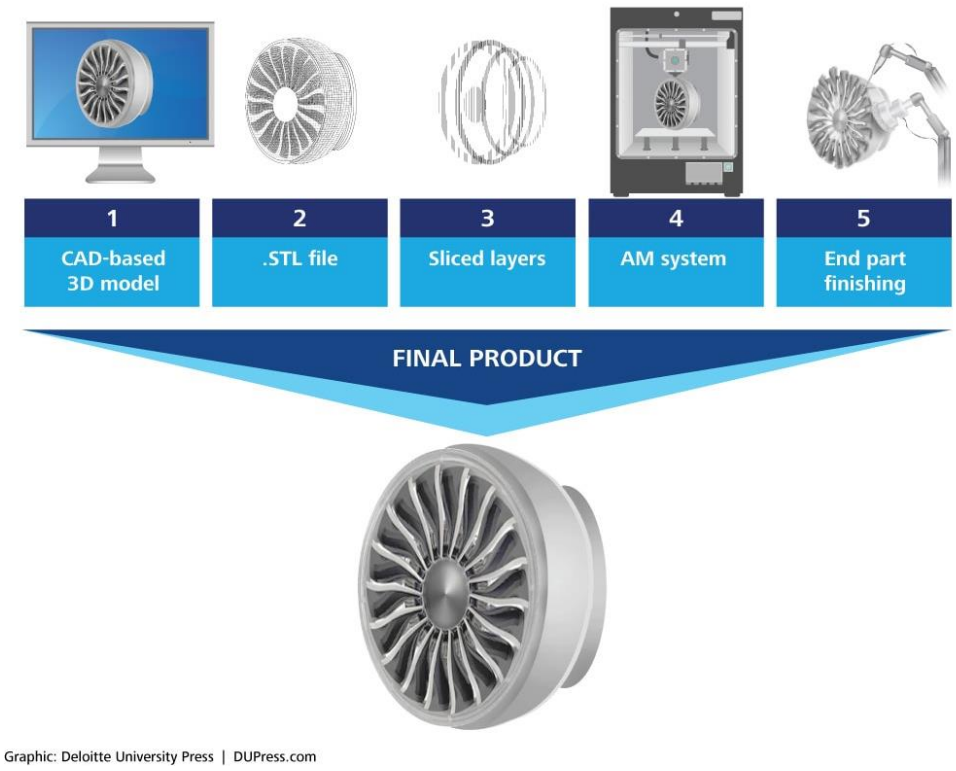

Figure 2-5. AM process flow [14]

Powder bed fusion (PBF) and directed energy deposition (DED) are mostly utilized metal additive manufacturing styles fabricating complex geometries in comparison with conventional fabrication methods. Main metal AM processes commonly on the market are categorized in Figure 2.7.

2.3.1 Direct Energy Deposition (DED)

Directed energy deposition process contains a nozzle moving in multi-axes which can selectively deposit the molten material on the build platform. The main usage area of this tehnique is repairing damaged parts including damaged turbine components. Laser and electron beam are used as an energy source in DED. In terms of high amount of deposition material and high quality repair based on grain structure controlling, this technique can be relatively comparable to other AM techniques. However, the DED fabricated parts have lower surface quality and low accuracy owing to lower resolution resulting secondary procedures. [15]

2.3.2 Powder Bed Fusion (PBF)

Powder bed fusion process consists of a build platform moving Z axis.The process starts with the roller spreading a layer of powder material on the build stage and the heat source moves in X and Y axis to penetrate into the metallic powders. Laser, electron beam or plasma can be used as a heat source. The process is continuously conducted till the 3D final part is entirely obtained. [16] The powder bed fusion method using laser as a heat source is schematically demonstrated in Figure 2.6

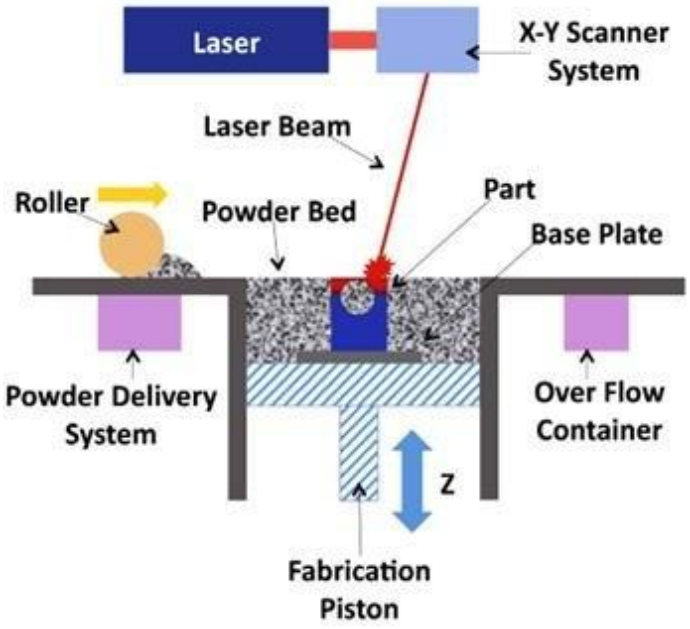

Figure 2-6. The powder bed fusion method using laser as a heat source [17]

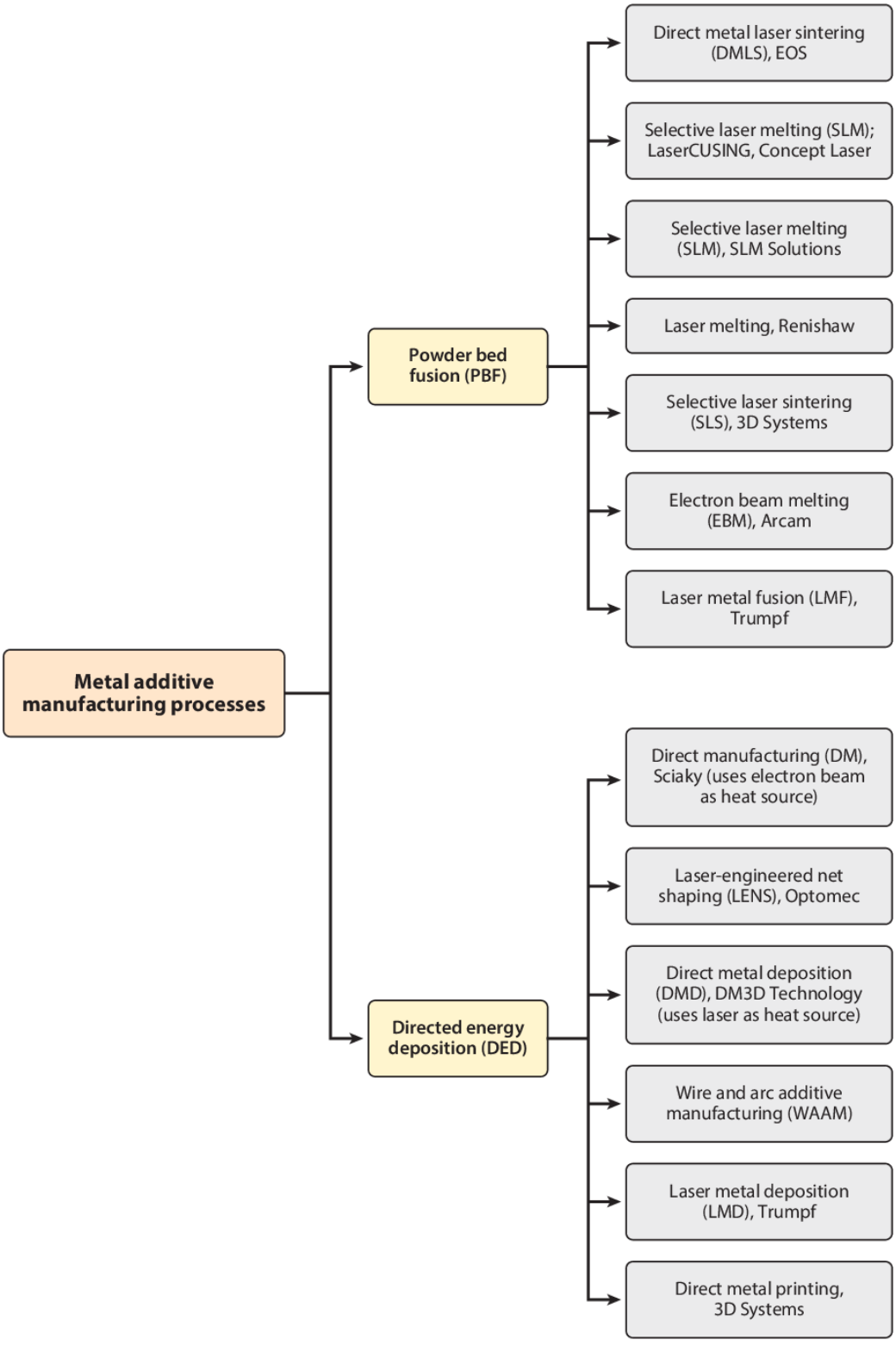

Figure 2-7. AM processes with respect to their producer names [18]

SLM and EBM are the most demanding powder bed fusion additive manufacturing methods to offer a high resolution and a geometrical control. Although they have the same working principle, the use of different heat sources is associated with differency in processing conditions and consequently characteristic properties. In SLM, the process is takes place under an inert atmosphere (argon or nitrogen gases) so as to avoid the contamination of metal powders, while a vacuum is needed to prevent the deflection of an electron beam by gas impurities in EBM. [19]

SLM is also known to create residual stress along build direction. During the fabrication, releasing of a large amount of heat in the chamber causes high thermal gradients in produced parts. The main reason of formation shrinkage or cracking is the generation of residual stress which is the result of high thermal gradients with respect to fast cooling rate during the SLM process. [20][19][21]

In SLM process, photons of a laser beam are the main source of the thermal energy to melt metal powders. However, in EBM method, the kinetic energy of electrons transforms the thermal energy to fuse the powder. EBM process has more energy efficency than SLM process. An electron relatively diffuses larger and more powder particles by virtue of its larger spot size than a laser beam. Larger and more diffusive areas are obtained due to higher temperature (up to 1000^0 C) in base plane resulting in slower cooling rate. Unlike SLM processed objects, EBM produced parts have relatively lower internal stress because of smaller thermal gradients between layers during melting of the powder. In addition to this, high pre-heating temperature which offers the heating of the powder nearly softening temperature. Consequently, the microstructure of EBM produced parts has usually lamellar structures.The EBM process contains several production parameters including beam focus, beam line spacing, beam diameter, beam power, beam scanning velocity, plate temperature, pre-heat temperature (including the repetitions, power and speed of the beam), contour strategies, and scanning strategy. [18][19][21] The optimization of all these process parameters is more difficult when compared to SLM process. In EBM, limited conductive materials including Ti-Grade 2, Ti6Al4V, CoCrMo, Inconel 718 are used in EBM method. [22]. EBM process will be studied in this thesis.

2.4 Electron Beam Melting of Ti6Al4V

Liu et al. summarized tensile properties of as-built EBM processed Ti6Al4V specimens shown in Table 2.2.Under tension loading, the horizontal samples generally have higher UTS and YS than longitudinal samples. The anisotropic microstructure including elongated columnar β and grain boundary α results in different mechanical properties in the horizontal and longitudinal direction.[23]

Table 2-2. Tensile properties for EBM processed Ti6Al4V in different conditions [24-28]

Condition	**Specimen Orientation**	**UTS [MPa]**	**YS [MPa]**	**EL [%]**
As-built, not machined	Longitudinal	851±19	812±12	3.6±0.9
	Horizontal	833±22	783±15	2.7±0.4
Aa built, machined, interior location	Longitudinal	1032.9±12.9	984.1±8.5	9.0±2.9
As built,machined, exterior location		1008.6±15.2	961±7.1	7.1±3.4
As built, machined, interior location	Horizontal	1029.7±7	982.9±5.7	12.2±0.8
As built,machined, exterior location		1017.4±4.9	966.5±5.3	12.2±2.0
As built, machined	Longitudinal	972±14	845±9	14.2±1.5
	Horizontal	976±11	846±7	15.0±2.0
As built, machined	Longitudinal	928±9.8	869±7.2	9.9±1.7
	Horizontal	978±3.2	899±4.7	9.5±1.2
Annealed, machined	-	837-918	741-842	3-9
HIPed,machined	-	817-918	723-817	3-9
Stress relieved, machined	-	885-1015	778-943	3-9

In addition, ASTM F2924-14 standard specifies the mechanical properties of AM Ti6Al4V as shown in Table 2.3 by comparison with cast and wrought Ti6Al4V alloy.

Table 2-3.Tensile properties of cast, wrought and AM Ti6Al4V alloy

Standard	**Yield Strength (MPa)**	**Ultimate Tensile Strength (MPa)**	**Elongation (%)**
ASTM F1108-14 (cast)	758	860	8
ASTM F136-13 (wrought)	795	860	10
ASTM F2924-14 (AM)	825	895	10

The microstructure of EBM processed Ti6Al4V shown in Figure 8 consists of α + β lamellas in widmanstätten structure or basketwave structure and the prior β columnar grains along building direction.

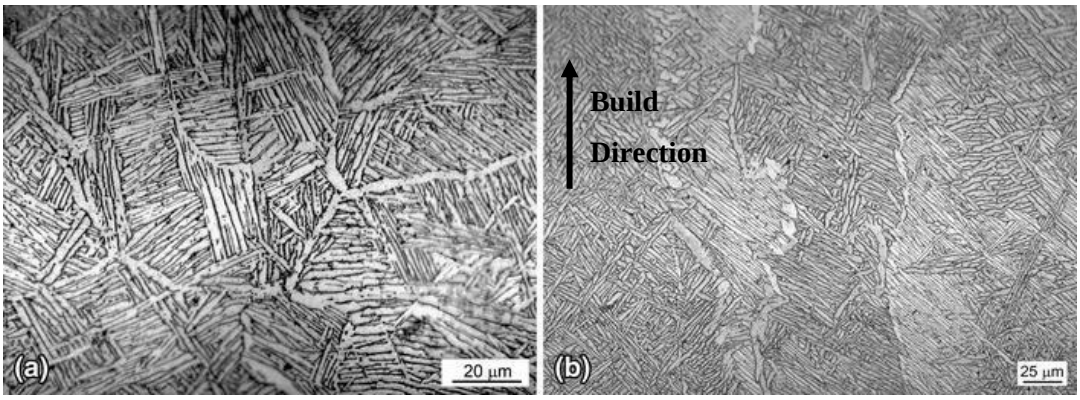

Figure 2-8. Microscopic images of the as-built EBM Ti-6Al-4V samples: (a) longitudinal direction and (b) transverse direction [27]

Chern et al. analyzed the fatigue behavior of EBM manufactured samples depending on different post processes. It was reported that horizontally built EBM samples exhibit higher fatigue resistance because vertically built samples are exposure to more crack origination sites resulting from rough surface. [29]

There were limited studies about fracture behavior of EBM fabricated parts as fracture toughness and fatigue crack behavior. Seifi et al. reported that differences in the microstructure and defects depending on orientation effect the fracture parameters. Post-process HIP or machining can be applied to obtain acceptable microstructures and eliminate or reduce the internal flaws. In addition, several EBM fracture data were reported as KQ due to the violation of specified thickness criteria. [30]

Edwards and Ramulu also examined the orientation dependence of fracture toughness behavior horizontally and vertically using EBM process. [31] The fracture toughnes values of EBM fabricated parts were superior compared to annealed Ti6Al4V and thicker specimens were suggested to acquire a valid fracture toughness result. They also stated that of EBM samples had slightly developed Region II dadN crack growth behavior when compared to wrought Ti6Al4V alloy.

Lewandowski and Seifi reviewed the calculated fracture toughness values with respect to different orientation in Table 4. [32]

Table 2-4. The summarization of AM Ti-6Al-4V EBM-PBF fracture toughness [30][31][33]

Condition	Specimen Type	Specimen orientation	Kq	Ref.
As built	3PB	XYZ	68, 80	30
		XZY	76	
		ZXY	65, 66	
As built	CT	XY	110 ± 8.9	31
		ZX	102 ± 7.4	
As built	CT	XY	96.9	33
		ZX	78.1	
HIP		XY	99.0	
		ZX	83.1	

2.5 Fatigue Fracture Mechanism

Fatigue is defined as permanent and localized changes in mechanical and microstructural properties of metallic materials exposed to continuously stress and variable strains less than the yield strength of the material. This fluctuating or cyclic streess and strain mechanism finally lead to failure or cracking.

Surface flaws, gas pores, notches and surface discontinuities act as a stress amplifier in the materials. A material containing these stress concentrators might suddenly fail under cyclic loading or might show the resistance against failure because of slip formation in the structure.

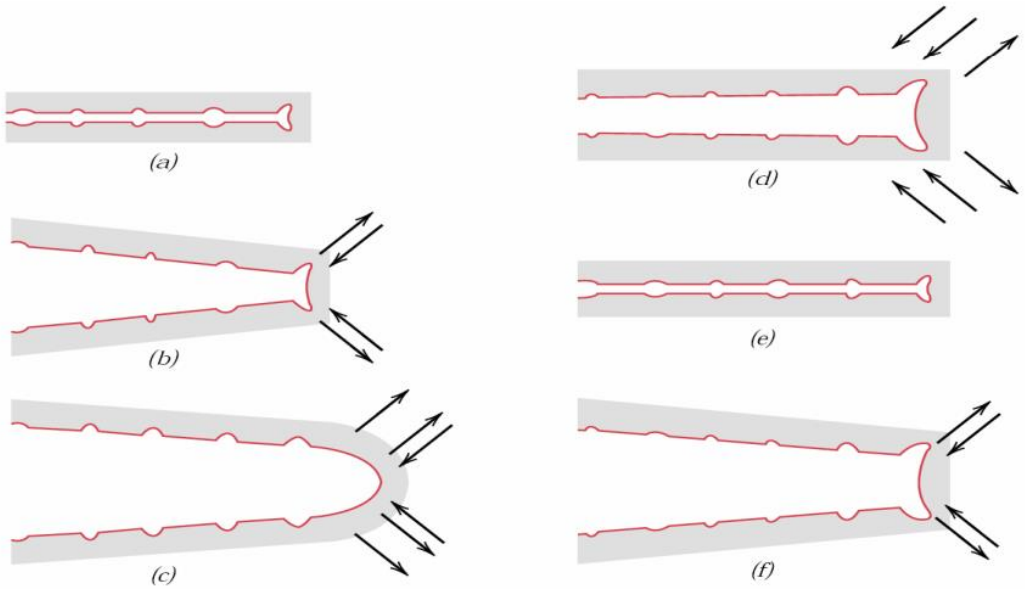

Figure 2-9. Fatigue striation formation by plastic blunting process.(a)zero load.(b) small tensile load.(c)maximum tensile load.(d) small compressive load.(e) maximum compressive load.(f) small tensile load. [37]

The fatigue crack growth mechanism divided into three main regions.In Region I, there is a stable crack propagation because of shearing and the small cracks formation. Region II indicates that crack growth is driven by striation formation as a result of plastic blunting process shown in Figure 9. Plastic zone at the crack tip concentrates at the slip planes of the crack and then the crack expands to its maximum level resulting in plastic shearing and blunting structure. When the load is changed from tension to compression, reversible slip direction is observed at the crack tip. The new cracks in tension is forced into the folded crack plane to form the resharpened crack tip. Hence, the repetitive process of crack sharpening followed by plastic blunting constitutes the fatigue striation. This region specifies the fatigue life of materials due to depending on the flow properties of the material. [37]

In Region III of crack growth, the crack growth rate is relatively high and unstable. Moreover, maximum stress intensity nearly equals the fracture toughness, Kc, of the material in this region.

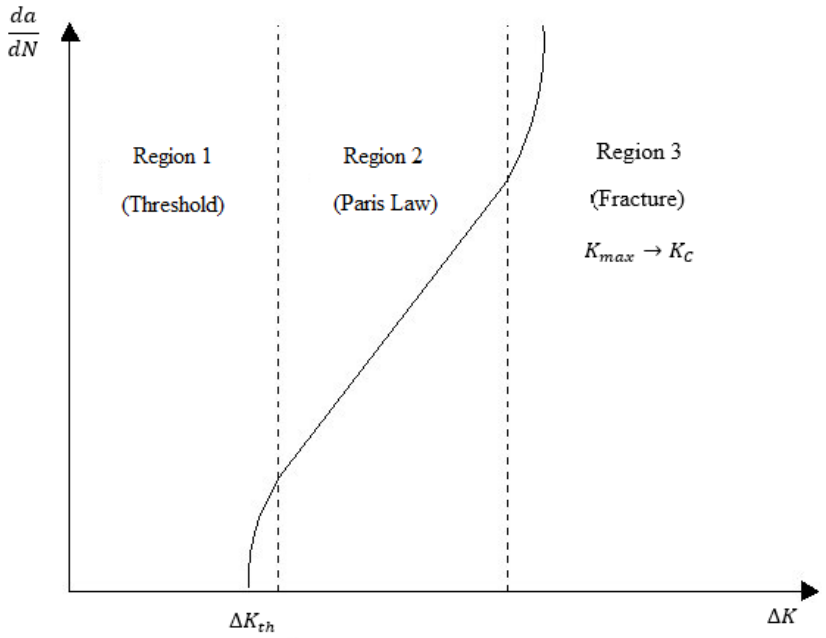

Figure 2-10. Typical fatigue crack growth curve showing the three main regimes

In the first region of this curve indicates that there are non-propagating cracks below ΔKth and the threshold value can be used at low low stress levels. The crack propagates in order of 10^{-9}m/cycle in this region.

In Region II, the linear relation between the crack growth rate, da/dN, and the stress intensity factor range, ΔK, can be achieved by applying Paris law as the concept of linear elastic fracture mechanics.

$$\Delta K = K_{max} - K_{min}$$

$$\frac{da}{dN} = C(\Delta K)^m$$

In the above equation, C and m are material properties obtained experimentally and depend on loading frequencies, mean load and environment. ΔK is the range of stress intensity factor during cylic loading. The constant m in the equation varies by the toughness of material.

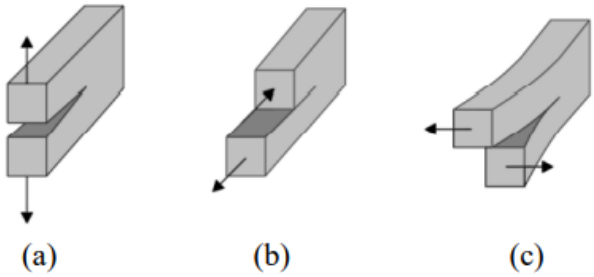

Figure 2-11. Three fracture loading modes of crack (a) Mode I (b) Mode II (c) Mode III

There are three loading types in fracture mechanisms as opening (mode I), sliding (mode II) and tearing (mode III) represented in Figure 2.11. In addition, three types of load and displacement curves are drawn based on the loading types to determine the critical load and fracture toughness. The critical load is defined by drawing 95% of the linear slope or 5% secant offset and thus for Type 1 the defined Pq is equal to P5 represented in Figure 12. However, if there is a maximum force above P5, the maximum force is Pq in the state of Type II and Type III, also shown in Figure 2.12.

In this study, Type I load and displacement is addressed depending on the fracture toughness of material. The compact tension geometry, farcture mechanics parameters and test validity requirements of fracture toughness are specified in compliance with ASTM E399.

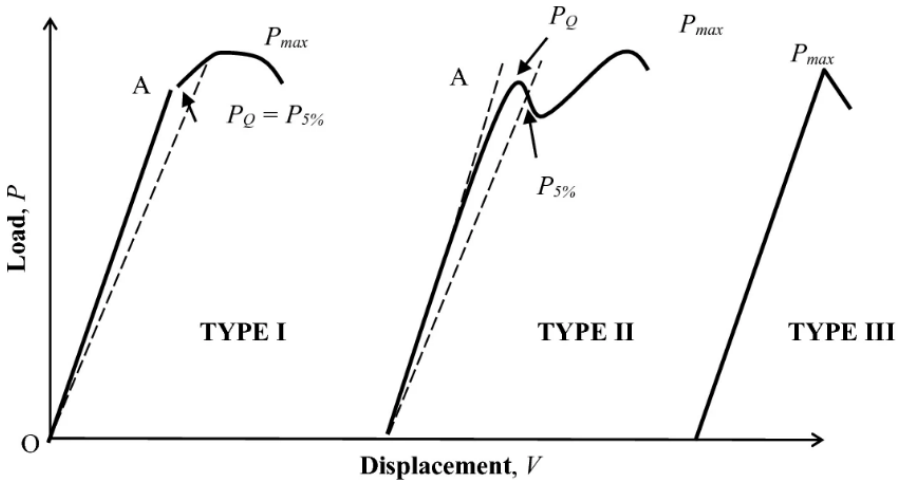

Figure 2-12. Typical load-displacement curves of fracture toughness test

CHAPTER 3

EXPERIMENTAL PROCEDURE

3.1 Material

All test specimens were fabricated using ARCAM Ti6Al4V powders (Grade 5). Chemical composition of Ti6Al4V powders was given in Table 3.1. Powder size of the ARCAM Ti6Al4V is the range of 45 and 100 μm and supplied by the machine manufacturer. Figure 3.1 also shows the EDS analysis of Ti6Al4V powder particles examined in this study.

Table 3-1. Chemical concentration of Ti6Al4V powders (weight %)

Element	ASTM F2924-14 (AM)	Arcam Company (supplier)	EDS analysis for this study
Al	5.5-6.75	6	6.36
V	3.5-4.5	4	4.35
C	0.08	0.03	-
Fe	0.3	0.1	-
O	0.2	0.15	-
N	0.05	0.01	-
H	0.015	0	-
Ti	Balance	Balance	89.29

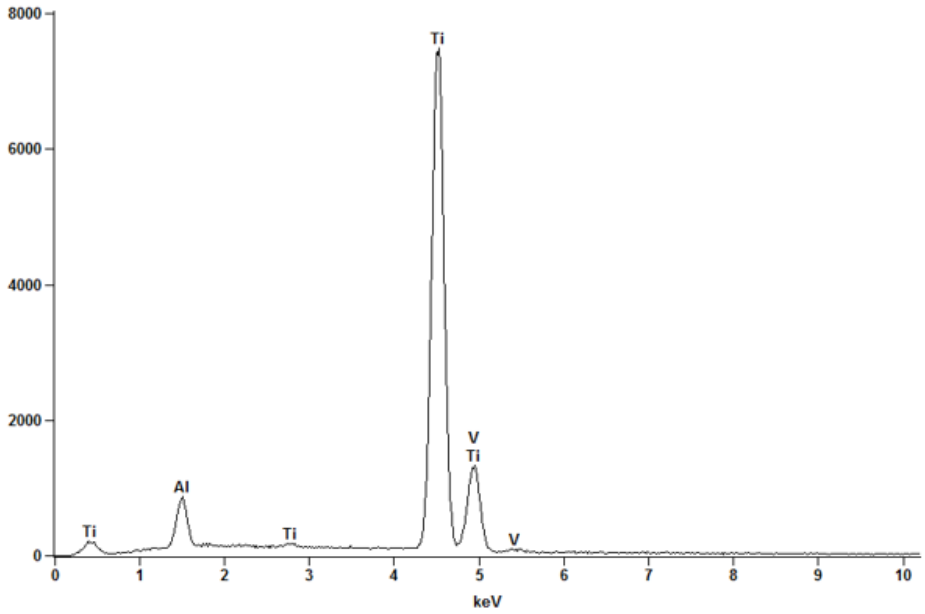

Figure 3-1. EDS analysis of powder particles

3.2 Process Parameters

All of the specimens were fabricated by the same process parameters identified and recommended by the algorithm of ARCAM Company as shown in Table 3.2. In this study, ARCAM Q20 EBM Machine at Turkish Aerospace was used and EBM system was shown in Figure 3.2.

EBM process consists of preheating and melting stages at a vacuum chamber.

Table 3-2. Built process parameters

Pre Heat 90 µm	Pre Heat	Focus Offset	44mA
		Heating Focus Offset	100 mA
		Offset to part	4mm
		Max. Heat Time	60s
	Pre Heat 1	Max Beam Current	36 mA
		Beam Speed	40500 mm/s
		Max. No. Of Repetitions	3
		Average Current	NA
	Pre Heat 2	Max Beam Current	45 mA
		Beam Speed	40500mm/s
		Max. No. Of Repetitions	3
		Average Current	13.95 mA
Melt 90 µm	Outer Contour	Current	9mA
		Focus Offset	6mA
		Speed	450mm/s
	Inner Contour	Current	9mA
		Focus Offset	6mA
		Speed	450mm/s
	Hatch	Beam speed	4530 mm/s
		Beam Current	15mA
		Max Current	28mA
		Min Current	3.5mA
		Focus Offset	45mA
		Hatch Depth	0.09 mm

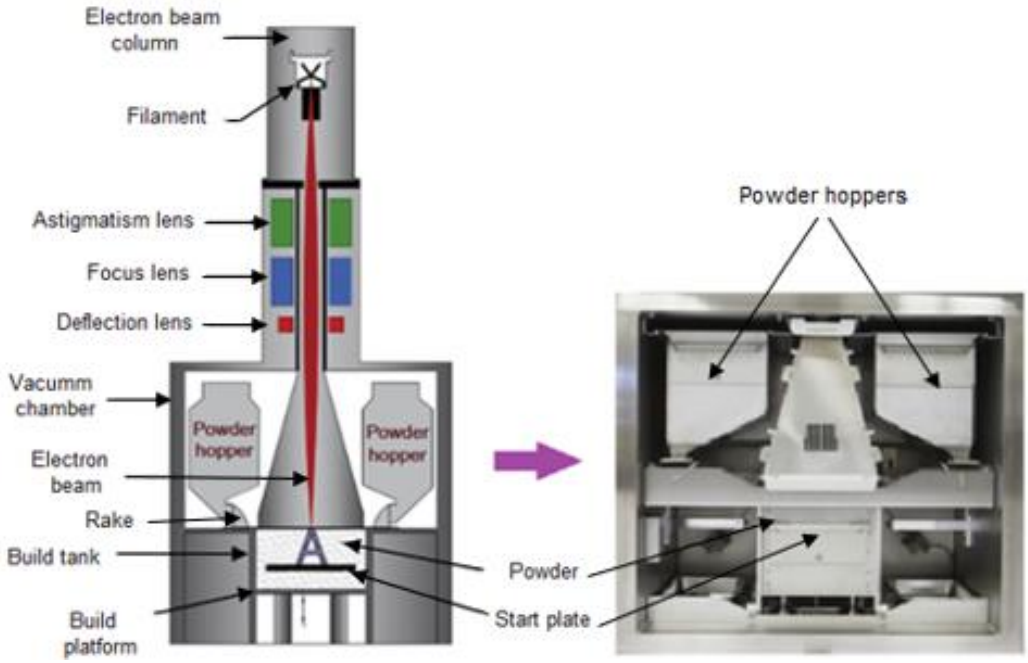

Figure 3-2. ARCAM Q20 EBM Machine

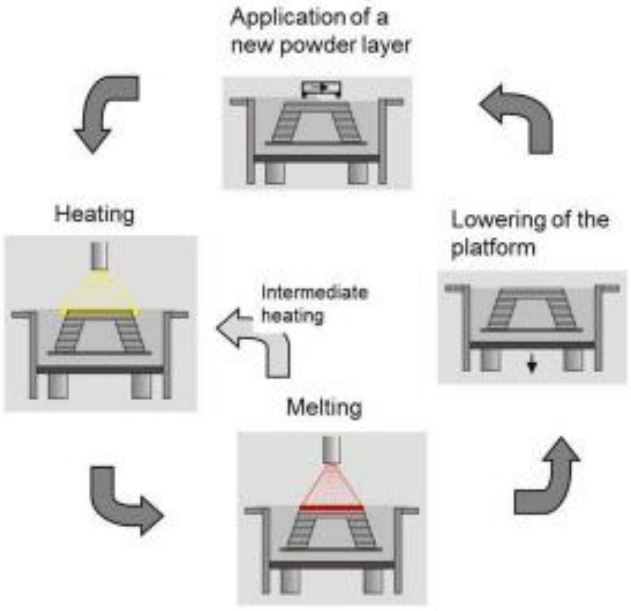

Figure 3-3. The schematization of EBM process for building one layer [39]

The process of EBM for Ti6Al4V basically shown in Figure 3.3 started with using the electron beam to preheat a build plate to a set approximately 750 °C in the vacuum chamber. The build plate was lowered and a raking system spreads a layer of powder in 90 μm of layer thickness. The powder bed was preheated by the electron beams and subsequently the electron beams melted two contours by starting with outside of the geometry in each layer being produced. Lastly, the beam was used to fill these contour regions by rotating hatch with a raster pattern with the x or y axes represented in Figure 3.5.After completion of the fabrication, helium gas was used to cool the vacuum chamber to under 100 °C before taking the ambient room condition. [40] The layer by layer production is basically demonstrated in Figure 3.4.

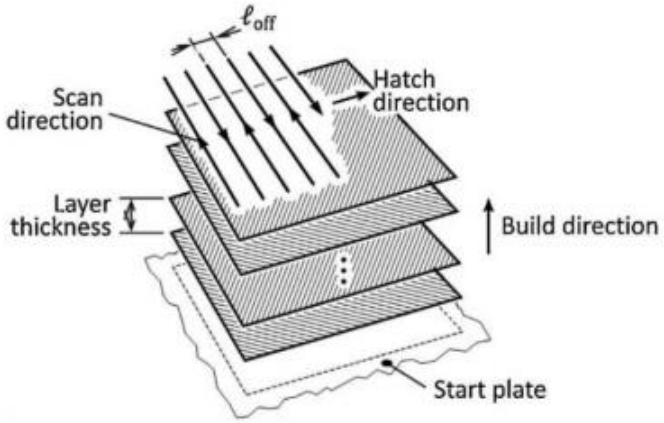

Figure 3-4. Layer by layer process [41]

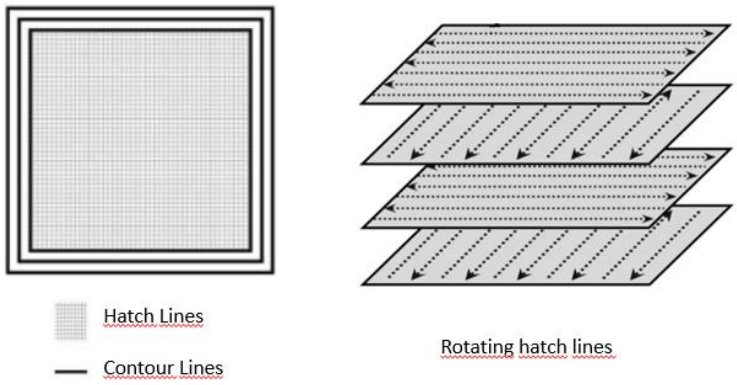

Figure 3-5. Rotation hatch lines

3.3 Test Geometries

All test specimens were machined from blocks deposited in four different angles (0^0, 30^0,45^0, 90^0) regarding as production base plane. Figure 3.6 shows these blocks per their build directions in the chamber with the coordinate system. The each blocks were labeled per direction as indicated in Table 3.3.

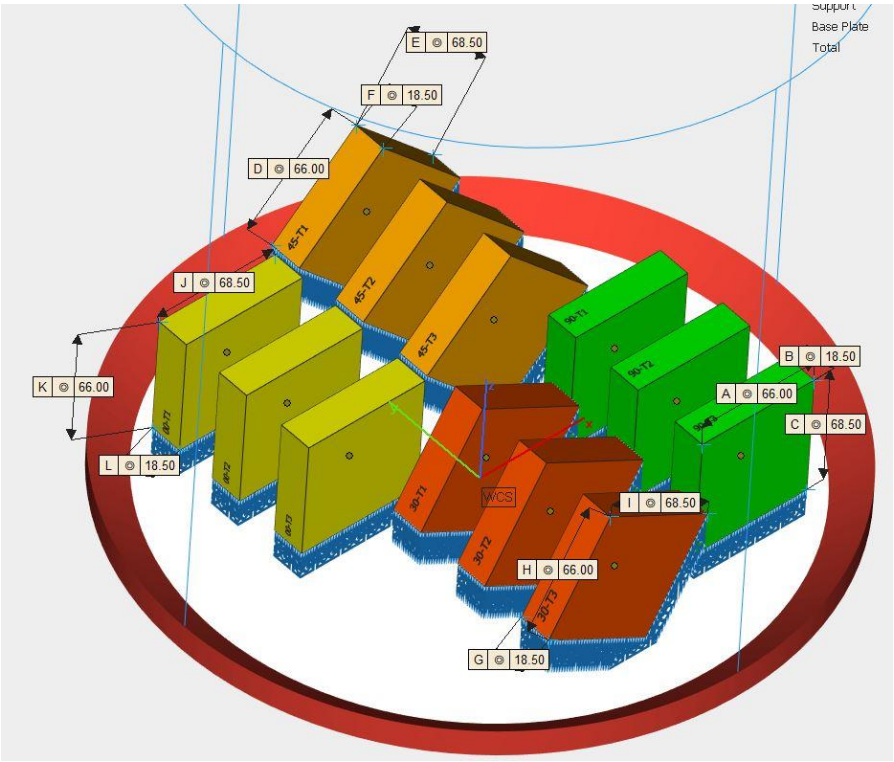

Figure 3-6. The schematization of the block orientation in the vacuum chamber

Table 3-3. Nomenclature of specimens

Build Angles	Nomenclature
0^0	00T
30^0	30T
45^0	45T
90^0	90T

3.3.1 Tensile Test Specimen

The dimension of tensile test specimen is represented in Figure 3.7. Two specimens per each direction were designed and in total eight specimens were obtained. One of the fabricated blocks and finished tension test specimens are shown in Figure 3.8.

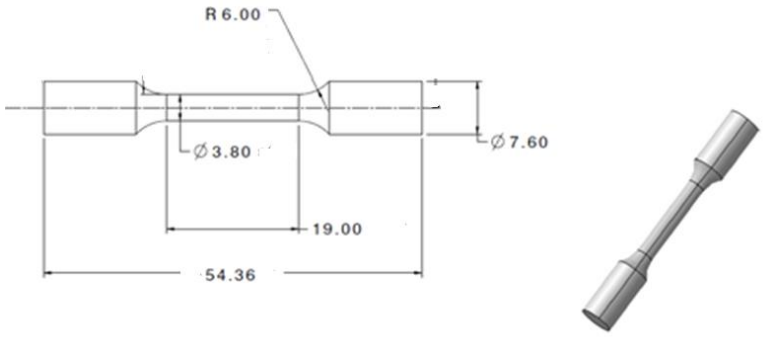

Figure 3-7. Dimension of the tensile test specimen per ASTM E8M

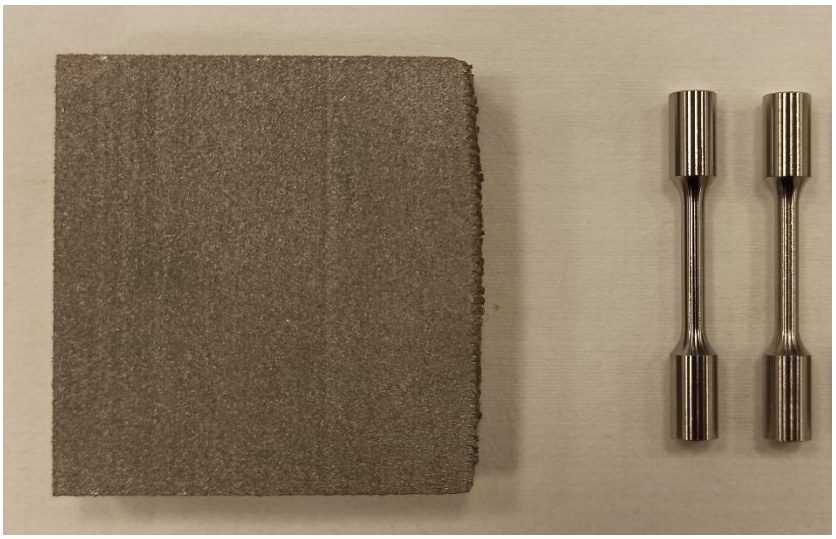

Figure 3-8. Block fabricated by EBM and finished tension test specimens

3.3.2 Fracture Toughness Test Specimen

For fracture toughness, compact tension, CT, specimens were machined per ASTM E 399 with B= 12.5 mm and W= 25 mm as represented in Figure 3.9. Machined test specimens are shown in Figure 3.10.

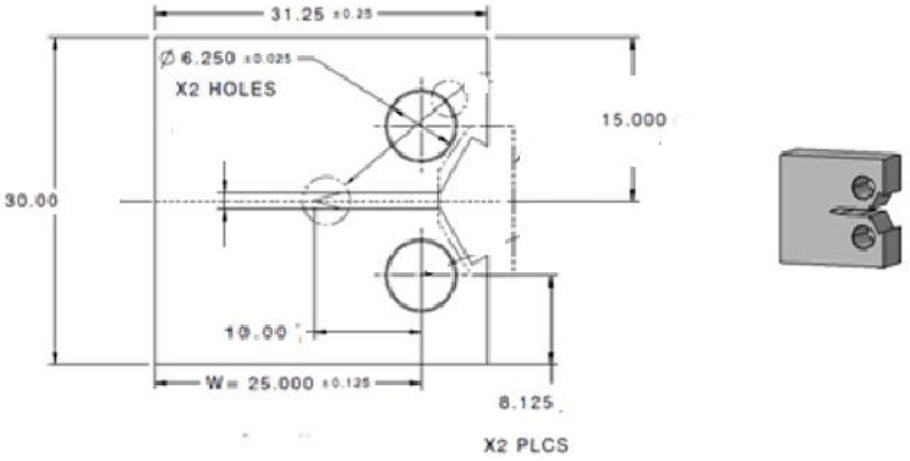

Figure 3-9. Dimension of the fatigue toughness test specimen per ASTM E399

Figure 3-10. Finished fracture toughness specimens

3.3.3 Crack Growth Test Specimen

For crack growth test, C(T) test specimens were designed according to ASTM-E647 with B=12.5 mm and W=50 mm as shown in Figure 3.11 and the final test specimen is shown in Figure 3.12.

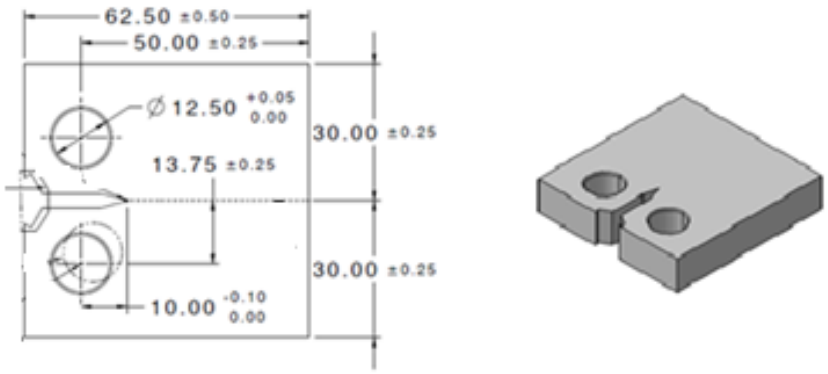

Figure 3-11. Dimension of the crack growth test specimen per ASTM E647

Figure 3-12. Finished CT (50) test specimens

3.4 Microstructure Examination and Hardness Test

For the microstructure examination, the specimens cut from blocks were prepared then mounted in bakalite. After mechanical and chemical polishing stage, the specimens were etched for 30-40 s in Kroll's reagent. Etched surfaces were examined by using optical microscope.

Additionally, the Vickers microhardness values of specimens produced at different angles were measured by using Quness microhardness test machine. 10 kg load was applied for 20 points per each side (XY, XZ and YZ).

3.5 Densification Measurement

The density of samples were measured by Archimedes' Method and the measurement was performed by using ethanol which is higher than 99.9 % purity at room temprature. The weight of samples was measured in the air and ethanol respectively. The densities of specimens were calculated using the obtained weight measurements.

3.6 Tensile Test

Tensile specimens produced per ASTM E8M were examined to determine the stress-strain properties by using Instron 5582 Universal Testing Machine. Figure 3.13 represents the production layers with respect to different build angles.

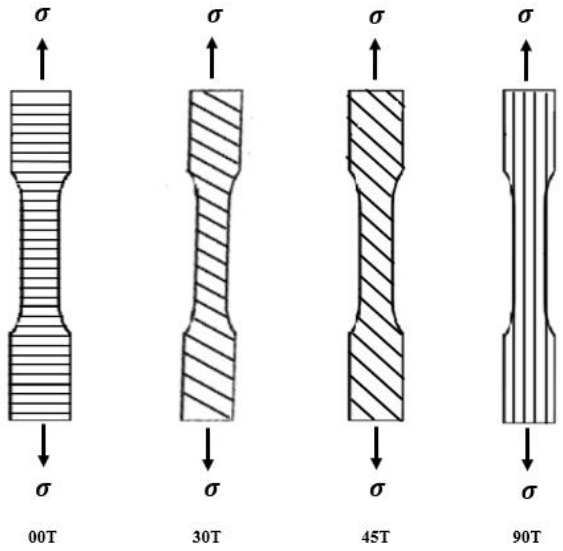

Figure 3-13. The schematization of tensile test specimens. The lines indicate the production layers during EBM process.

3.7 Fracture Toughness Test

Fracture toughness test is performed in order to measure the resistance of a material to failure. In this study, fracture toughness tests of four samples were carried out in compliance with ASTM E399. Figure 3.14 represented production layer lines corresponding to build direction The tests were carried out at room temperature and Instron Model 5985 universal testing machine was used.

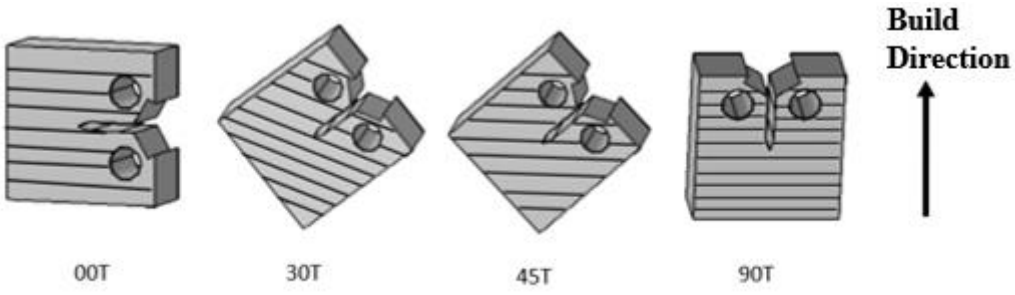

Figure 3-14. Production layer of samples and build direction

For pre-cracking, specimens were performed under fatigue cyclic loading to obtain the appropriate crack size in compliance with ASTM E399 i.e crack size between 0.45 W and 0.55 W. The stress ratio was R=0.1. All specimens were performed at constant load amplitude with initial ΔK= 15 MPa$\sqrt{m}$, increasing ΔK until complete the precrack condition.

After that, Instron crack opening displacement (COD) gage was installed to specimen as represented in Figure 3.15. Static steps were performed Instron electromechanical test machine with 1.65 MPa$\sqrt{m/s}$.

Finally, load-COD displacement curves of four samples were acquired as shown in Figure 3.16. Fracture toughness test calculations were for all specimens indicated in Table 3-4 and Table 3-5.

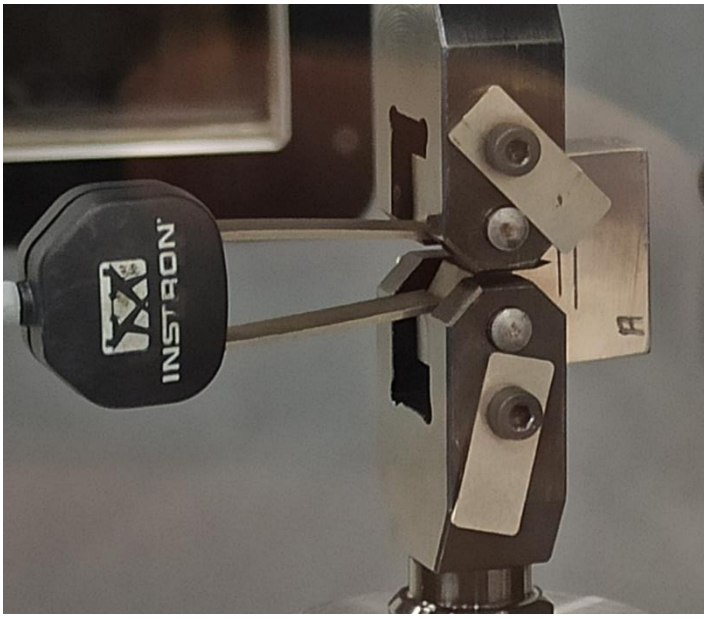

Figure 3-15. The installation of COD displacement gage

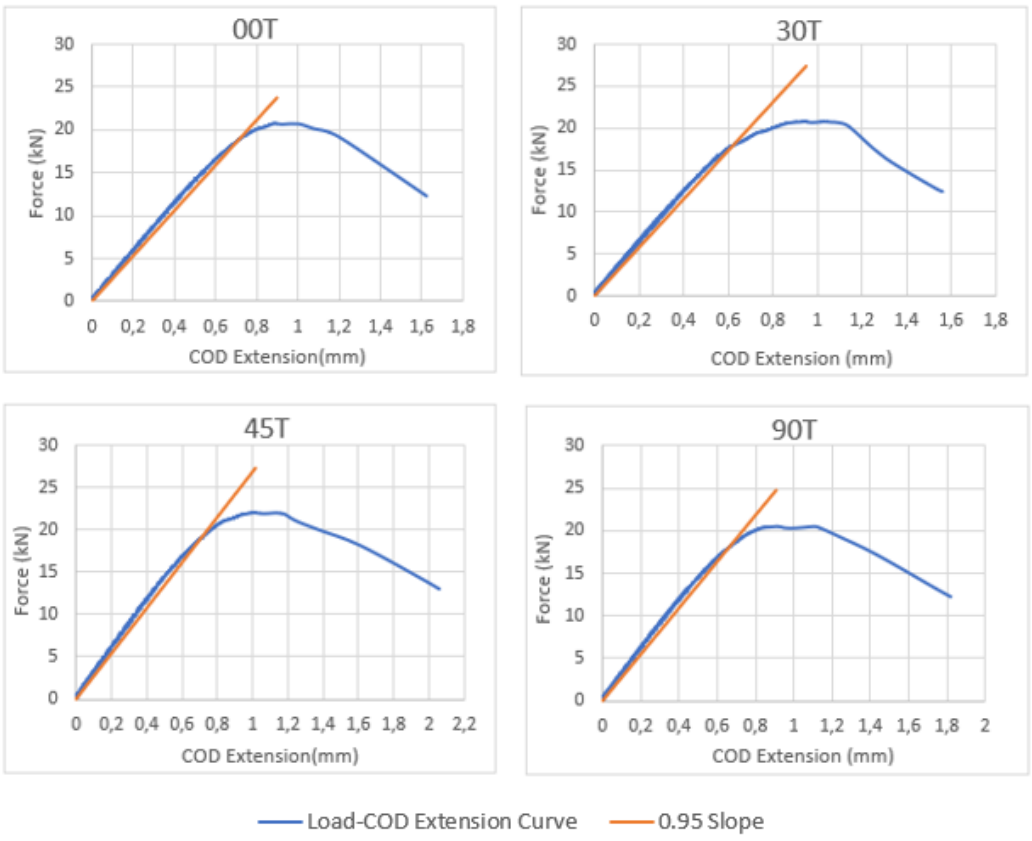

Figure 3-16. Force – COD Displacement graphs of specimens

The crack size was calculated by taking the average of three measurements from the center, the right of center and the left of center over the crack surface as shown in Figure 3.17.

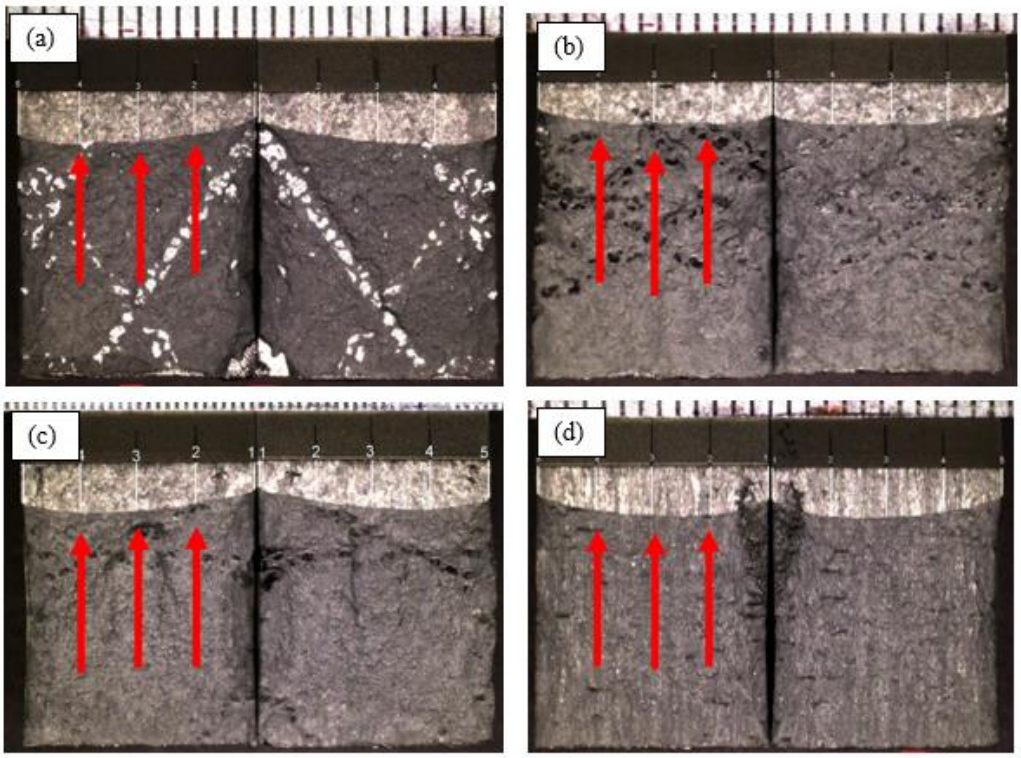

Figure 3-17. Representative of the fracture toughness specimen fracture surfaces of 00T (a), 30T (b), 45T (c) and 90T (d) respectively.

Equation (1) and (2) were used to calculate the fracture toughness of compact tension specimen, K_Q.

$$K = \frac{P}{B\sqrt{W}} f\left(\frac{a}{W}\right) \qquad (1)$$

$$f\left(\frac{a}{W}\right) = \frac{\left(2+\frac{a}{W}\right)\left[0.886+4.64\frac{a}{W}-13.32\left(\frac{a}{W}\right)^2+14.72\left(\frac{a}{W}\right)^3-5.6\left(\frac{a}{W}\right)^4\right]}{\left(1-\frac{a}{W}\right)^{3/2}} \qquad (2)$$

P= applied force

a= crack size

W=specimen width

B= specimen thickness

According to ASTM E399, two requirements must be utilized to identify the plane strain fracture toughness. Equation (3) and (4) are conducted to valid the fracture toughness values.

$$\frac{P_{max}}{P_Q} \leq 1.10 \qquad (3)$$

$$W - a \geq 2.5 \left(\frac{K_Q}{\sigma_{ys}}\right)^2 \qquad (4)$$

Table 3-4. Fracture toughness test results

Specimen	Specimen Thickness B (mm)	Average Crack Size a (mm)	Specimen Width W (mm)	Specimen Ligament Size W-a (mm)	Force P_{max} (kN)	Force P_Q (kN)
00T	12.5	1.60	25	12.44	20.74	18.8
30T	12.5	1.51	25	12.93	20.82	17.91
45T	12.5	1.57	25	12.57	22.1	18.94
90T	12.5	1.68	25	12.48	20.5	18.05

Table 3-5. Fracture toughness test results per ASTM E399

Specimen	Validity Requirement $\frac{P_{max}}{P_Q}$	Validity Requirement $2.5\left(\frac{K_Q}{\sigma_{ys}}\right)^2$ (mm)	Fracture Toughness K_Q (MPa$\sqrt{m}$)
00T	1.1031	23.4	92.5
30T	1.1629	22.3	83
45T	1.1649	24.6	92
90T	1.1358	21.4	88

3.8 Crack Growth Test

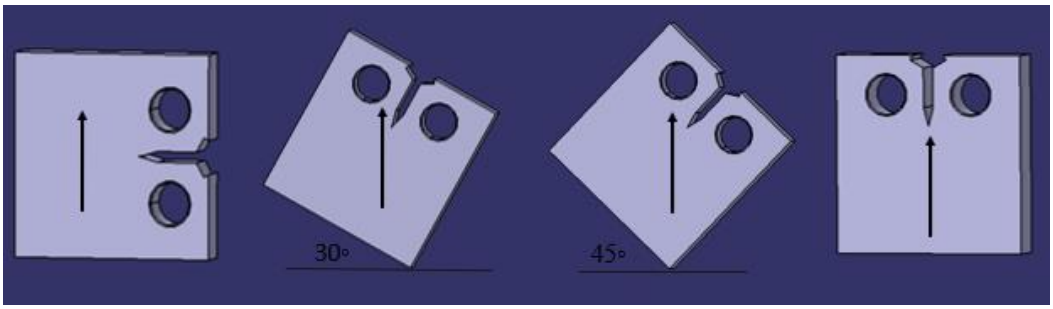

Figure 3-18. Crack growth test specimens with respect to build direction

Crack growth tests were performed using Rumul testing machine indicated in Figure 3.18. Samples were firstly pre-cracked per the requirement specified in ASTM E647-11 at the stress ratio R=0.1 under tension-tension cycle loading. Subsequently, fatigue crack propagation tests were conducted under cyclic load at f=80Hz with sin wave a constant load amplitude and the loading ratio R=0.1. The maximum load P_{max} is 6.36 kN. Figure 3-19 shows the test specimens with respect to orientation and arrows indicate the build direction.

The pre-crack length was monitored in all the FCG specimens using alternating current potential drop method with Matelect potential drop device shown in Figure 3.20 was used to monitor crack propagation. In this method, a constant current is passed through the specimen under test and the voltage difference across the crack front is created due to the crack propagation then the reduction of voltage is measured.

The fatigue crack growth test results comprise Paris-Erdoğan region constants (C and m), crack growth rate (da/dN). The coefficient “C” and the exponent “m” were obtained by drawing best linear line on the log (da/dN) versus log ΔK.

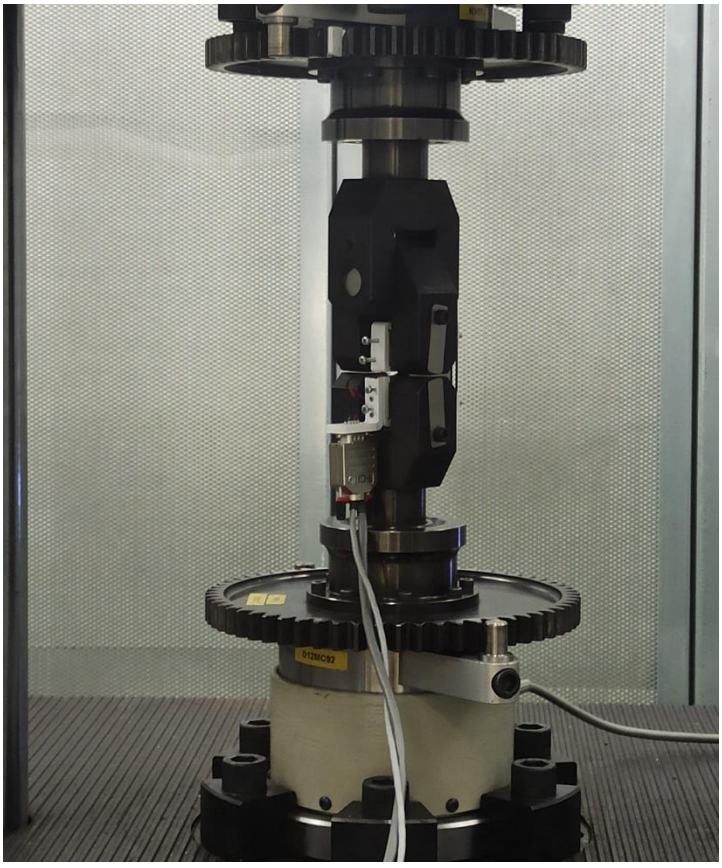

Figure 3-19. Rumul test machine and the attachment of specimen

Figure 3-20. Potential drop measurement device for crack growth monitor

3.8.1 Defect Analysis

The volumetric defect analysis of crack growth specimens was investigated prior to tests by using X-ray Computed Tomography which is a commercial product of X5000, North Star Imaging, Rogers. Additionally, all specimens were entirely scanned for two hours and only the front area of the notch represented in Figure 3.21 was analysed by using scanning parameters as shown in Table 3.6. Figure 3.21 also displays the CT machine.

Table 3-6. Computed tomography scan parameter for crack propagation specimens

Scanning Parameter	
Voltage	160kV
Current	230µm
Focal Spot size	36.8 microns
Focal Spot Mode	Microfocus
Zoom Factor	x3.24
# Projections	2160
# Frame Averaged	3
Filter	1 mm Al

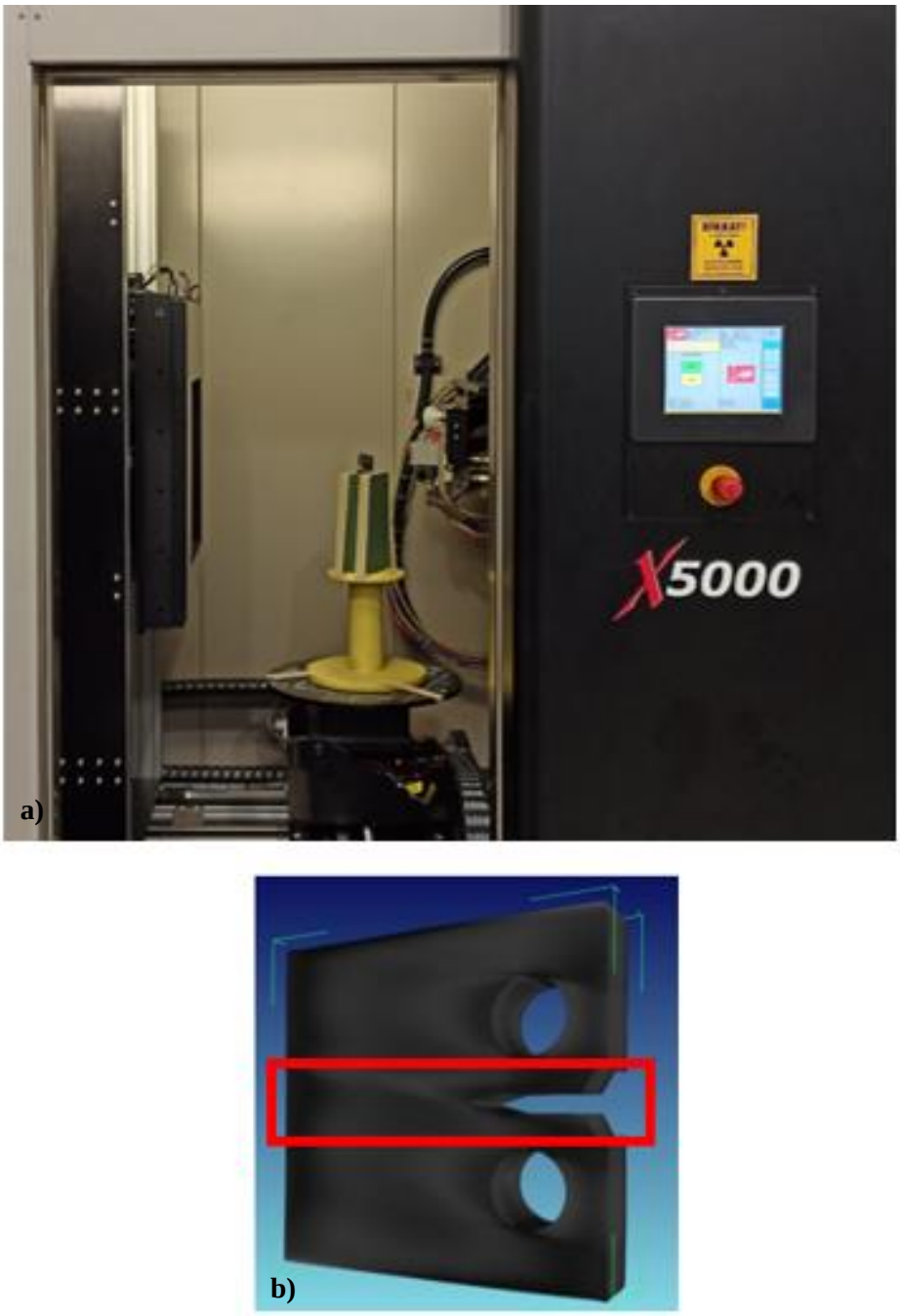

Figure 3-21. a) CT machine b) the representation of analysed region for all specimens marked with red square region

CHAPTER 4

RESULTS AND DISCUSSION

4.1 Microstructure Examination and Hardness Test Results

The optical micrographs of samples produced by EBM built at different angles are shown in Figure 4.1 and Figure 4.4. As seen from the images, β grains as marked with red dashes have elongated parallel to the building axes. Widmanstaten or basketweave morphology and lamellar structure were observed in the microstructure as represented in Figure 4-7 and Figure 4-8. Besides that, lack of fusion defects and voids were found as shown in Figure 4.5 and Figure 4.6 respectively.

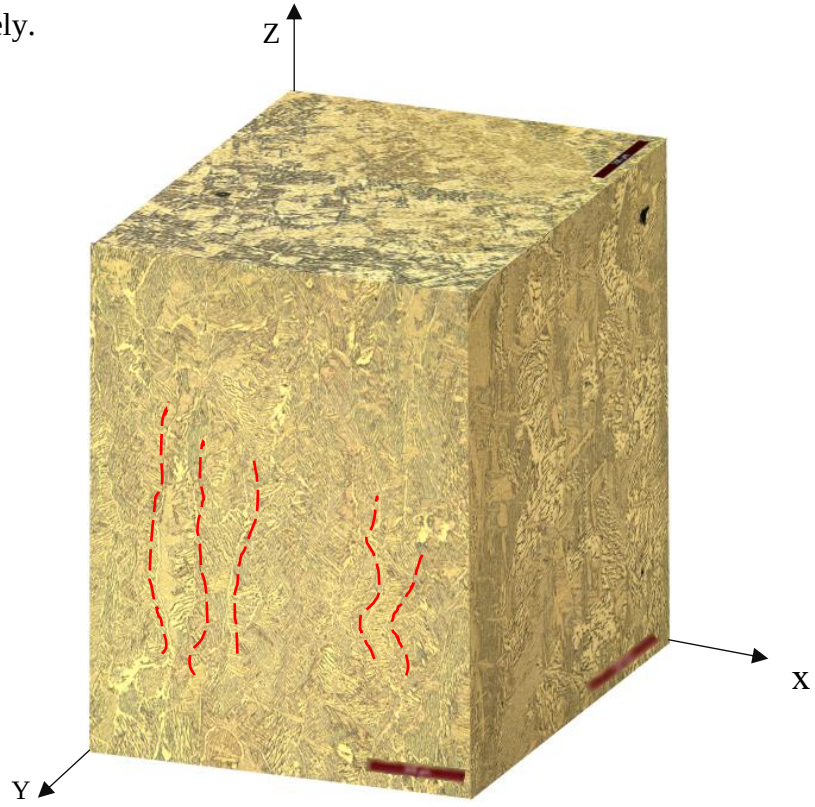

Figure 4-1. 3D Optical micrographs of specimen fabricated along 0^0 direction

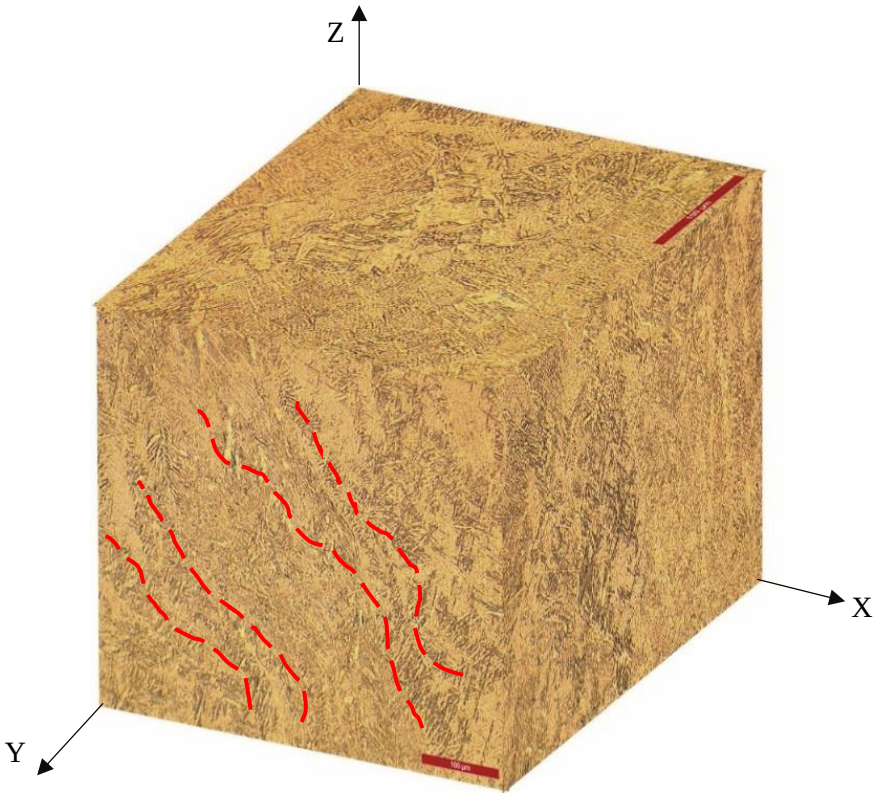

Figure 4-2. 3D Optical micrographs of sample fabricated along 30^0 direction

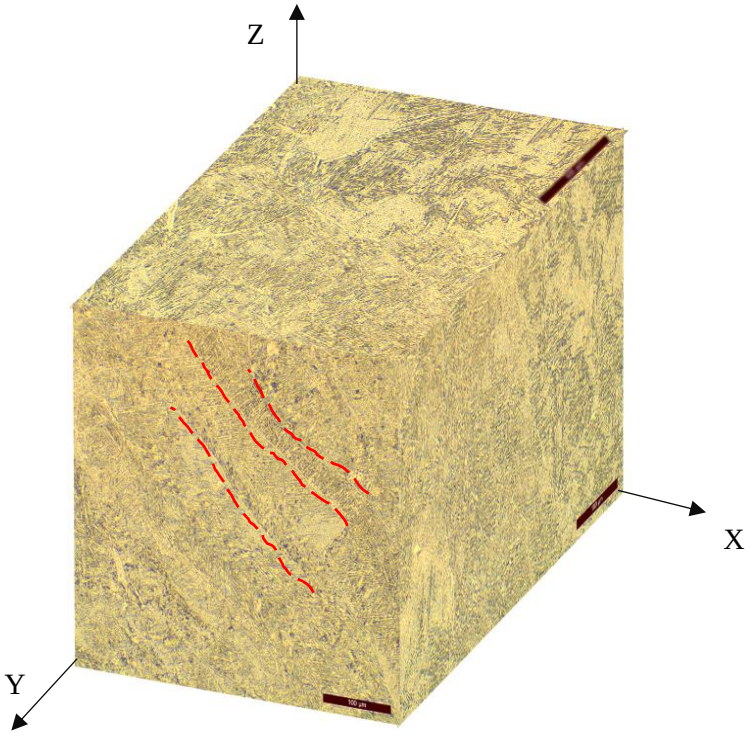

Figure 4-3. 3D Optical micrographs of 45T specimen

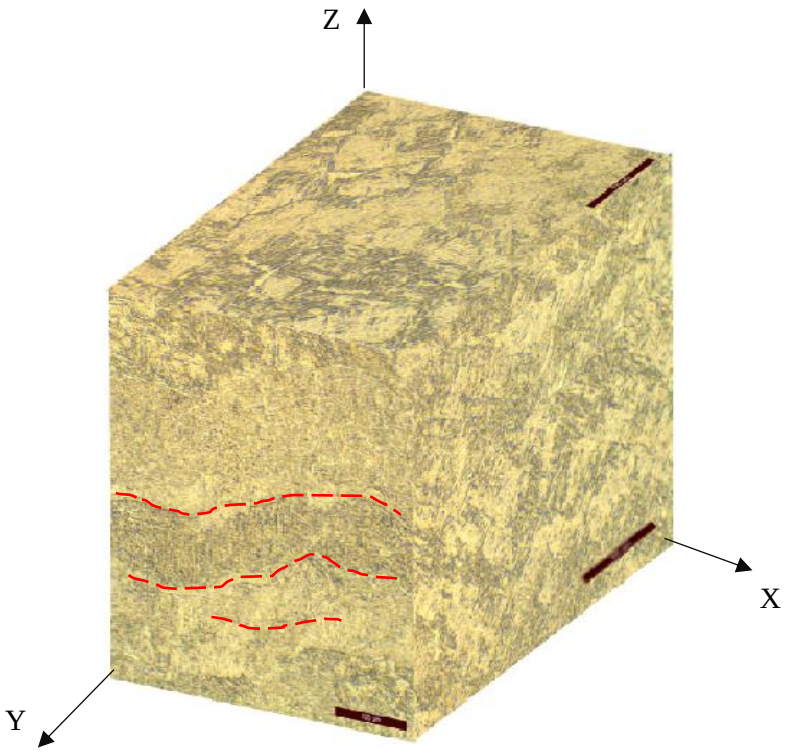

Figure 4-4. 3D Optical images of specimen fabricated at 90^0 direction

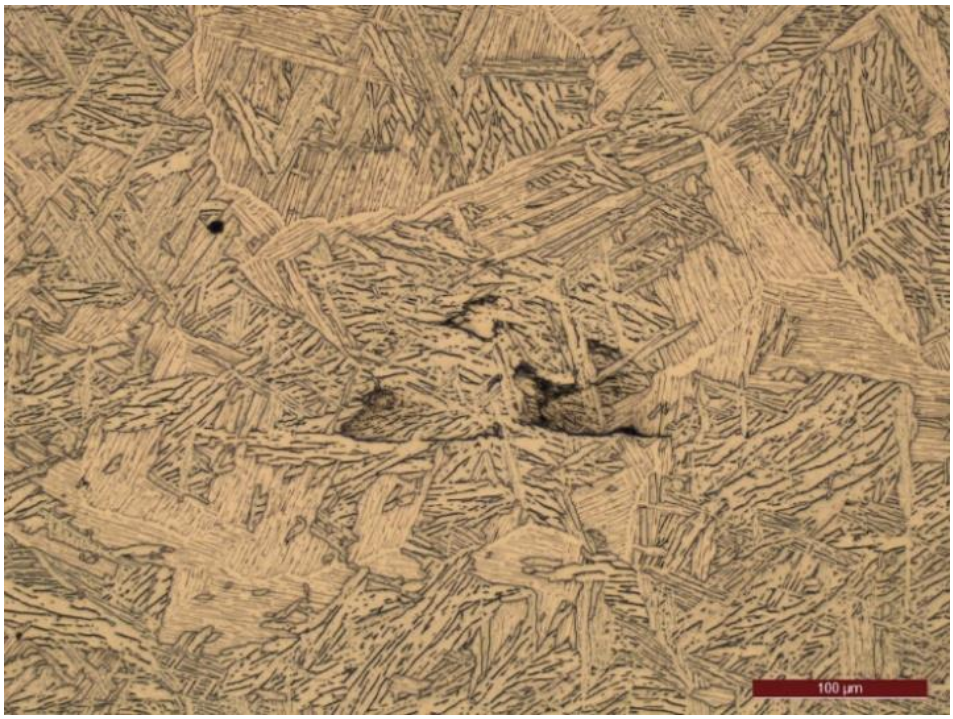

Figure 4-5. Lack of fusion for EBM processed specimens

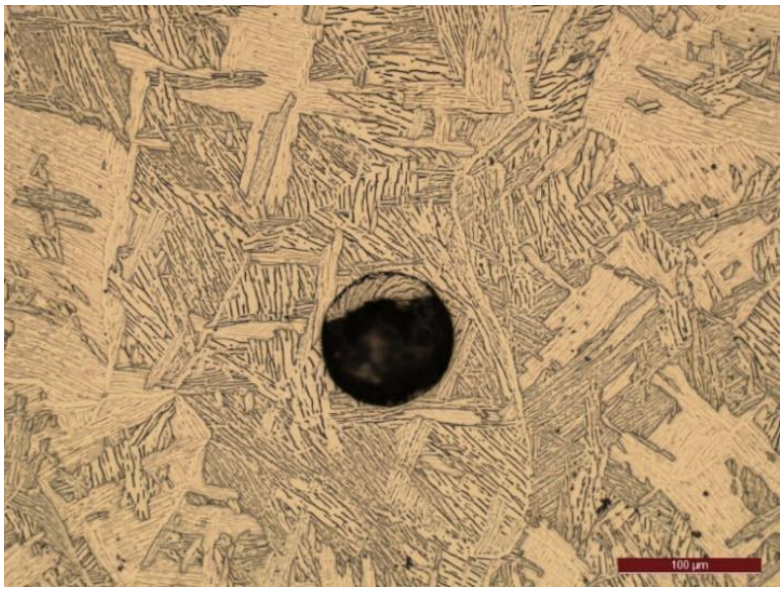

Figure 4-6. Void structure and unmelted powders in EBM processed specimens

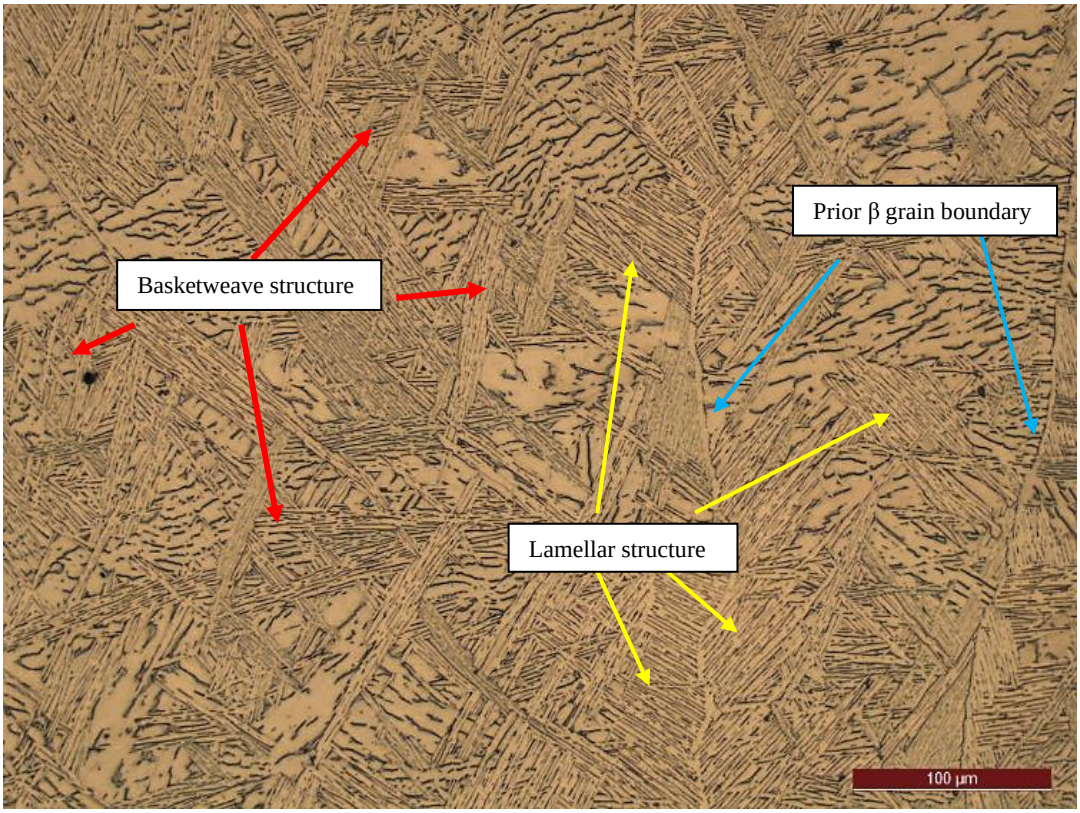

Figure 4-7. Optical image of EBM Ti-6Al-4V specimens. β phases are displayed black region whilist α phases are white regions. It is also noticed there are different size of phase laths.

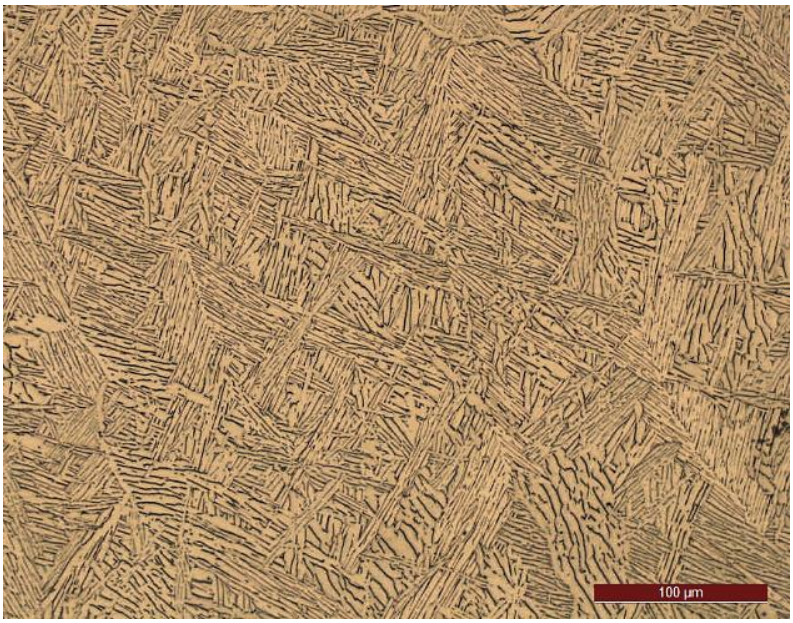

Figure 4-8. Widmanstaten or basketwave structure and lamellar morphology of EBM fabricated Ti6Al4V specimens

During EBM process, preheating stage and fabrication of specimens in vacuum chamber with 750^0C temperature provide almost equilibrum in the amount of α and β phases. Therefore, all specimens and three side of specimens (XZ, XZ and YZ) consisted of the same microstructure and consequently there was no clear differences in the hardness between four samples as shown in Figure 4.9.

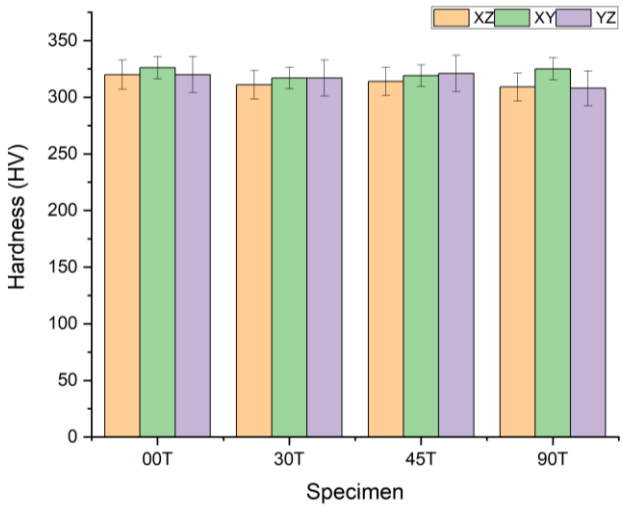

Figure 4-9. Hardness results of specimens

4.2 Tensile Test Results and Densification Measurement

The density values of EBM processed tensile test specimens at different directions were compared with 4.43 g/cm^3 [42], the standard density of Ti6Al4V. Table 4.1 includes the caldulated density and relative density values. The density of 00T specimen is a little bit higher than others and 30T, 45T and 90T have the same relative density.

Table 4-1. Densification results

Specimen	Density (g/cm^3)	Relative Density (%)
00T	4.405± 0.007	99.5
30T	4.396 ± 0.002	99.3
45T	4.398 ± 0.001	99.3
90T	4.397 ± 0.002	99.3

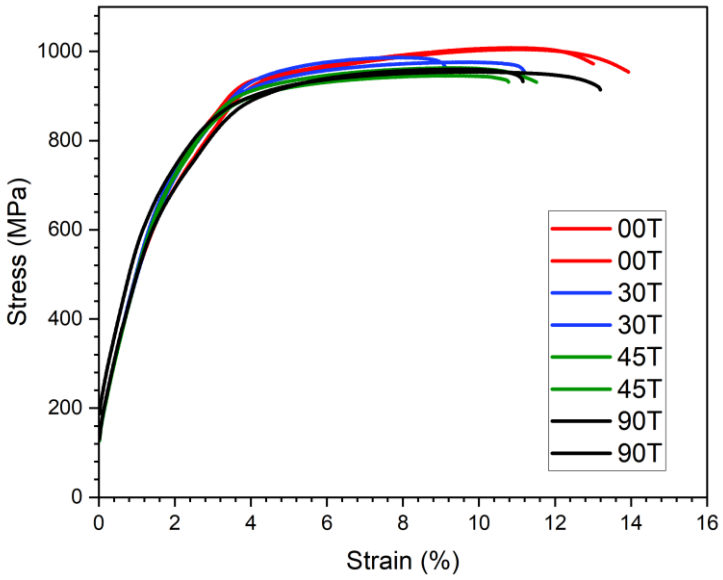

Figure 4-10. Stress-strain graphs

Table 4.2 contains the average tensile mechanical properties as yield strength(YS), ultimate tensile strength (UTS) and % elongation for specimens fabricated at different angles. According to this table, EBM built samples have higher yield and ultimate tensile strength values than ASTM F2924-14 standard values. For 00T specimen, it has more dense structure according to densification measurements as indicated in Table 4.1 and this can be related with the high amount of melted powders and the little amount of porosity. Therefore, specimens built at 0^0 angles have highest tensile strength and highest elongation. As can be seen from fracture surfaces in Figure 4-11 and Figure 4-26, EBM fabricated samples exhibit ductile fracture mechanism such as dimples. However, 30T specimens have different fracture surfaces indicated in Figure 13 and Figure 18. Consequently, large unmelted regions that cannot fused with next layer clarified the lowest elongation.

Table 4-2. Tensile results examined from curves in Figure 4.10

Specimen	0.2% YS (MPa)	UTS (MPa)	Elongation (%)
00T	866 ± 2	1006 ± 2	13 ± 2
30T	873 ± 8	981 ± 5	7 ± 3
45T	842 ± 4	955 ± 4	10 ± 1
90T	876 ± 6	957 ± 3	12 ± 1
ASTM F2924-14 (AM)	825	895	10
ASTM F1108-14 (Cast)	758	860	>8

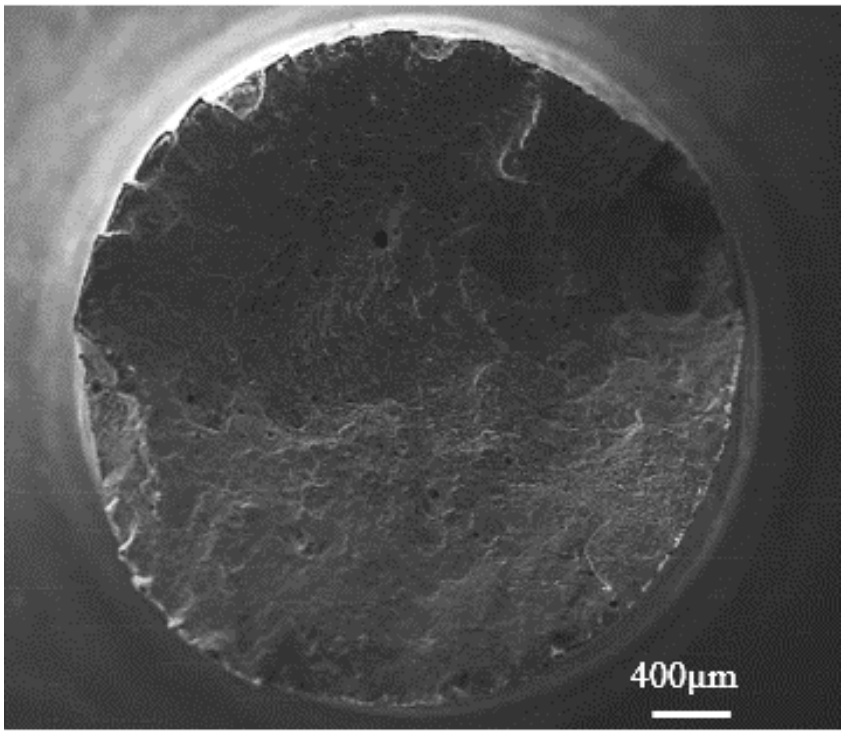

Figure 4-11. SEM images of 00T tension test specimen fracture surface

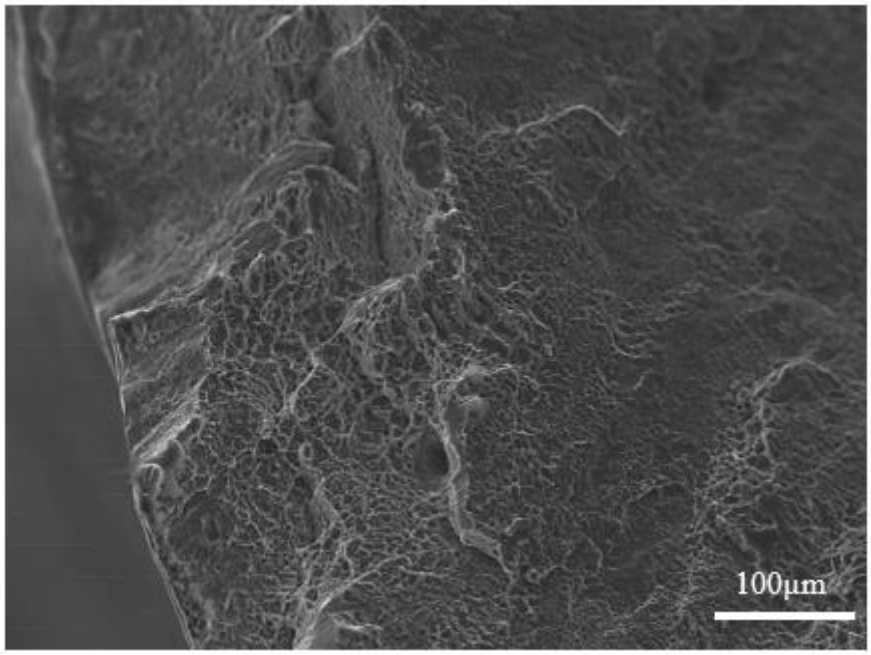

Figure 4-12. Porosity and dimples on 00T fracture surface

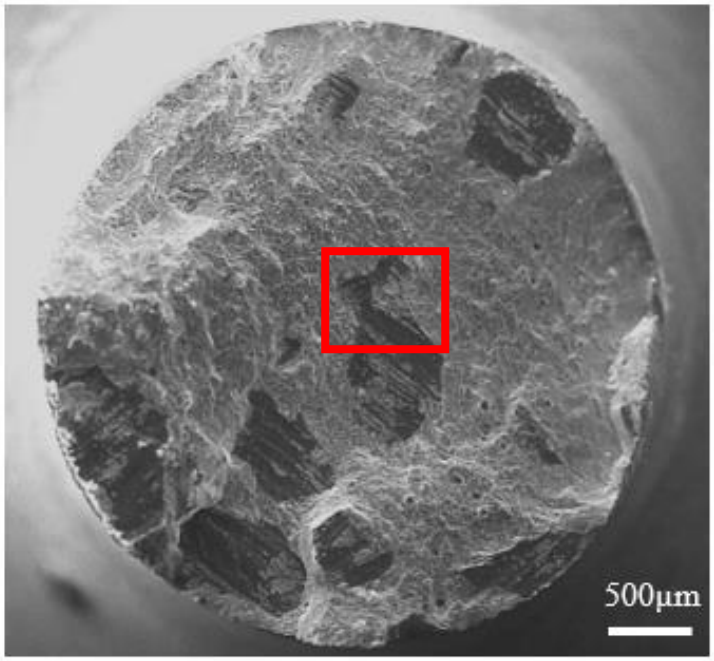

Figure 4-13. SEM images of 30T tension test specimen fracture surface

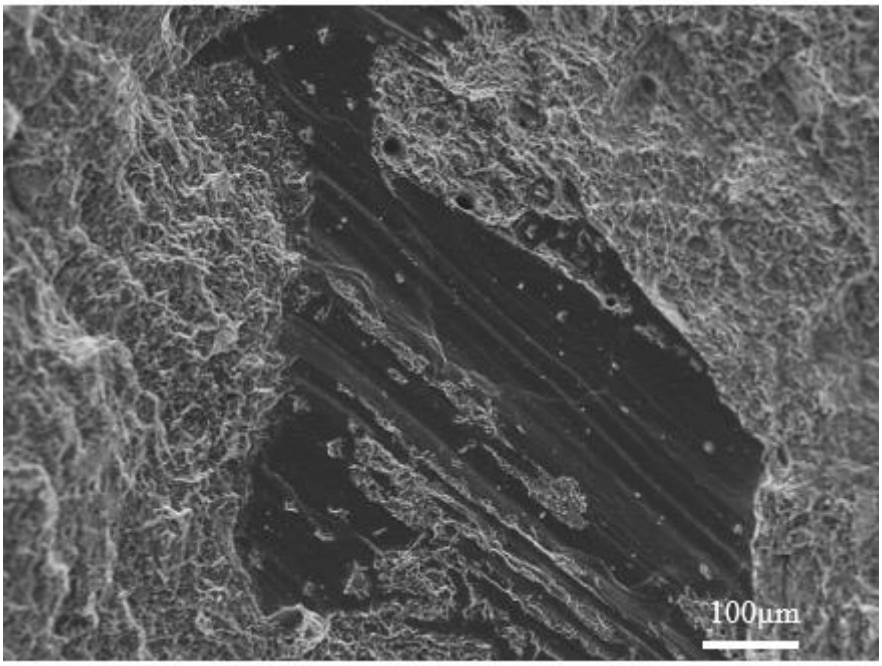

Figure 4-14. Dimples, voids and large surfaces that cannot fused with the next layer for 30T specimen. These unmelted large surfaces account for nearly 25 % of total fracture surface.

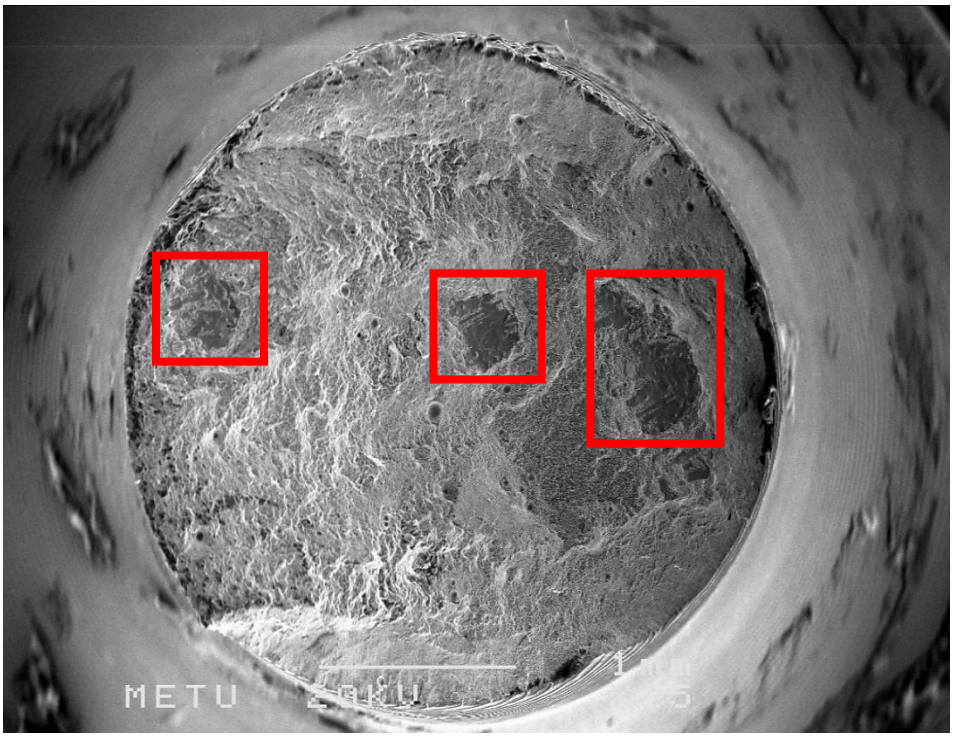

Figure 4-15. General view of 30T tension test specimen fracture surface with insufficient melt regions which consisted of about 15% of total surface.

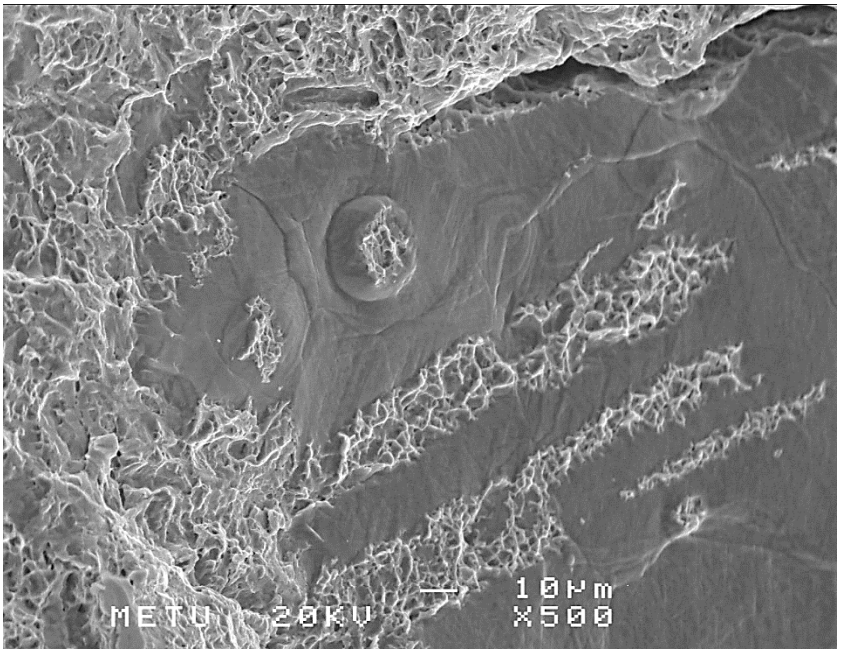

Figure 4-16. Dimples structure and unbonded regions resulted from insufficient melting. This may be a result of difference in local cooling during the process.

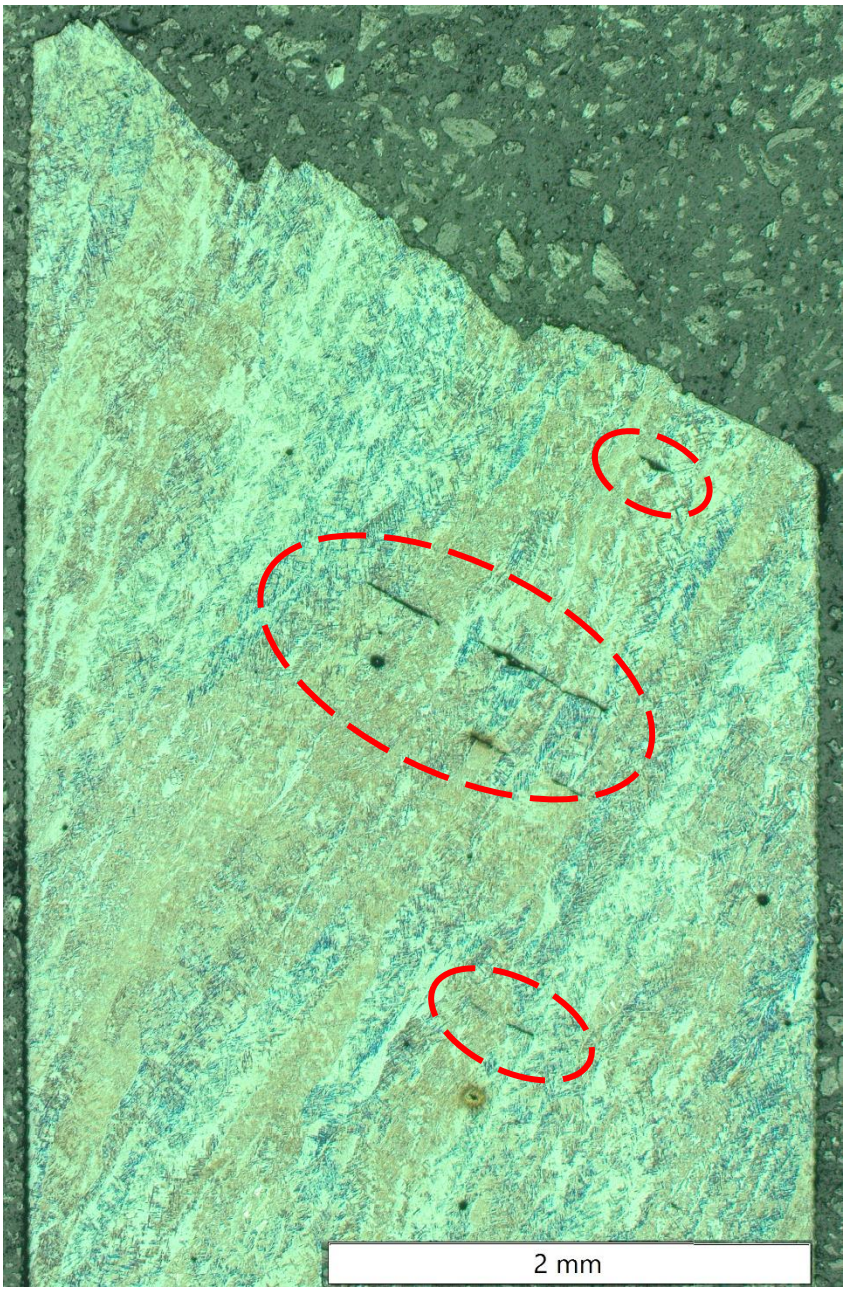

Figure 4-17. The vertical cut image of 30T tension test specimen.

In Figure 4-17, it is clearly observed that grains have elongated along built direction. Furthermore, fracture plane is parallel to production layer because of insufficient melted regions shown in red dashes. Figure 4-14, Figure 4-16 and Figure 4-18 indicate the top view of these red dashes. Light regions represent alpha phases while beta phases are displayed by dark regions.

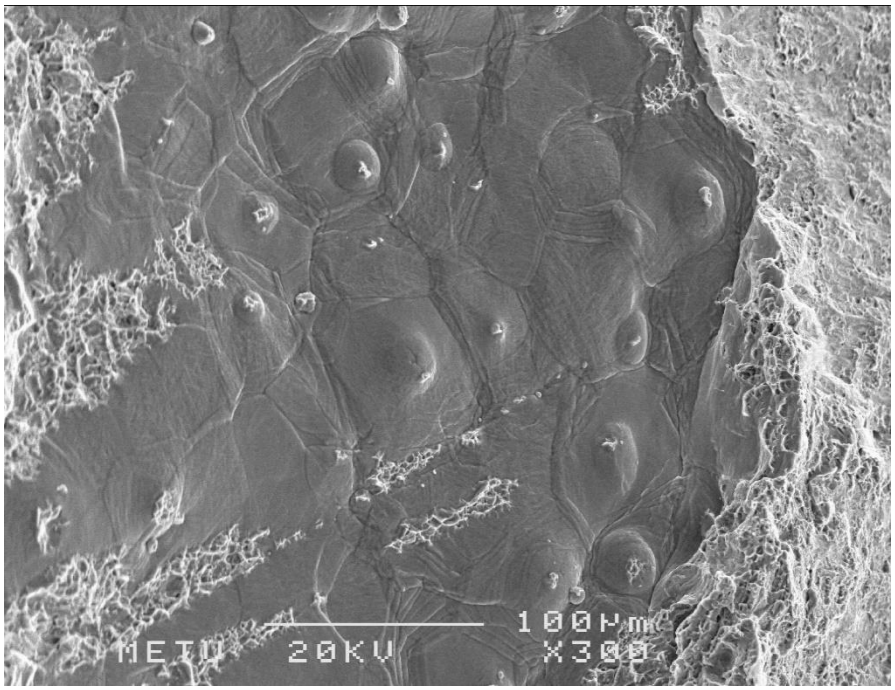

Figure 4-18 Unmelted particle islands. This is due to insufficient heat input to melt and bond powders.

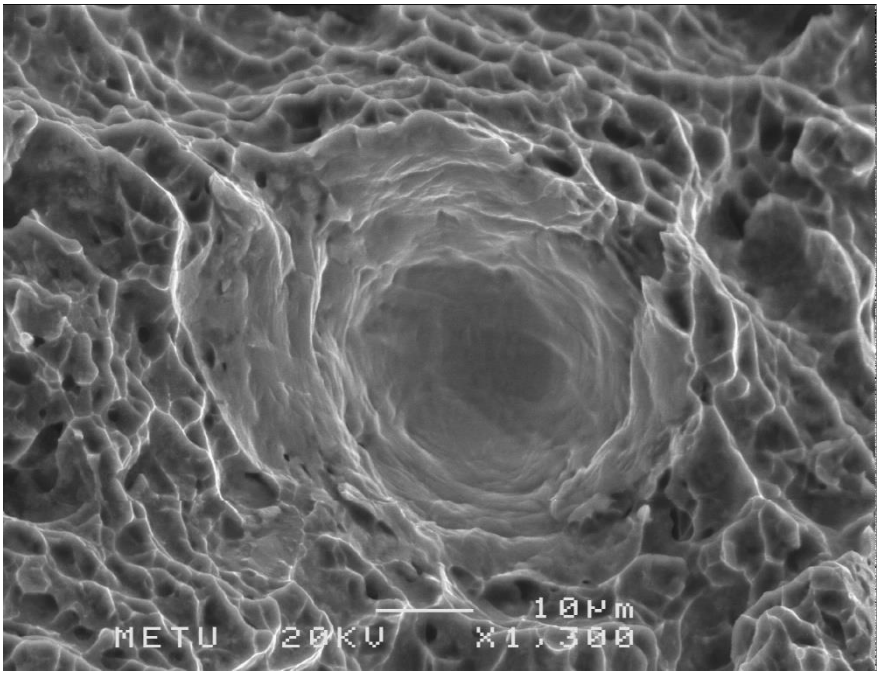

Figure 4-19 Void structure on the fracture surface for 30T specimen

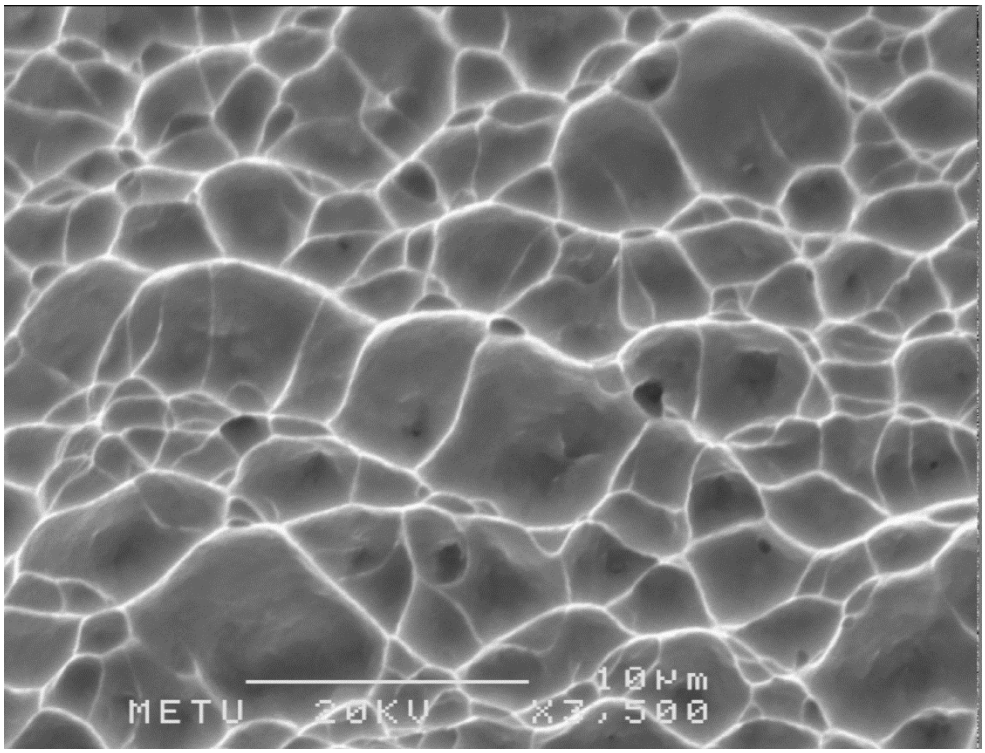

Figure 4-20. The dimple structures on the fracture surface of EBM-Ti6Al4V fabricated at 30^0angle.

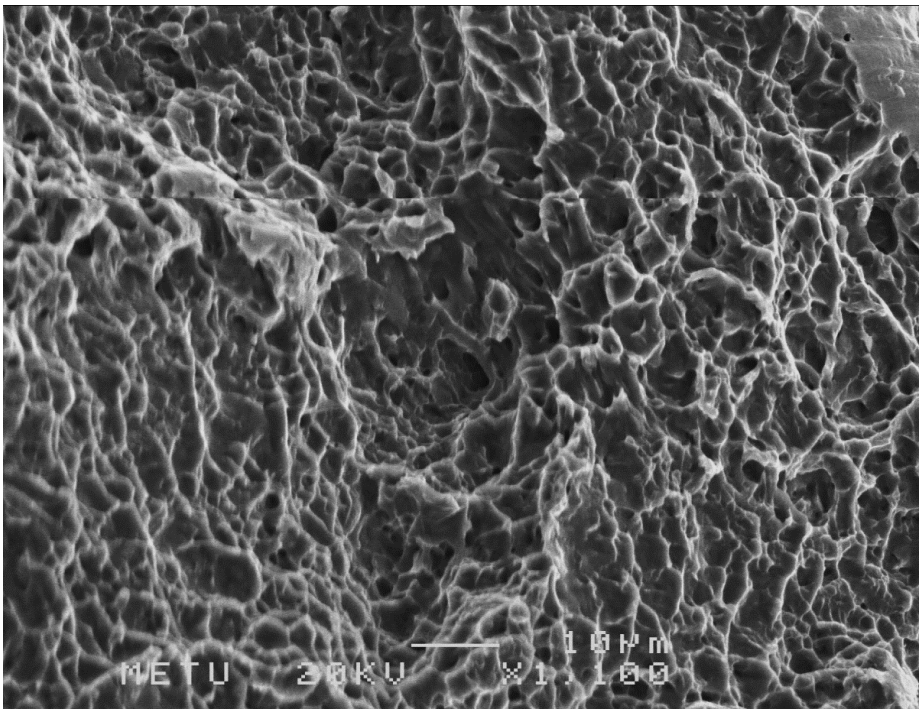

Figure 4-21 Ductile fracture surface at 1100X magnification for 30T

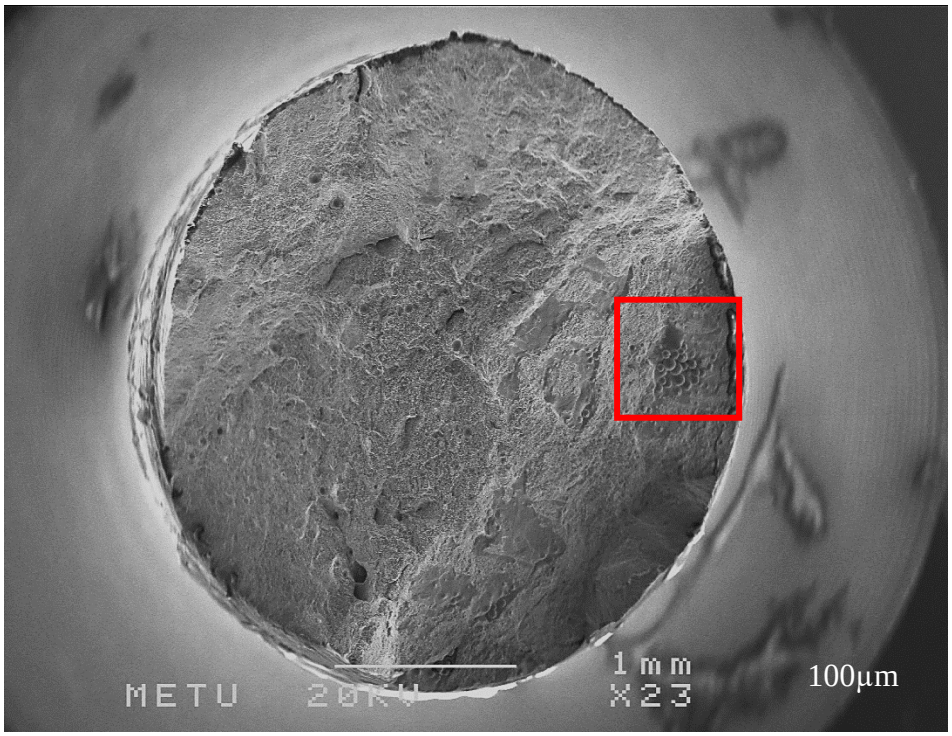

Figure 4-22 General SEM image of 45T specimen

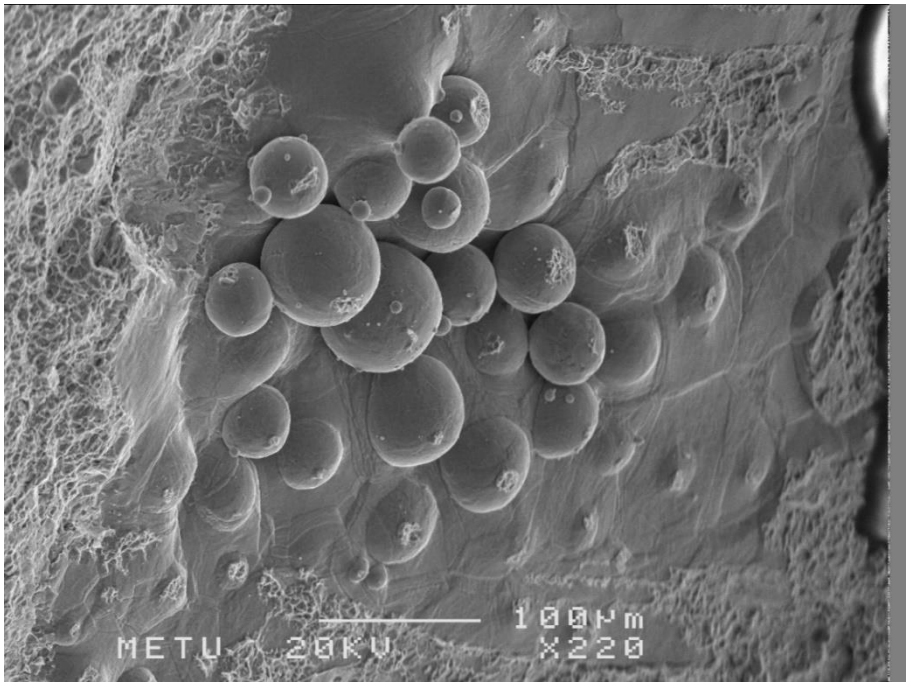

Figure 4-23 Unmelted powder particles at the edge of the fracture surface of 45^0 angle built specimen.

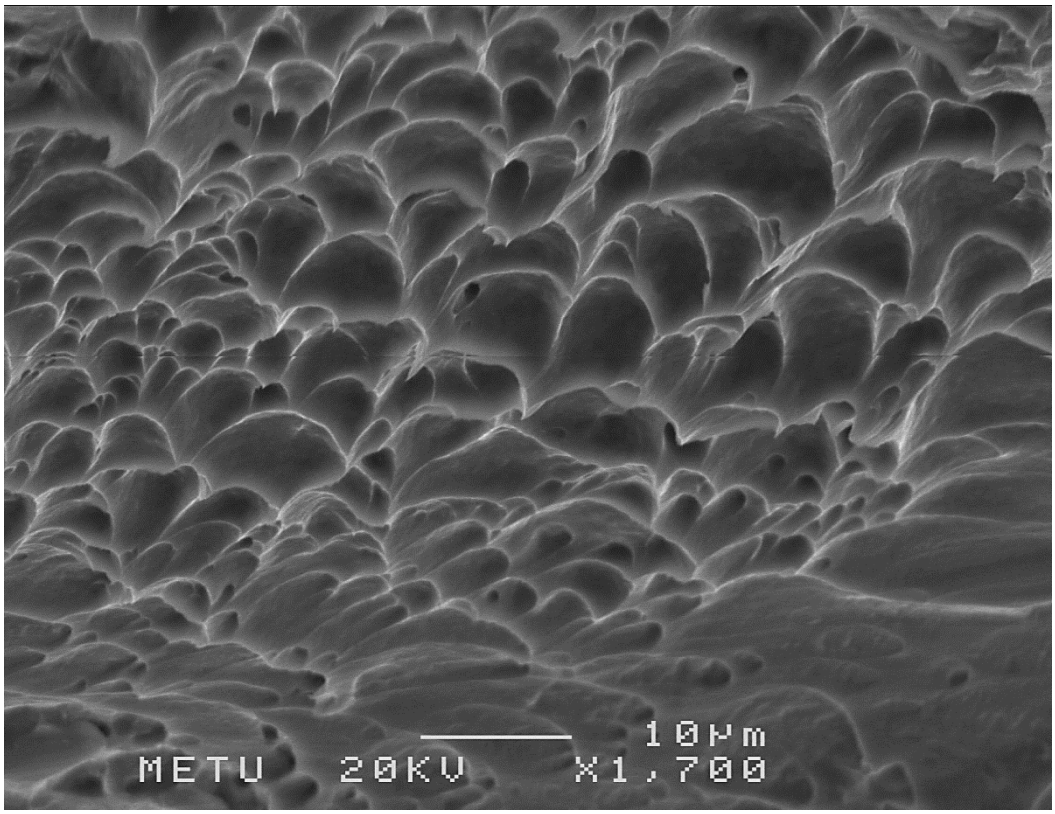

Figure 4-24 Angularly elongated dimples on the fracture surface. The evidence of the relation between the fracture plane and layers produced with 45^0 angle.

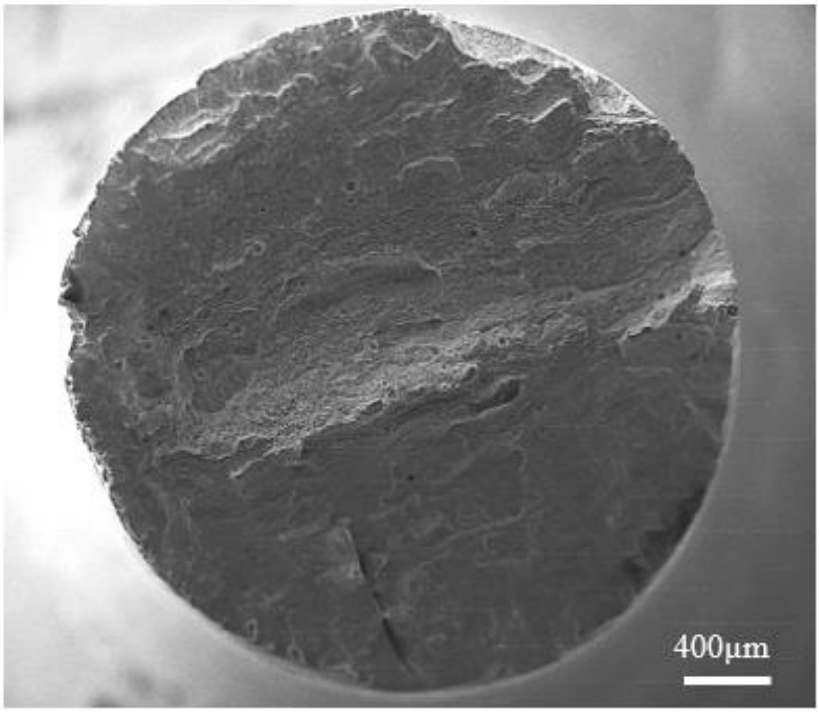

Figure 4-25. SEM images of 90T tension test specimen fracture surface

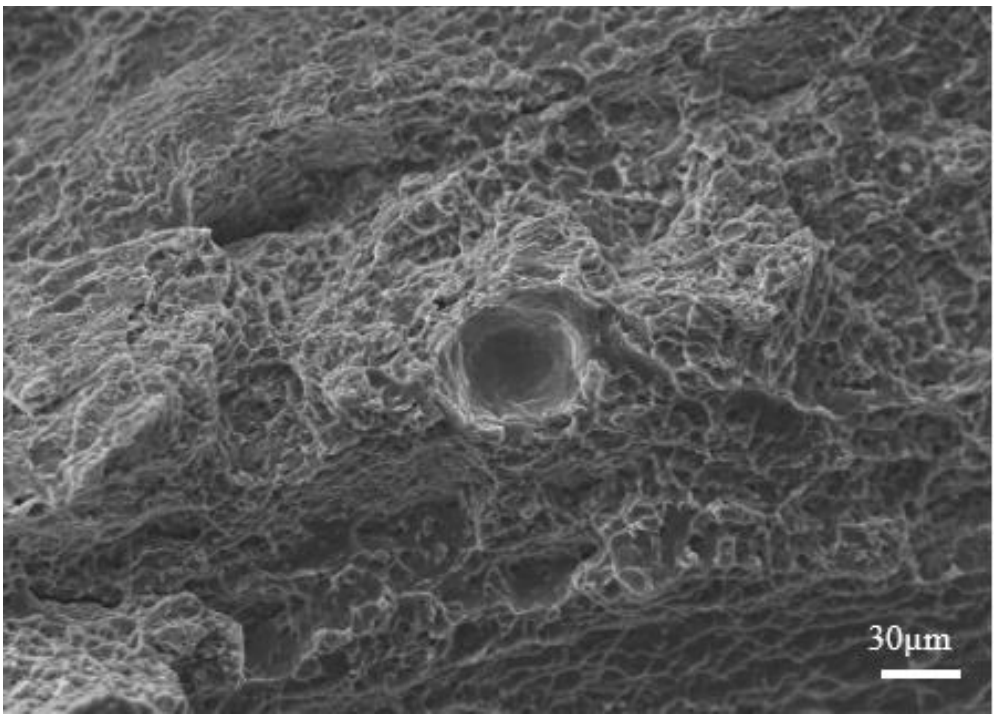

Figure 4-26. Porosity, dimples and small cracks on 90T fracture surface

4.3 Fracture Toughness Test Results

The fracture toughness values of the EBM fabricated specimens at different angles examined in this study are similar to literature studies.[30][31][33]. According to Table 4-3 comparing the findings, the study's results have higher than forged Ti6Al4V bar. Despite of these calculated results, plain strain conditions specified in ASTM E399 are not satisfied because of thickness requirement. Thicker specimens should be tested to determine the valid K_{1c}.

Table 4-3. Fracture toughness test results

Condition	Specimen Type	Specimen orientation	K_Q (MPa$\sqrt{m}$)
As built, machined,	CT	00T	92.5
		30T	83
		45T	92
		90T	88
Mill annealed, forged bar [3]	-	L-T	42-84
Mill annealed, forged bar [3]	-	T-L	36-89

4.4 Crack Growth Rate Results

4.4.1 Crack Length vs. Number of Cycles

Crack length for specimens were measured by alternating current potential drop method during experiments. Crack length versus number of cycle plots are shown in Figure 4.27-4.30.

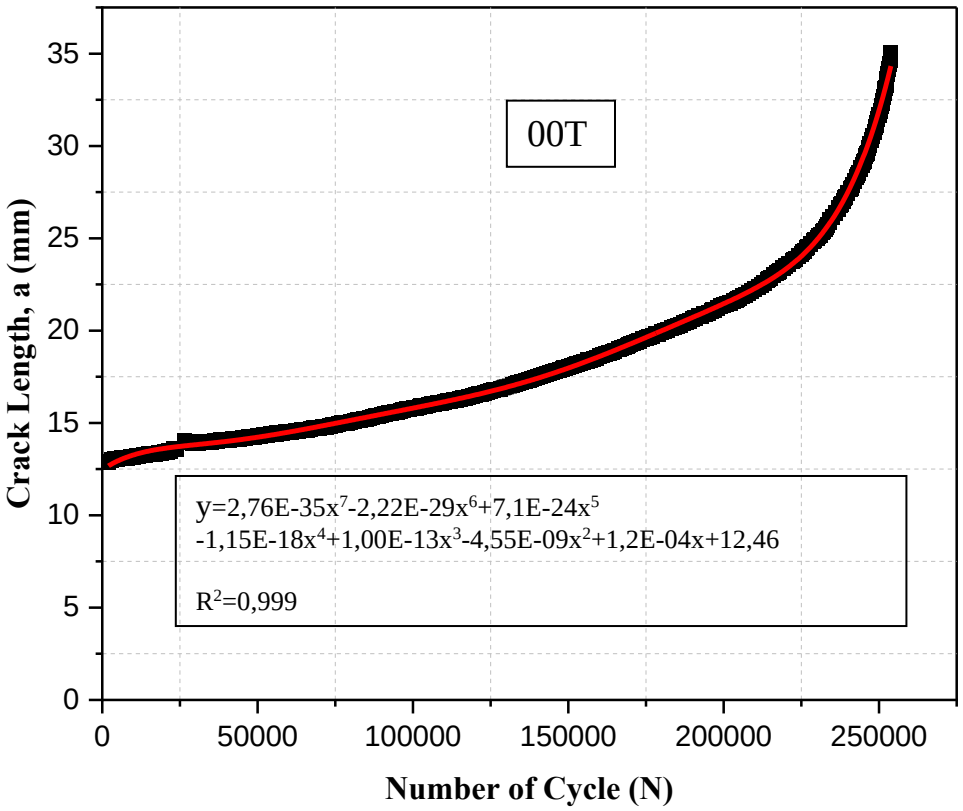

Figure 4-27. Crack length vs number of cycle of 00T specimen

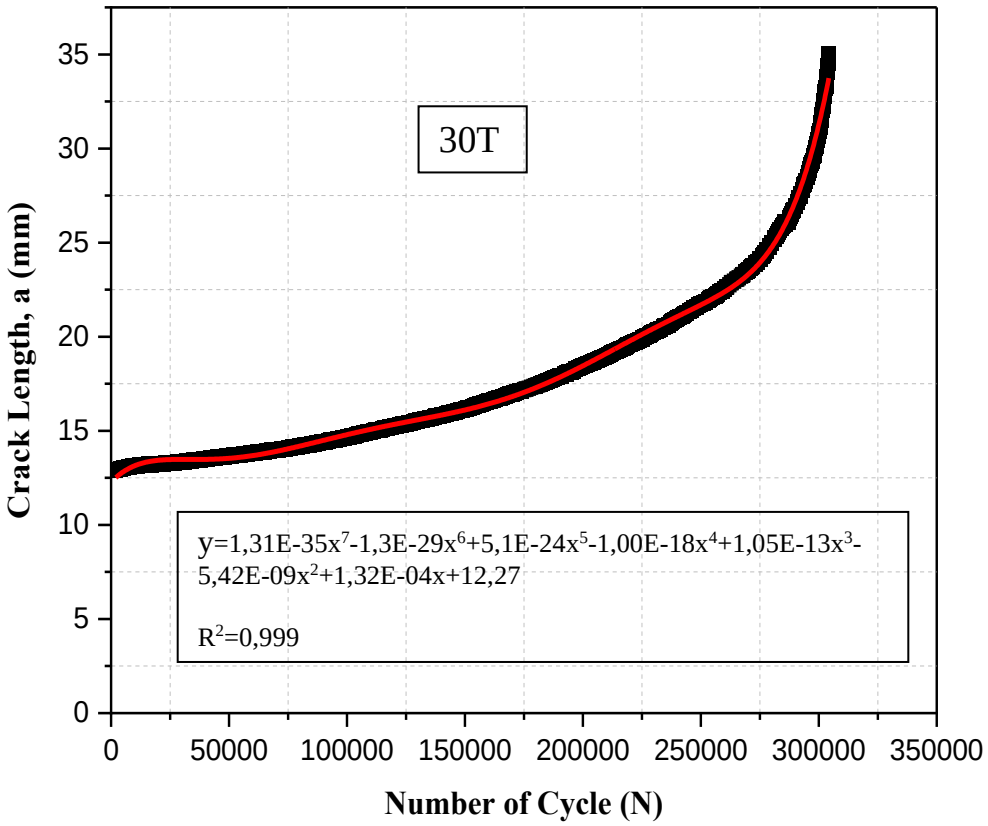

Figure 4-28. Crack length vs number of cycle of 30T specimen

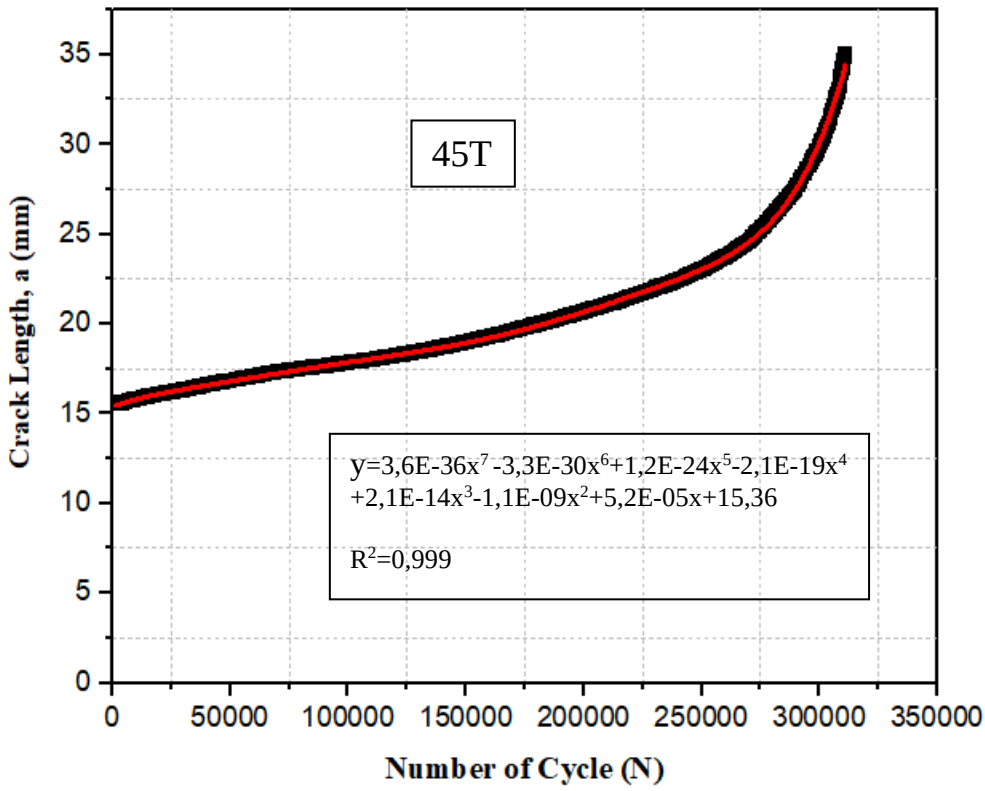

Figure 4-29. Crack length vs number of cycle of 45T specimen

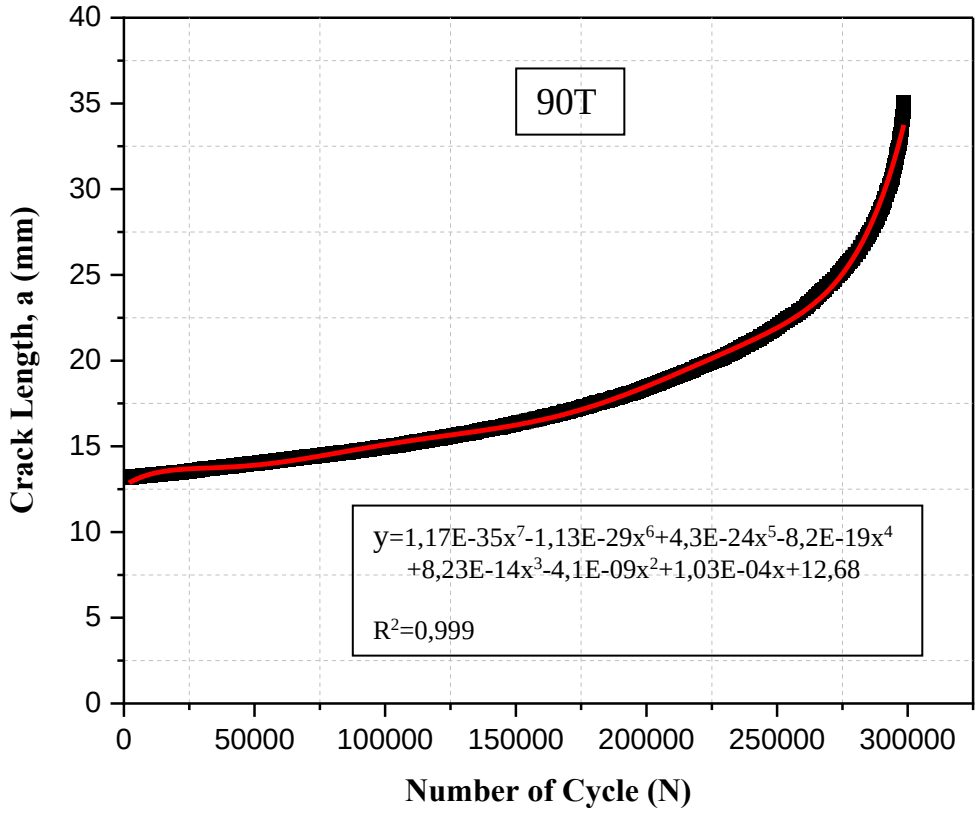

Figure 4-30. Crack length vs number of cycle of 90T specimen

4.4.2 Crack Growth Rate vs. Stress Intensity Range Graphs

Incremental polynomial technique mentioned in ASTM E647-15 was benefited to computer data reduction for crack growth rates vs. stress intensity range plots These curves within logarithmic scale are represented in Figure 4.31-4.34

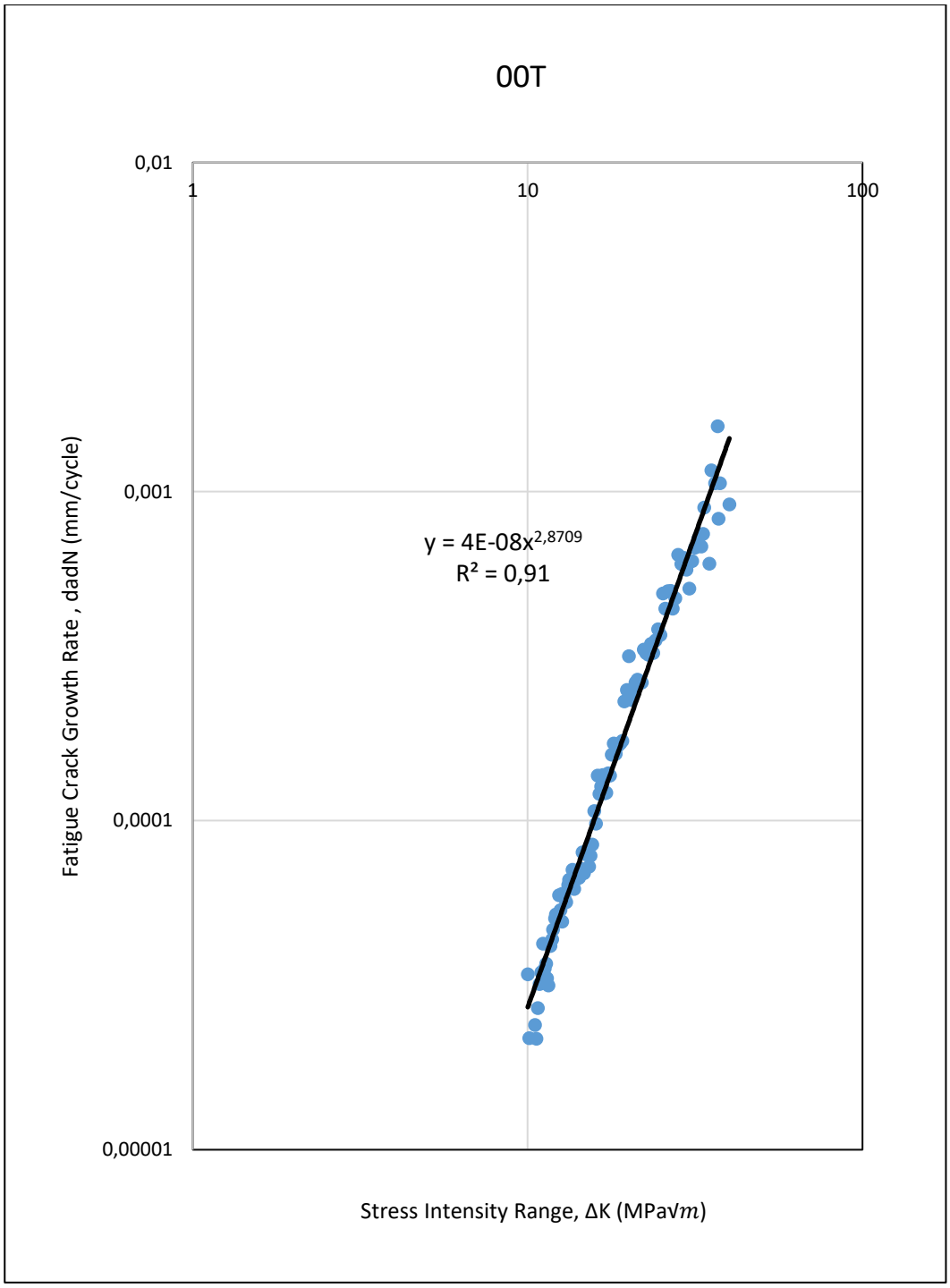

Figure 4-31. da/dN vs.ΔK plot for 00T specimen

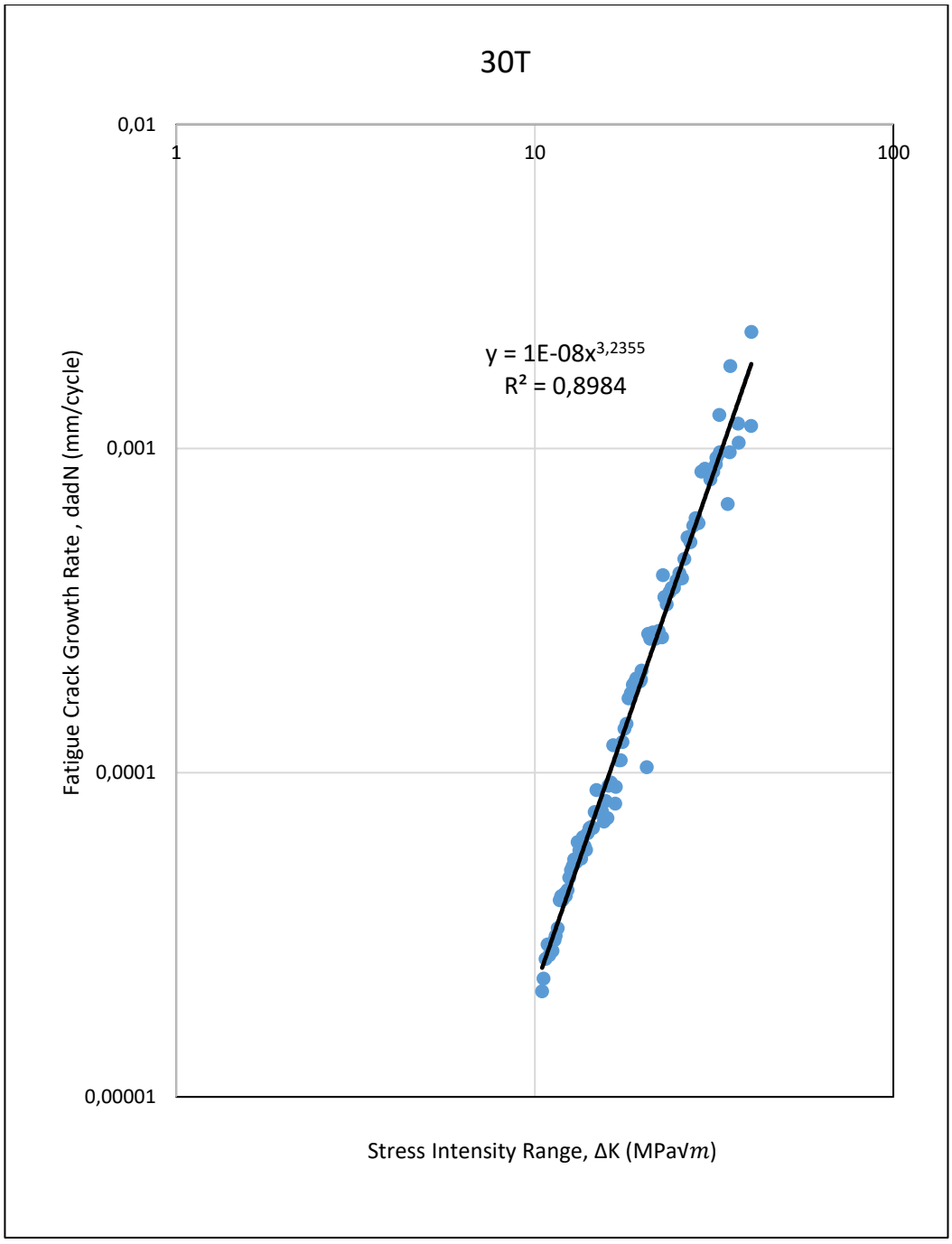

Figure 4-32. da/dN vs.ΔK plot for 30T specimen

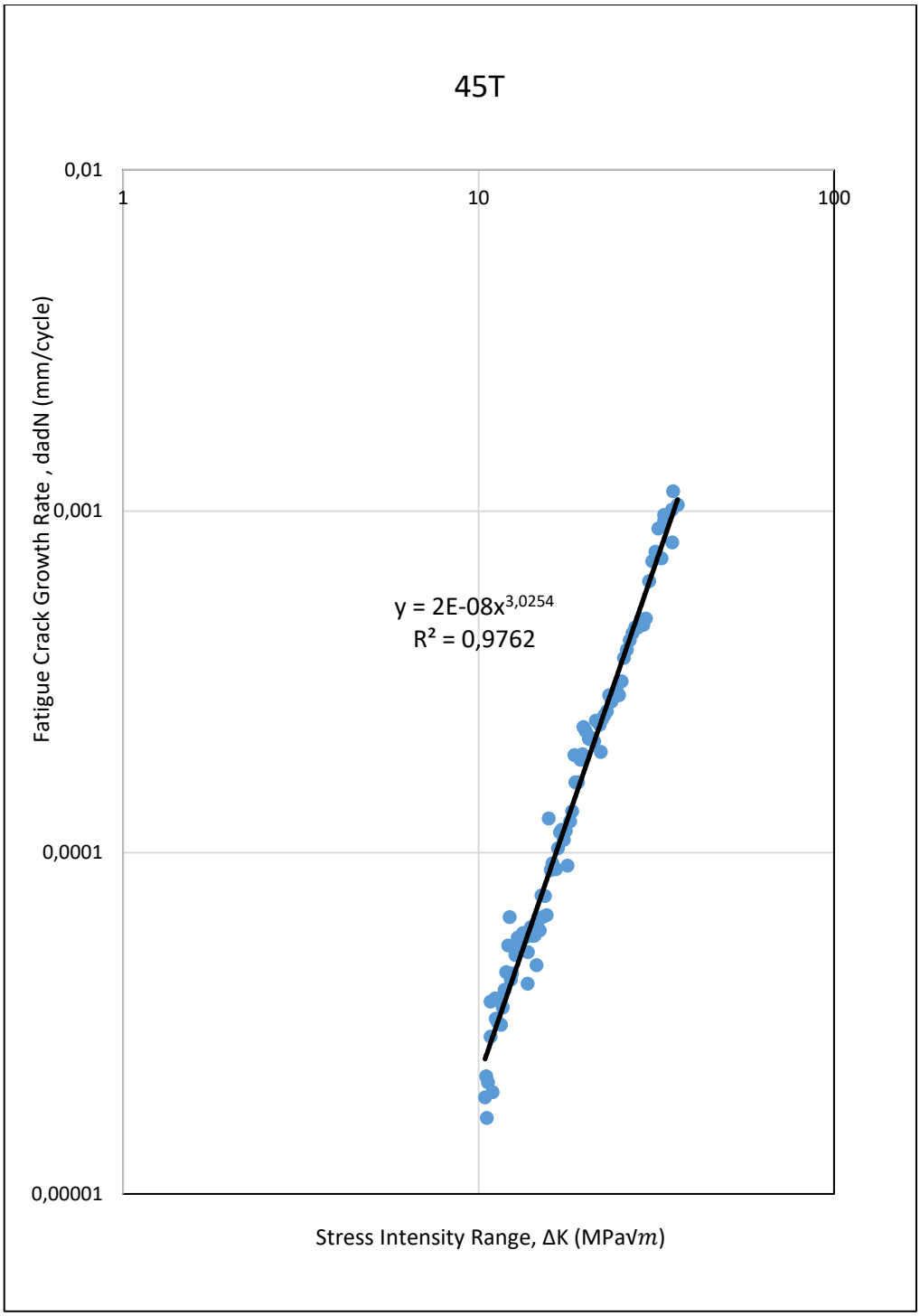

Figure 4-33. da/dN vs.ΔK plot for 45T specimen

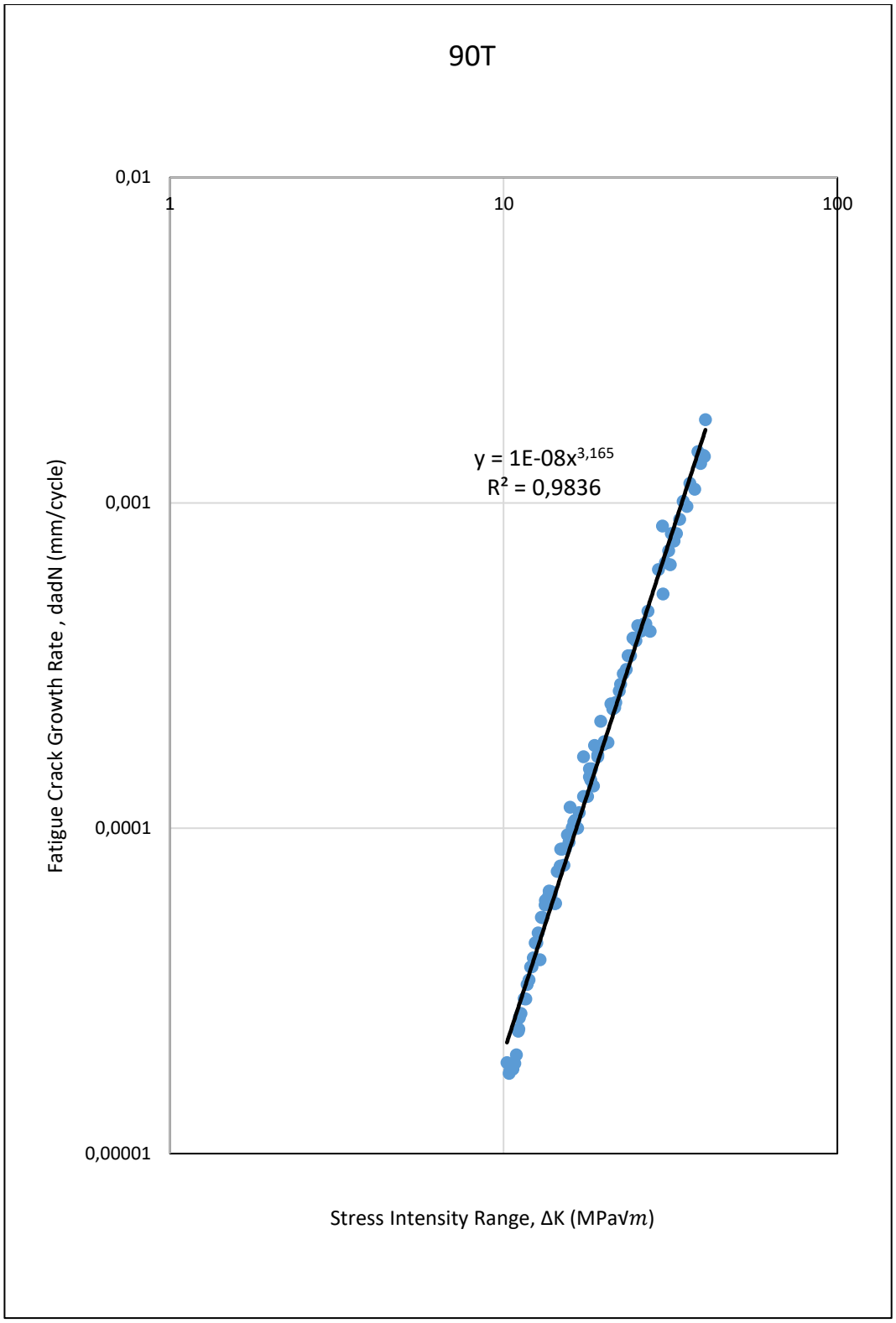

Figure 4-34. da/dN vs.ΔK plot for 90T specimen

4.4.3 Paris-Erdoğan Law and Comparison of da/dN – ΔK Curves

Regarding crack growth rate test, Figure 4.35 represents the comparison of da/dN – ΔK of EBM fabricated specimens. Table 4.4 also summarizes the experimentally calculated Paris-Erdoğan region constants, C and m.

Paris-Erdoğan Equation:

$$\frac{da}{dN} = C(\Delta K)^m$$

Table 4-4. Paris-Erdoğan regime constants of specimens

Specimen	C	m	R^2	$\frac{da}{dN} = C(\Delta K)^m$
00T	4.013E-08	2.87	0.91	$4.013E\text{-}08(\Delta K)^{2.87}$
30T	1.412E-08	3.24	0.89	$1.412E08(\Delta K)^{3.24}$
45T	2.433E-08	3.03	0.97	$2.433E\text{-}08(\Delta K)^{3.03}$
90T	1.423E-08	3.17	0.98	$1.423E\text{-}08(\Delta K)^{3.17}$

Table 4-5. Crack propagation rates at different ΔK

Specimen	da/dN ($\Delta K =$ 20 MPa$\sqrt{m}$)	da/dN ($\Delta K =$ 25 MPa$\sqrt{m}$)	da/dN ($\Delta K =$ 30 MPa$\sqrt{m}$)	da/dN ($\Delta K =$ 40 MPa$\sqrt{m}$)
00T	$1.988x10^{-4}$	$3.746x10^{-4}$	$6.288x10^{-4}$	$1.423x10^{-3}$
30T	$1.996x10^{-4}$	$4.067x10^{-4}$	$7.275x10^{-4}$	$1.821x10^{-3}$
45T	$1.780x10^{-4}$	$3.452x10^{-4}$	$5.932x10^{-4}$	$1.394x10^{-3}$
90T	$1.838x10^{-4}$	$3.721x10^{-4}$	$6.621x10^{-4}$	$1.643x10^{-3}$

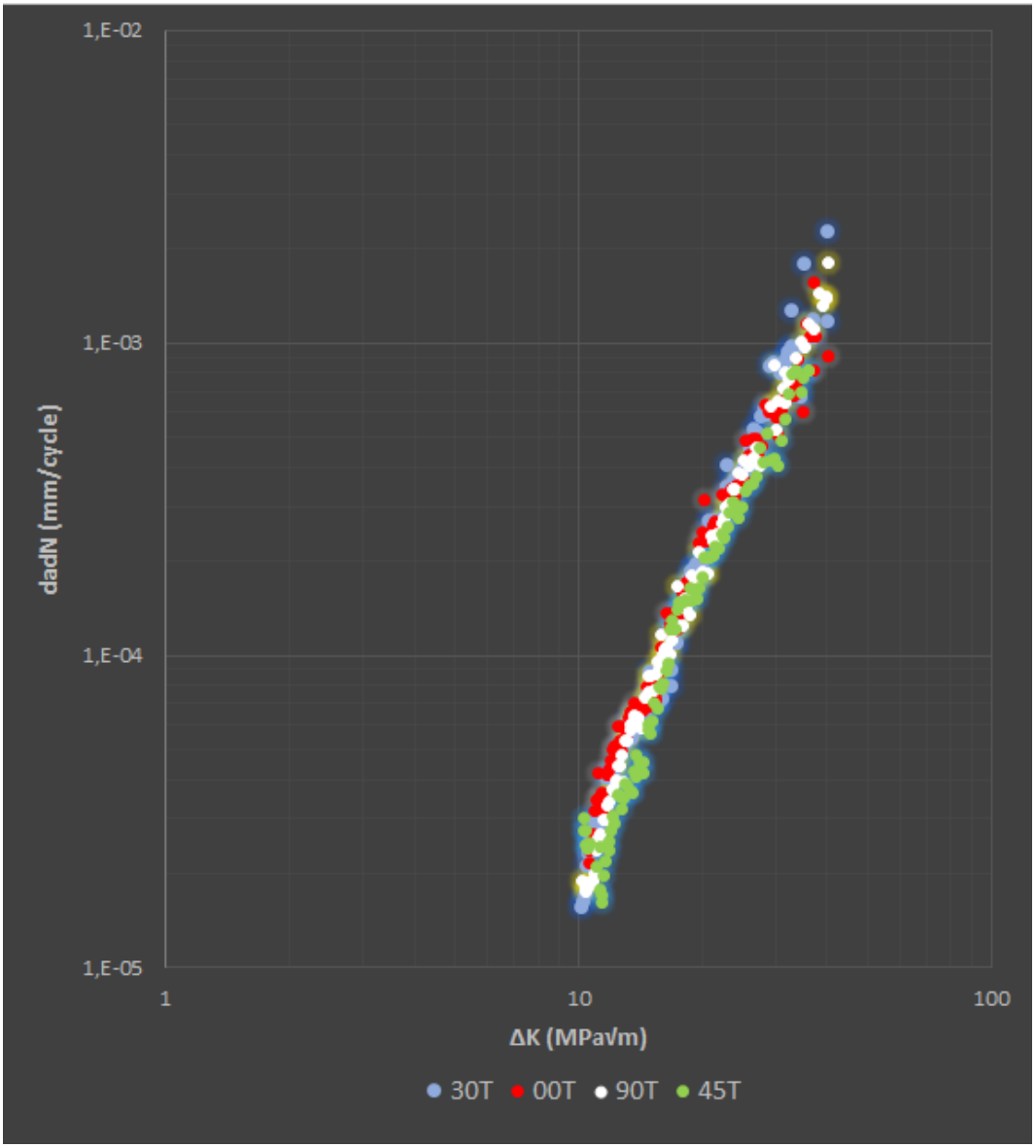

Figure 4-35. Comparison of da/dN – ΔK graphs

According to Figure 4.35, although FCGR graphs of four specimens interferences with each other, there are more fluctuation in the curve of 30T specimen. As a result of Table 4.4, the crack growth rate of 30T is faster than that of other specimens and the slower rate is observed in the 45T specimen when ΔK is calculated from 20 MPa$\sqrt{m}$ to 40 MPa$\sqrt{m}$ as indicated in Table 4-5.

Additionally, at the same stress intensity ranges 90T specimen is more resistant to the propagation of crack by comparison with 00T specimen.

It can be inferred that rapid crack propagation of 30T specimen correlates its the low toughness among other specimens.

According to CT results summarized in Table 4.6, although analysed material volume for 45T is higher than others, the lowest porosity volume is measured in 45T. As can also be examined from CT statistics indicated in Appendix A-D, 45T specimen has lowest number of porosity with respect to diameter. It can be concluded that 45T specimen has the lowest rate of crack propagation according to Table 4-5 due to its high fracture toughness indicated in Table 4.3 and its low porosity rate.

While 00T has more toughness and less porosity volume than 90T specimen, it exhibits low resistance of crack propagation when compared to 90T and thus there cannot be deduced a reliable result. However, porosity location and porosity shape inside the body is likely to cause this.

In the light of the findings in Table 4.5, crack propagation rate at low ΔK values (ΔK=20 MPa√m) provide consistency with the requirement of aerosapce components. However, the rate of crack propagation is higher than aerospace design requirements at high ΔK values (ΔK=30 MPa√m and ΔK=40 MPa√m)

Table 4.6. CT results of four specimens

Specimen	Material Volume (mm^3)	Defect Volume (mm^3)	Porosity volume ratio (%)
00T	2400.34	4.22	0.18
30T	2297.71	6.86	0.30
45T	2521.29	2.16	0.09
90T	2369.09	10.10	0.42

4.5 Fractography

The fracture surface of four specimens were investigated with digital and Scanning Electron Microscope (SEM). The differences between macroscopic images demonstrated in Figure 4-36 and Figure 4-39 were resulted from the scanning strategies of the ARCAM Company algorithm. Fracture surfaces obtained from both toughness tests and FCG rate tests are confirmed each other. The light regions mean the unmelted powders related to lack of fusion while voids and gas porosities are positioned in dark regions. During fast crack regimes, dimples demonstrated in Figure 52 were observed in all of specimens. Additionally, the evidences of fatigue failure including fatigue striations, tear ridges and secondary cracks were examined in Paris regime as shown in Figure 4-40 and Figure 4-51.

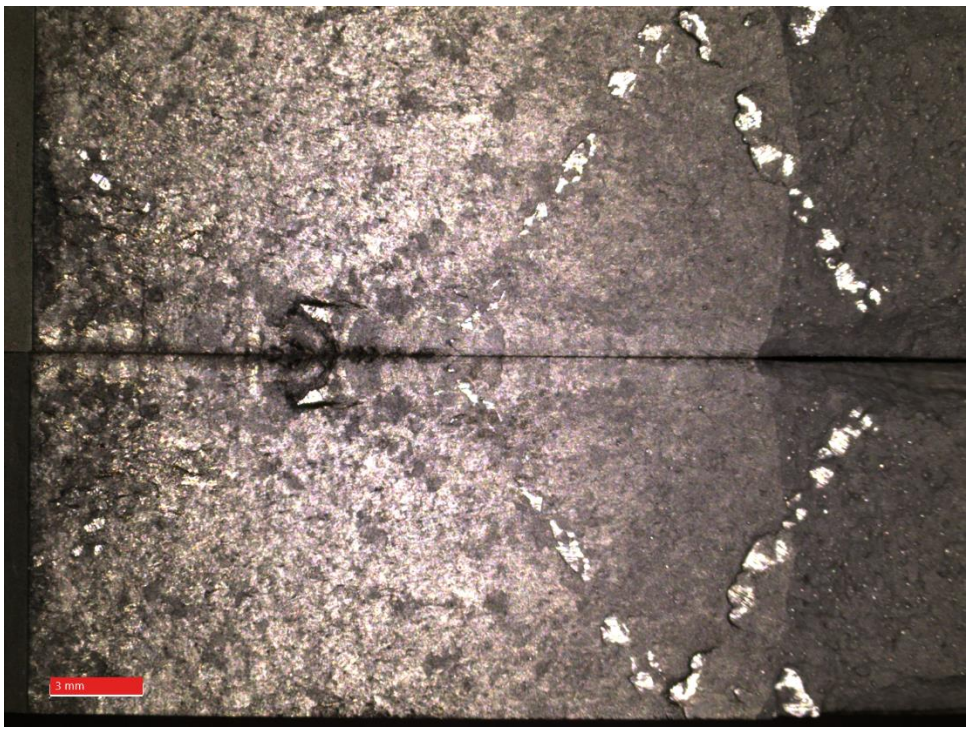

Figure 4-36 Fracture surface of 00T specimen

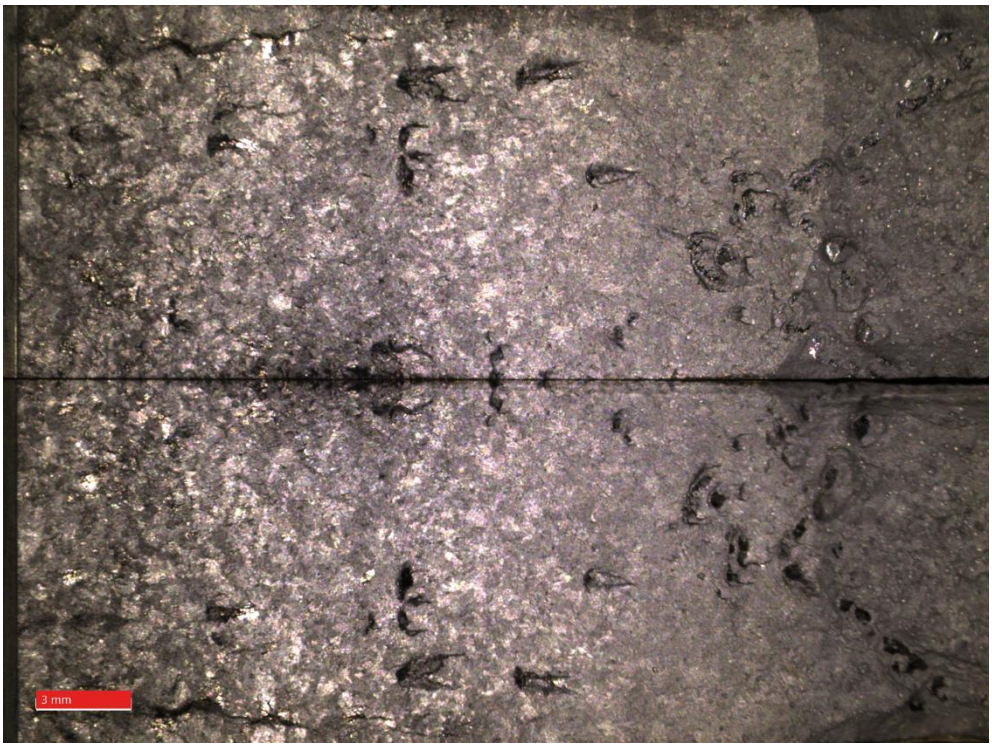

Figure 4-37 Fracture surface of 30 angle built specimen.

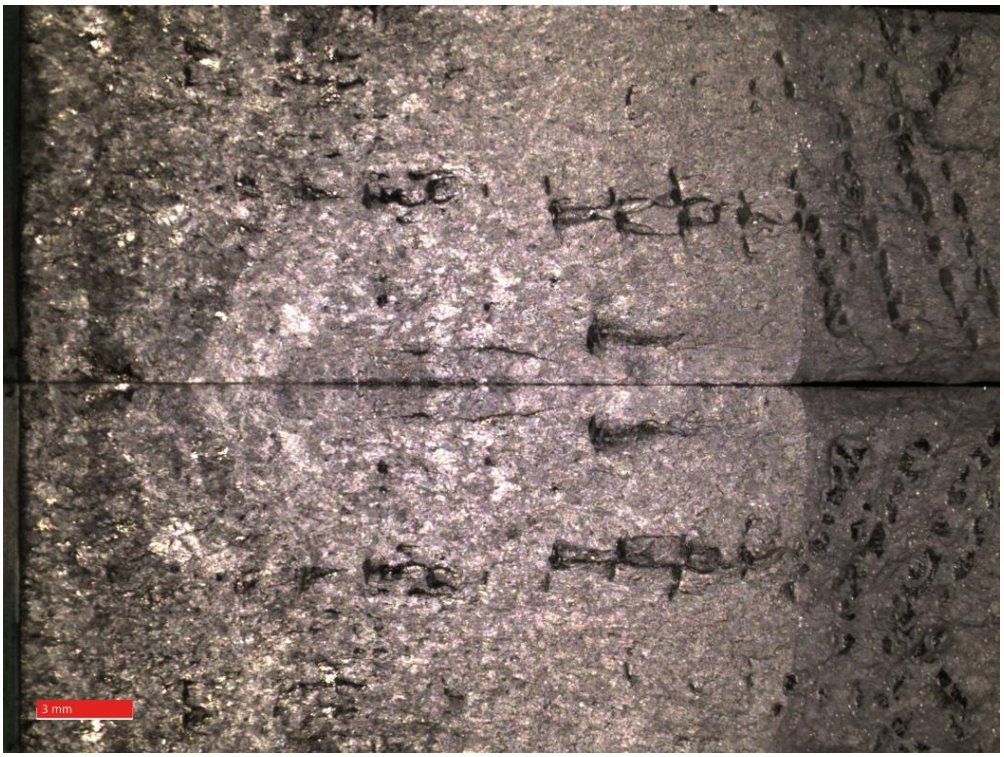

Figure 4-38 Fracture surface of 45T specimen

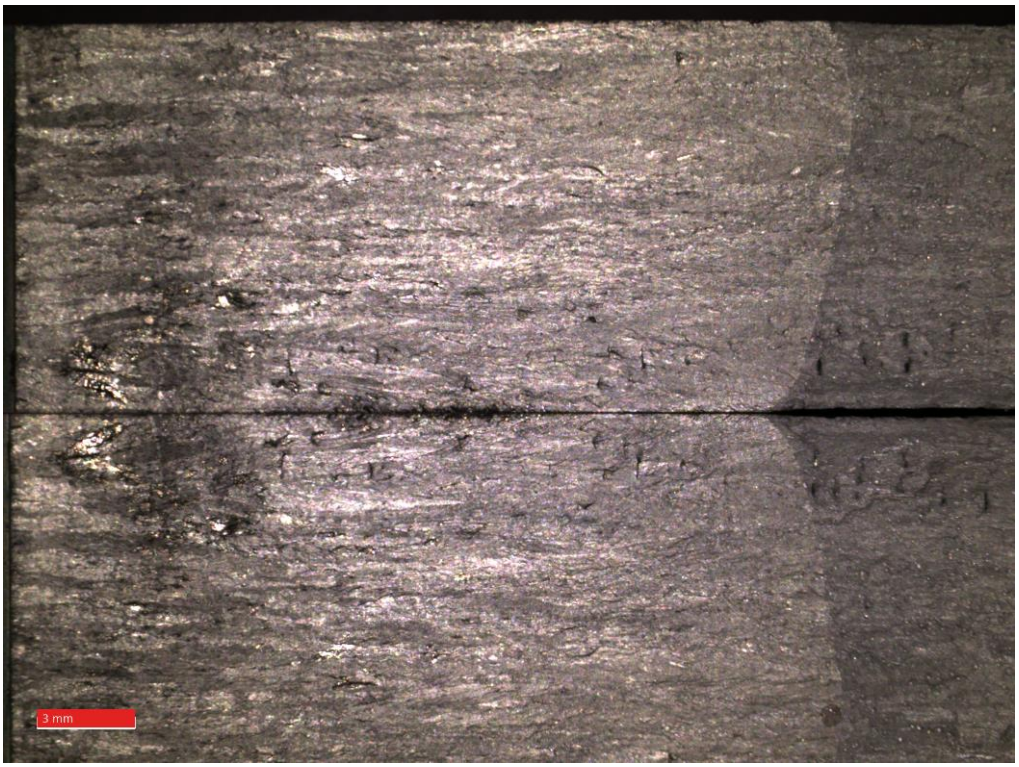

Figure 4-39 Fracture surface of 90T specimen

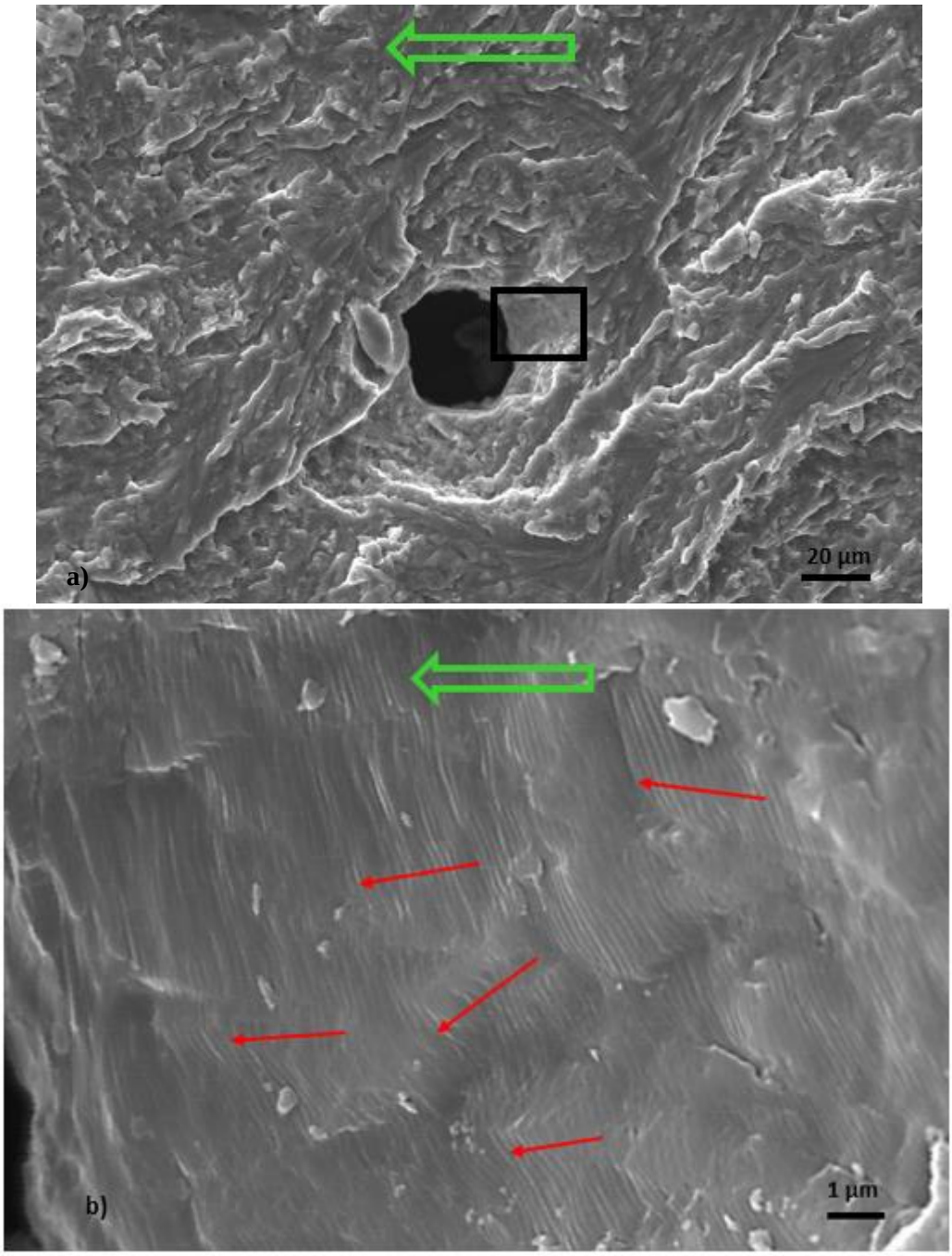

Figure 4-40. a) For 00T specimen, tear ridges and a void in which unmelted particles are b) Striations in edges of the void during Region 2, FCGR ≈ $2x10^{-4}$ mm/cycle (measured from photo). Red arrows indicate microcrack growth directions. Big green arrow indicates main crack growth direction.

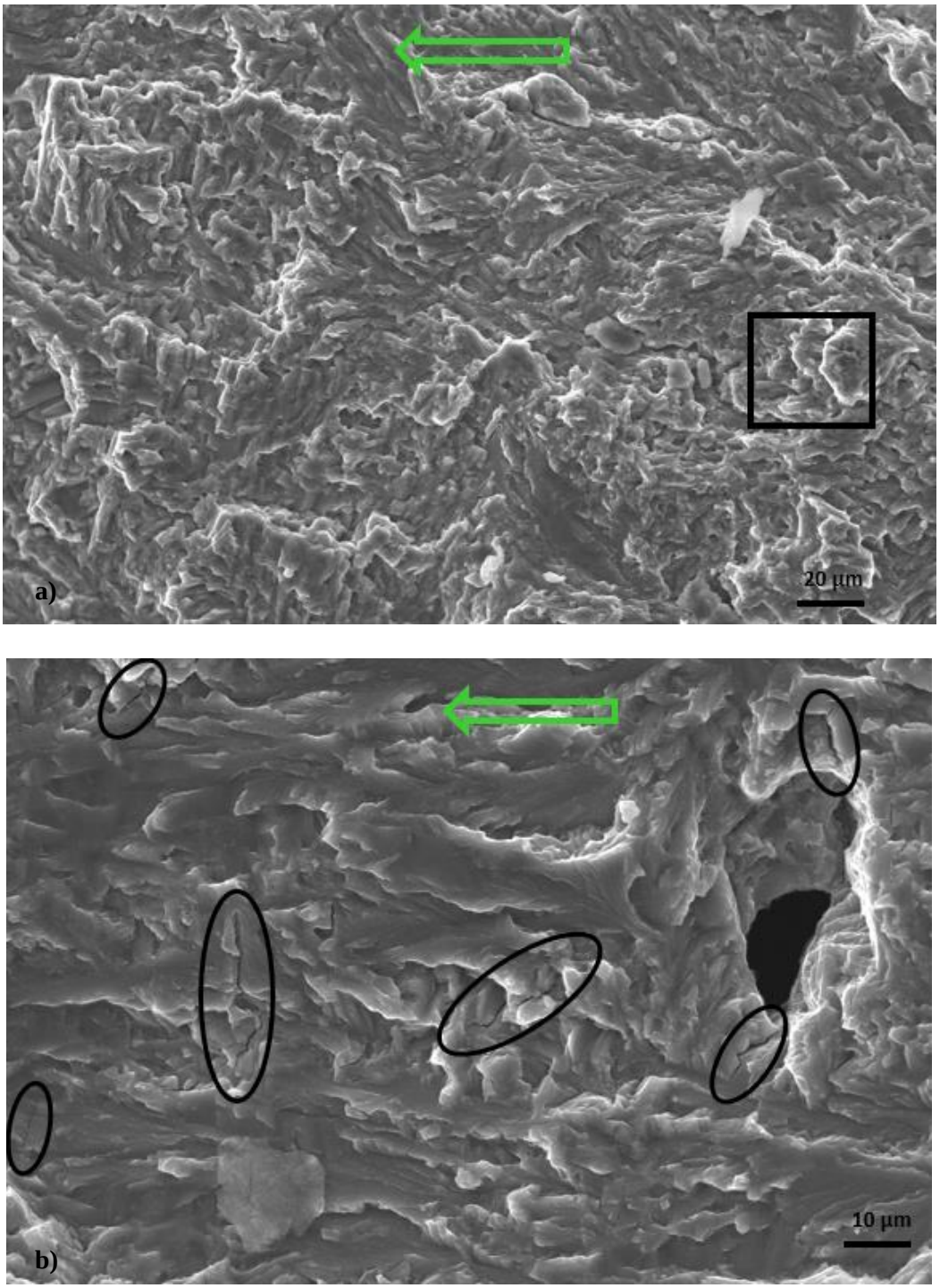

Figure 4-41. a) General SEM image of 30T specimen with coalescence of different crack propagation planes. b) Secondary cracks, tear ridges and a void on the black square area indicated in a). Black circles represent secondary cracks. Big green arrow indicates main crack growth direction.

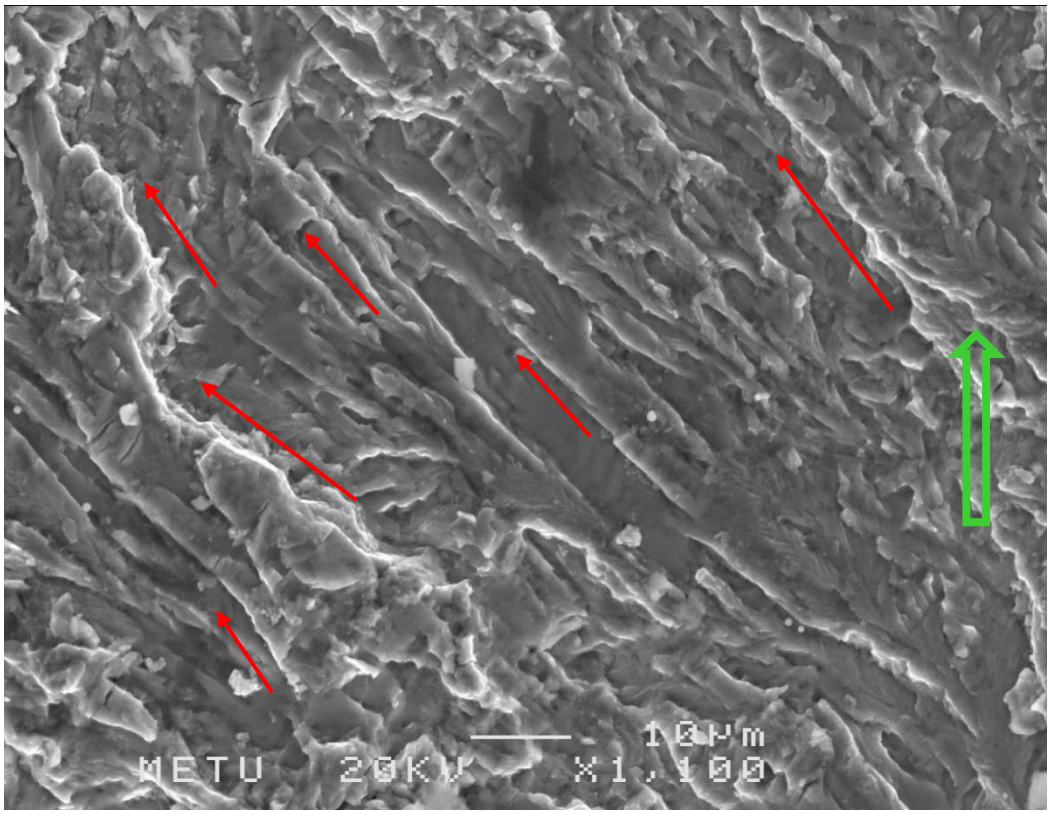

Figure 4-42 Typical tear ridges highlighted with red arrows at the precrack region of 30T specimen. Big green arrow indicates main crack growth direction.

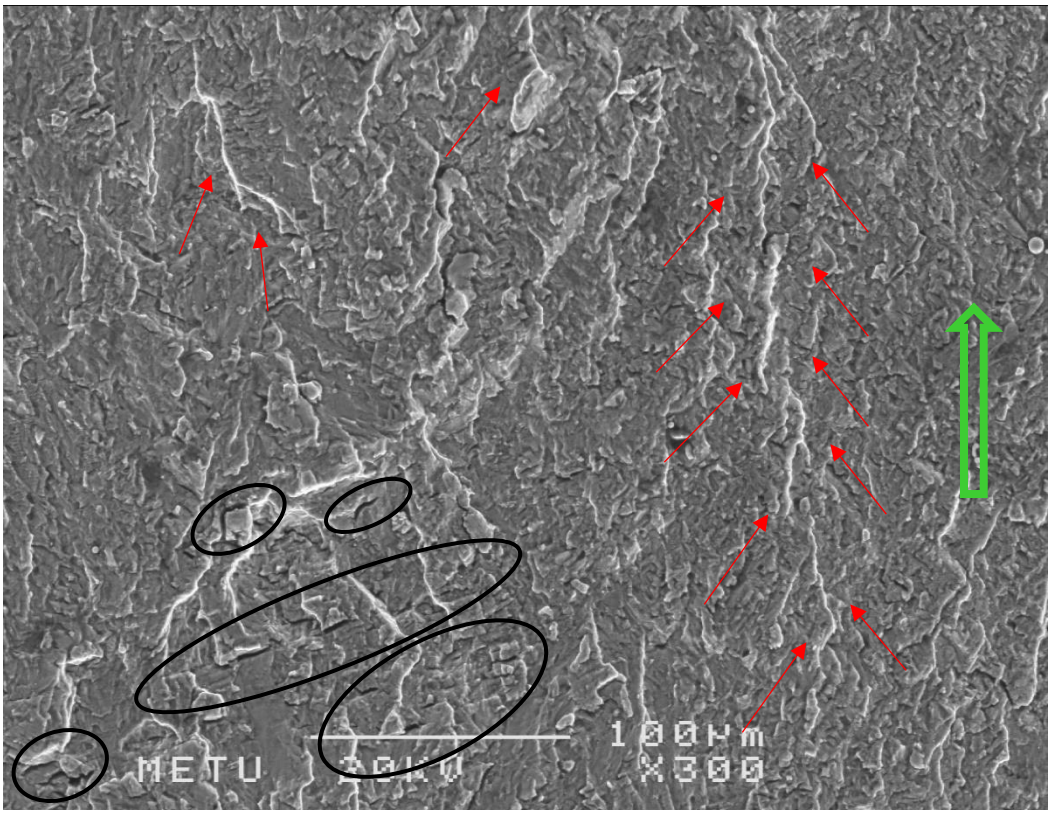

Figure 4-43 Secondary cracks marked with black circles parallel to each other 30T specimen. It is clear from the photo that tear ridges also show the propagating direction of crack by merging each other from bottom to top (See red arrows).Big green arrow indicates main crack growth direction.

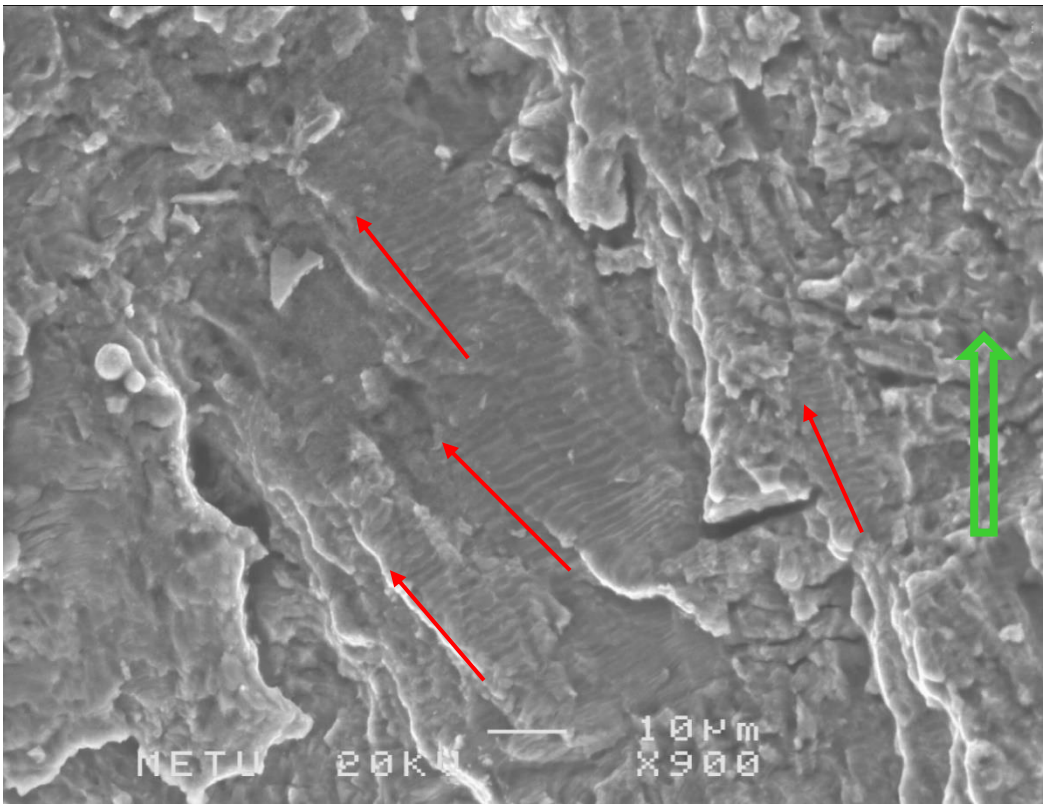

Figure 4-44 Fatigue striations perpendicular to crack growth direction for 30T specimen. Red arrows show the growth direction of local striations. Unmelted powders are also seen left of the image. Big green arrow indicates main crack growth direction.

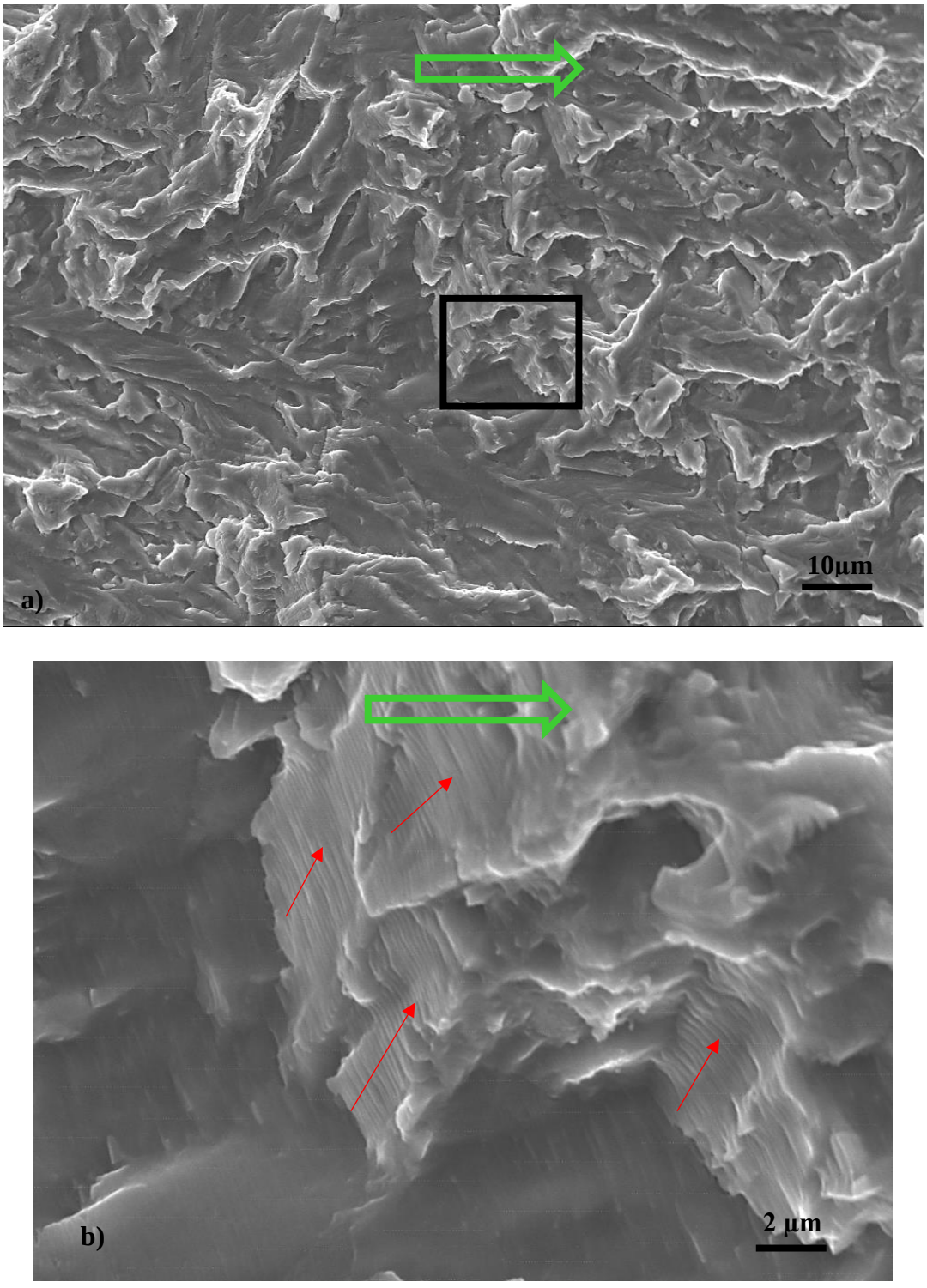

Figure 4-45. a) Fracture surface of 45T specimen. b) Looking at the black square in detail, striations and tear ridges during crack propagation with $2x10^{-4}$ mm/cycle (measured from SEM photo). Red arrows indicate local microcracks growing different planes. Big green arrow indicates main crack growth direction.

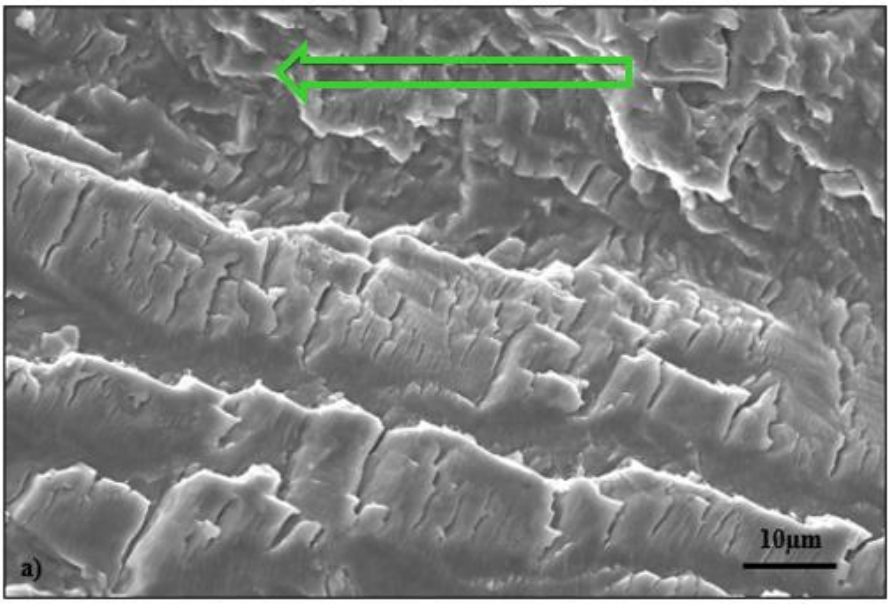

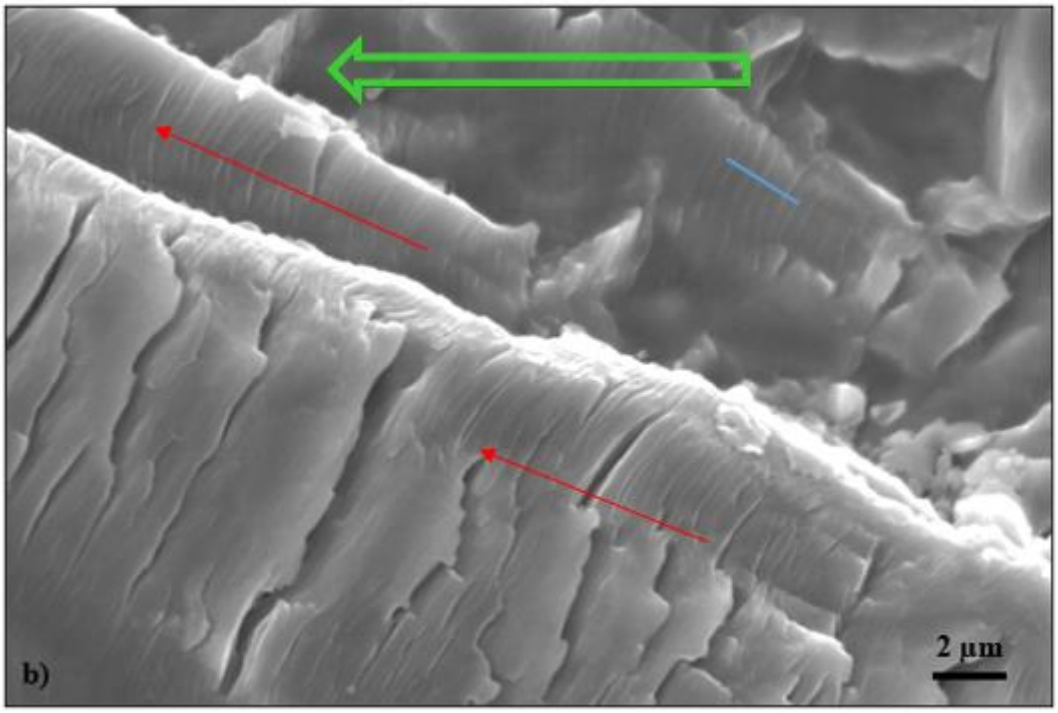

Figure 4-46 a) Tear ridges along with crack propagation direction in 90T. b) The close up observation of tear ridges on different planes and secondary cracks The formation of secondary cracks between fatigue striations is clearly visible in the SEM image. Red arrows highlight local cracks growing with FCGR ≈ $4x10^{-4}$ mm/cycle (measured by blue line indicated in the photo). Big green arrow indicates main crack growth direction.

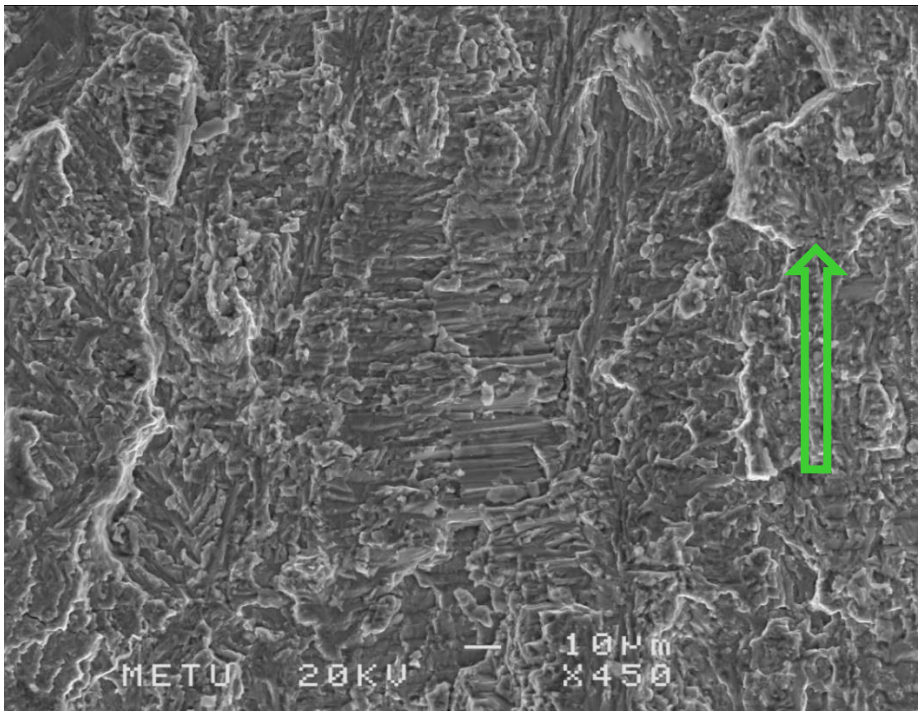

Figure 4-47 Typical fatigue appearance with different fracture planes at crack initiation regime for 90T specimen. Big green arrow indicates main crack growth direction.

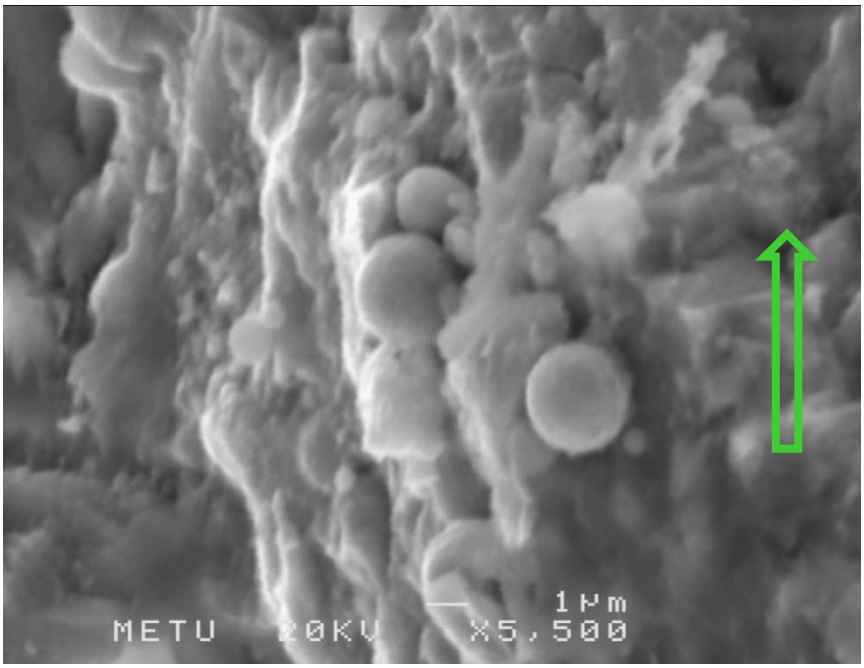

Figure 4-48 Unmelted powders at the precrack region for 90T sample. Big green arrow indicates main crack growth direction.

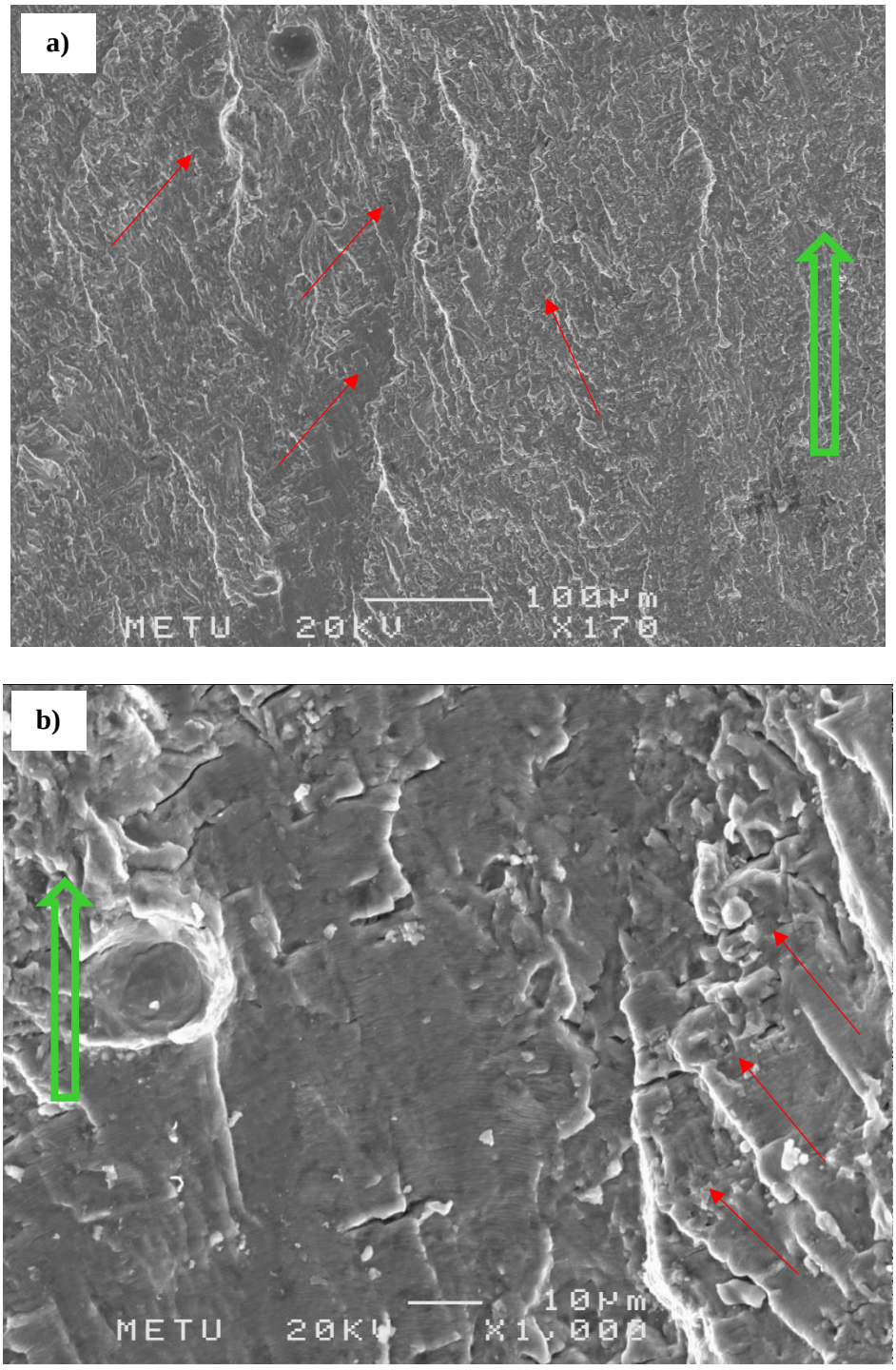

Figure 4-49 a) River pattern on the fracture surface almost 1,5 mm close to fast crack region of 90T. b) High magnification view of a). Secondary cracks perpendicular to crack growth direction and tear ridges parallel to crack growth direction. Red arrows indicate different microcrack directions. Big green arrow indicates main crack growth direction.

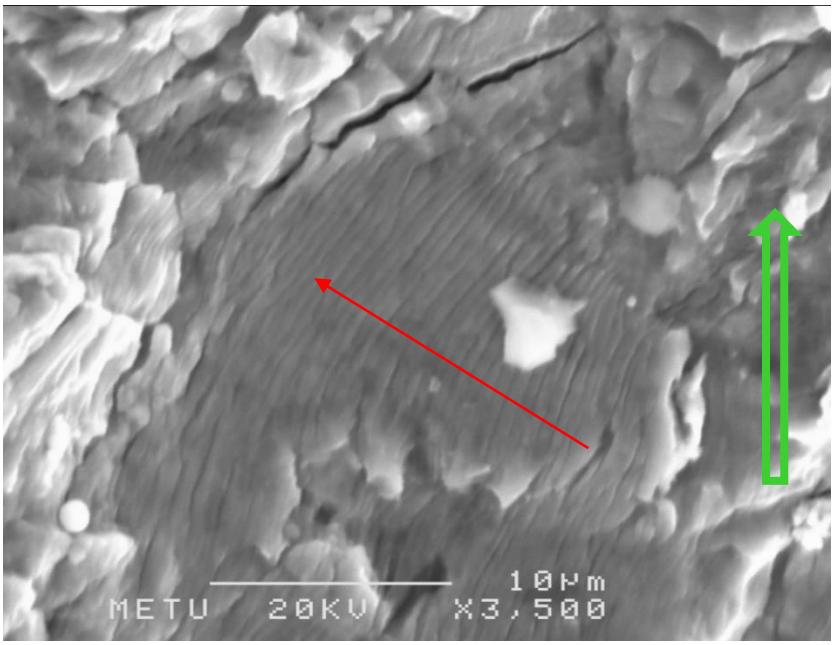

Figure 4-50 Fatigue striations and secondary cracks resulted from fatigue loading in the Paris region for 90T sample. Microcrack growth is shown by red arrow. Big green arrow indicates main crack growth direction.

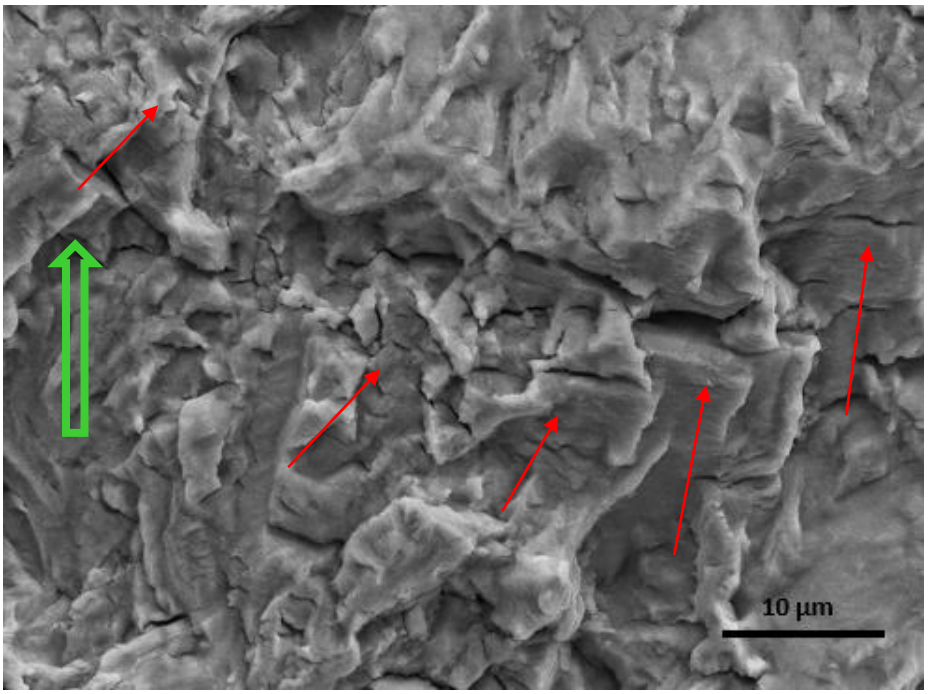

Figure 4-51. Fracture surface of 30T fracture tougness test specimen. Red arrows show the local micro striations at 4.05 kX magnification Big green arrow indicates main crack growth direction.

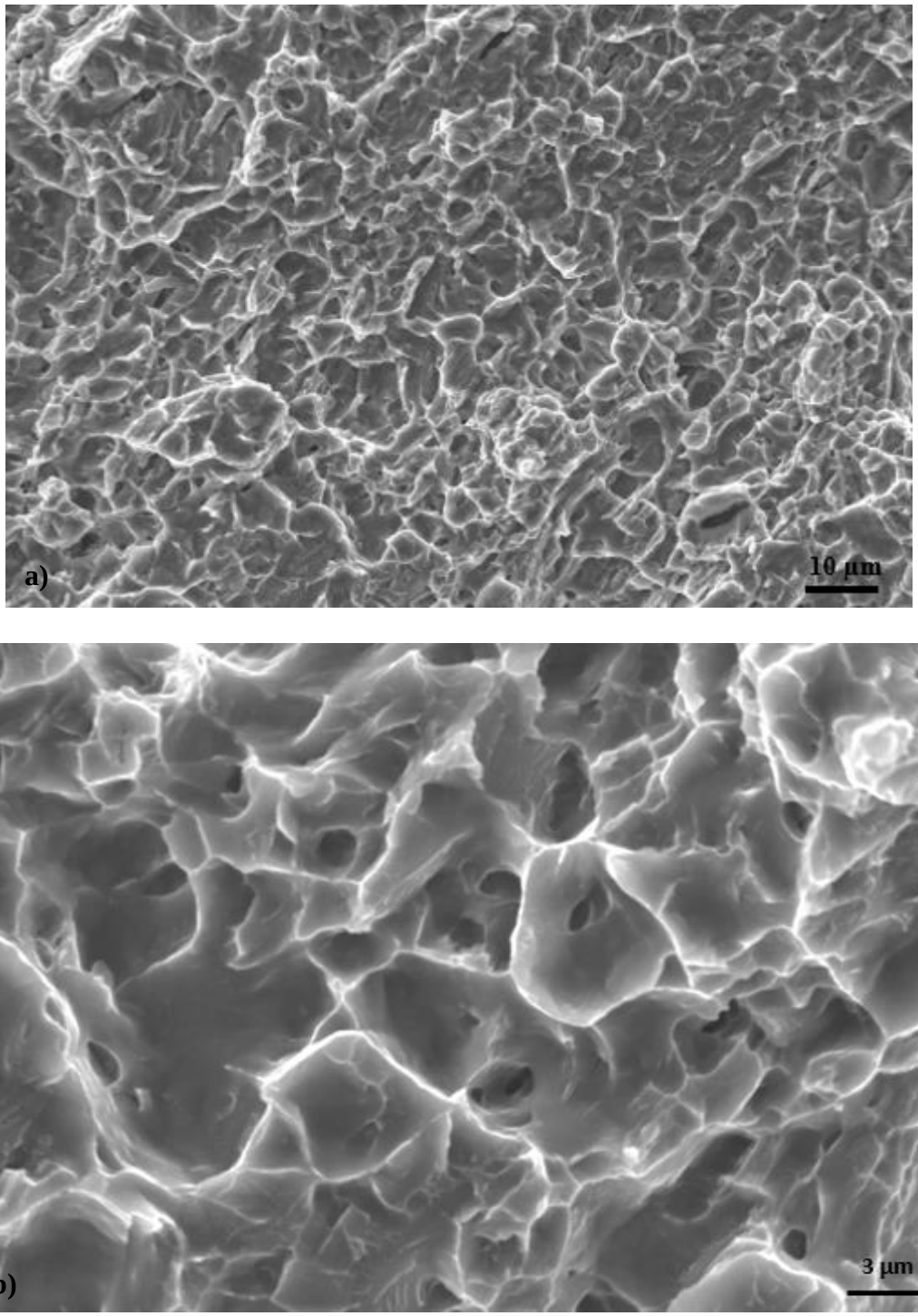

Figure 4-52. a) General view of fast crack growth region b) Dimples at 8 kX magnification

CHAPTER 5

CONCLUSION

In this study, the aim was to show the effect of build direction on crack growth behavior of Ti6Al4V fabricated by electron beam melting. From the conducted tests, following conclusions can be concluded;

- The mechanical properties including tension, fracture toughness and crack propagation of EBM processed specimens were comparable to conventioanlly produced Ti6Al4V. Microstructure morpholgy is consistent with literature studies.
- According to the tension results, 00T specimen has the highest tension strength and elongation whilst 30T specimen shows the lowest strength because of relatively larger unmelted regions on its fracture surface.
- Although the same process parameters was used in the layer by layer EBM production, different mechanical properties were investigated due to elongated microstructure in different direction.
- The shape of da/dN vs ΔK curves plotted for all four specimens are consistent with the graphs of the parts manufactured by the conventional method. The range of experimental C and m values is coherent with literature values. (for ductile materials $2<m<4$)
- Fracture toughness of 30T specimen is lower than that of other specimens and this is correlated with its faster crack propagation rate.
- 45T specimen has the lowest crack propagation based on its low porosity rate and its relatively high fracture toughness.
- In this study, a limited number of samples were tested and all of examinations should be conducted by using more specimens to obtain valid

and reliable results. Thicker compact tension samples for fracture toughness test should be examined.

Future Studies

- EBSD should be used to examine the microstructure mechanism such as growth direction and thickness of α and β phases.
- The effect of HIP (hot isostatic processing) or heat treatment on crack propagation behavior of EBM-Ti6Al4V parts should be also studied.
- The effect of oxygen concentration on mechanical properties of EBM-Ti6Al4V should be investigated due to the fact that oxygen may be resulted from powder production or storage conditions.
- To improve mechanical properties, process parameters should be enhanced by adjusting less layer thickness, by faster scanning, by increasing beam power or by increasing the scan depth. The range of powder particle size should be reduced to eliminate insufficient regions resulted from different size particles.
- The presence of process-induced defects in terms of location, shape and size should be taken into account to use produce additive manufacturing techniques for flight or fatique critical components.

REFERENCES

[1] Leyens C., Peters M. (2003). Titanium and Titanium Alloys: Fundamentals and Applications. Weinheim, Germany: Wiley-VCH.

[2] M.J. Donachie, Titanium - A Techinacal Guide, 2000.doi:10.5772/1844.

[3] Metallic Materials Properties Development and Standardization (MMPDS)-Chapter 5-Titanium

[4] M. Peters, J. Hemptenmacher, J. Kumpfert, C. Leyens, Structure and Properties of Titanium and Titanium Alloys, 2003.

[5] G.Terlinde, G. Fischer, O.F. Metallwerke, Beta Titanium Alloys, (2003).

[6] Ducato, A., Fratini, L., La Cascia, M., & Mazzola, G. (2013). An Automated Visual Inspection System for the Classification of the Phases of Ti-6Al-4V Titanium Alloy: Vol. 8048 LNCS (Issue PART 2). https://doi.org/10.1007/978-3-642-40246-3

[7] G. Welsch, R. Boyer, and E.W. Collings (1993). Materials Properties Handbook: Titanium Alloys. ASM International

[8] Pinke, P., Čaplovič, Ľ., & Kovács, T. (n.d.). The Influence Of Heat Treatment On The Mıcrostructure Of The Casted Ti6al4v Tıtanıum Alloy

[9] G. Lütjering, Influence of Processing on Microstructure and Mechanical Properties of (α+β) Titanium Alloys, Mater. Sci. Eng. A. 243 (2002) 32–45. doi:10.1016/s0921-5093(97)00778-8.

[10] J.C.M. Li, G. Lütjering, J.C. Williams, A. Gysler, Microstructure and Mechanical Properties of Titanium Alloys, in: Microstruct. Prop. Mater., 2000. doi:10.1142/9789812793959_0001.

[11] Gouge M, and Michaleris P. (Ed.) Thermo-Mechanical Modeling of Additive Manufacturing / Ch5: Microstructure and Mechanical Properties of AM Builds, 2018 Elsevier Inc

[12] Materials Properties Handbook: Titanium Alloys. (1994). ASM International.

[13] *ASTM F2792 - 12a Standard Terminology for Additive Manufacturing Technologies' (Withdrawn 2015)*. (n.d.). Retrieved August 11, 2021, from https://www.astm.org/Standards/F2792.htm

[14] M.M. Cotteleer, Mark, Jonathan Holdowsky, J. C. (2014). 3D opportunity in Aerospace and Defense. *A Deloitte Ser. Addit. Manuf.*, 1–28. https://www2.deloitte.com/us/en/insights/focus/3d-opportunity/additive-manufacturing-3d-opportunity-in-aerospace.html

[15] Zenou, M., & Grainger, L. (2018). *3 - Additive manufacturing of metallic materials*. https://doi.org/10.1016/B978-0-12-812155-9.00003-7

[16] Utela, B., Storti, D., Anderson, R., & Ganter, M. (2008). A review of process development steps for new material systems in three dimensional printing (3DP). *Journal of Manufacturing Processes*, *10*(2), 96–104. https://doi.org/10.1016/J.JMAPRO.2009.03.002

[17] Thompson, S. M., Bian, L., Shamsaei, N., & Aref Yadollahi. (2015). An overview of Direct Laser Deposition for additive manufacturing; Part I: Transport phenomena, modeling and diagnostics. *Additive Manufacturing*, *8*, 36–62. https://doi.org/10.1016/j.addma.2015.07.001

[18] Fousová, M., Vojtěch, D., Doubrava, K., Daniel, M., & Lin, C. F. (2018). Influence of inherent surface and internal defects on mechanical properties of additively manufactured Ti6Al4V alloy: Comparison between selective laser melting and electron beam melting. *Materials*, *11*(4). https://doi.org/10.3390/ma11040537

[19] Liu, Y., Yang, Y., & Wang, D. (n.d.). *A study on the residual stress during selective laser melting (SLM) of metallic powder*. https://doi.org/10.1007/s00170-016-8466-y

[20] Herzog, D., Seyda, V., Wycisk, E., & Emmelmann, C. (2016). *Additive manufacturing of metals*. https://doi.org/10.1016/j.actamat.2016.07.019

[21] Gokuldoss, P. K., Kolla, S., & Eckert, J. (2017). Additive Manufacturing Processes: Selective Laser Melting, Electron Beam Melting and Binder

Jetting—Selection Guidelines. *Materials*, *10*(6). https://doi.org/10.3390/MA10060672

[22] "About Arcam | GE Additive." https://www.ge.com/additive/who-we-are/about-arcam (accessed Aug. 14, 2021)

[23] Liu, S., & Shin, Y. C. (2019). Additive manufacturing of Ti6Al4V alloy: A review. *Materials and Design*, *164*, 107552. https://doi.org/10.1016/j.matdes.2018.107552

[24] Edwards, P., O'Conner, A., & Ramulu, M. (2013). Electron beam additive manufacturing of titanium components: Properties and performance. *Journal of Manufacturing Science and Engineering, Transactions of the ASME*, *135*(6). https://doi.org/10.1115/1.4025773

[25] Hrabe, N., & Quinn, T. (2013). Effects of processing on microstructure and mechanical properties of a titanium alloy (Ti-6Al-4V) fabricated using electron beam melting (EBM), Part 2: Energy input, orientation, and location. *Materials Science and Engineering A*, *573*, 271–277. https://doi.org/10.1016/j.msea.2013.02.065

[26] Wysocki, B., Maj, P., Sitek, R., Buhagiar, J., & Jan Kurzydłowski, K. (n.d.). *Laser and Electron Beam Additive Manufacturing Methods of Fabricating Titanium Bone Implants*. https://doi.org/10.3390/app7070657

[27] Rafi, H. K., Karthik, N. V., Gong, H., Starr, T. L., & Stucker, B. E. (2013). Microstructures and mechanical properties of Ti6Al4V parts fabricated by selective laser melting and electron beam melting. *Journal of Materials Engineering and Performance*, *22*(12), 3872–3883. https://doi.org/10.1007/s11665-013-0658-0

[28] Hayes, B. J., Martin, B. W., Welk, B., Kuhr, S. J., Ales, T. K., Brice, D. A., Ghamarian, I., Baker, A. H., Haden, C. V., Harlow, D. G., Fraser, H. L., & Collins, P. C. (2017). Predicting tensile properties of Ti-6Al-4V produced via directed energy deposition. *Acta Materialia*, *133*, 120–133. https://doi.org/10.1016/j.actamat.2017.05.025

[29] Chern, A. H., Nandwana, P., Yuan, T., Kirka, M. M., Dehoff, R. R., Liaw, P. K., & Duty, C. E. (2019). A review on the fatigue behavior of Ti-6Al-4V fabricated by electron beam melting additive manufacturing. *International Journal of Fatigue*, *119*(August 2018), 173–184. https://doi.org/10.1016/j.ijfatigue.2018.09.022

[30] Seifi, M., Dahar, M., Aman, R., Harrysson, O., Beuth, J., & Lewandowski, J. J. (2015). Evaluation of Orientation Dependence of Fracture Toughness and Fatigue Crack Propagation Behavior of As-Deposited ARCAM EBM Ti-6Al-4V. *JOM*, *67*(3), 597–607. https://doi.org/10.1007/S11837-015-1298-7

[31] Edwards, P., & Ramulu, M. (2015). Effect of build direction on the fracture toughness and fatigue crack growth in selective laser melted Ti-6Al-4-‰V. *Fatigue and Fracture of Engineering Materials and Structures*, *38*(10), 1228–1236. https://doi.org/10.1111/FFE.12303

[32] Lewandowski, J. J., & Seifi, M. (2016). *Metal Additive Manufacturing: A Review of Mechanical Properties*. https://doi.org/10.1146/annurev-matsci-070115-032024

[33] Svensson M. 2009. Ti6Al4V manufactured with electron beam melting (EBM): mechanical and chemical properties. In Proceedings from the Materials & Processes for Medical Devices Conference, pp. 189–94. Novelty, OH: ASM Int

[37] G.E.Dieter, “Mechanical Metallurgy”, McGraw Hill, (1988)

[38] Additive Manufacturing for Implants and Aerospace, EBM. (n.d.). Retrieved from http://www.arcam.com/

[39] Körner, C. (2016). Additive manufacturing of metallic components by selective electron beam melting - A review. *International Materials Reviews*, *61*(5)

[40] Everhart, W., Dinardo, J., & Barr, C. (n.d.). *The Effect of Scan Length on the Structure and Mechanical Properties of Electron Beam-Melted Ti-6Al-4V*. https://doi.org/10.1007/s11661-016-3866-z

[41] Klassen, A., Forster, V. E., Juechter, V., & Körner, C. (2017). Numerical

simulation of multi-component evaporation during selective electron beam melting of TiAl. Journal of Materials Processing Technology, 247, 280-288. doi:10.1016/j.jmatprotec.2017.04.016

[42] https://kyocera-sgstool.co.uk/titanium-resources/titanium-information-everything-you-need-to-know/ti-6al-4v-grade-5-titanium-alloy-data-sheet/#:~:text=Properties%20of%20Grade%205%20titanium,density%20of%204.43%20g%2Fcc.

[43] ASTM E8 -Standard Test Methods for Tension Testing of Metallic Materials

[44] ASTM E647-11 Standard Test Method for Measurement of Fatigue Crack Growth Rates

[45] ASTM E399-09ε2 Standard Test Method for Linear-Elastic Plane-Strain Fracture Toughness KIc of Metallic Materials

APPENDICES

A. 00T Specimen -CT results

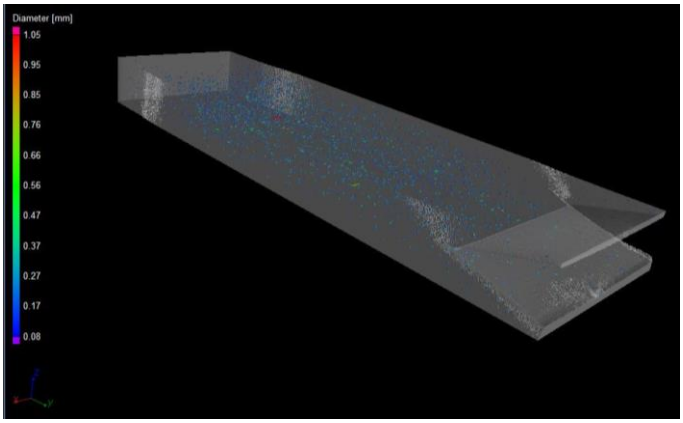

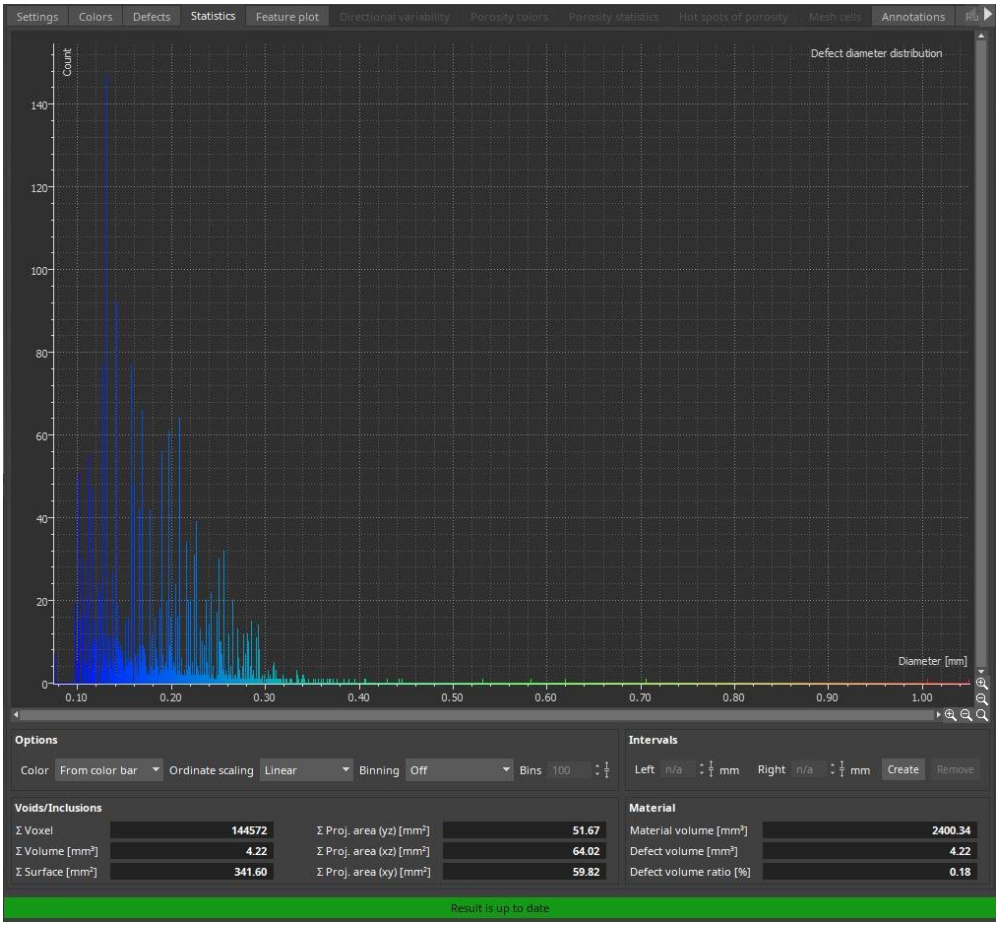

B. 30T Specimen-CT Results

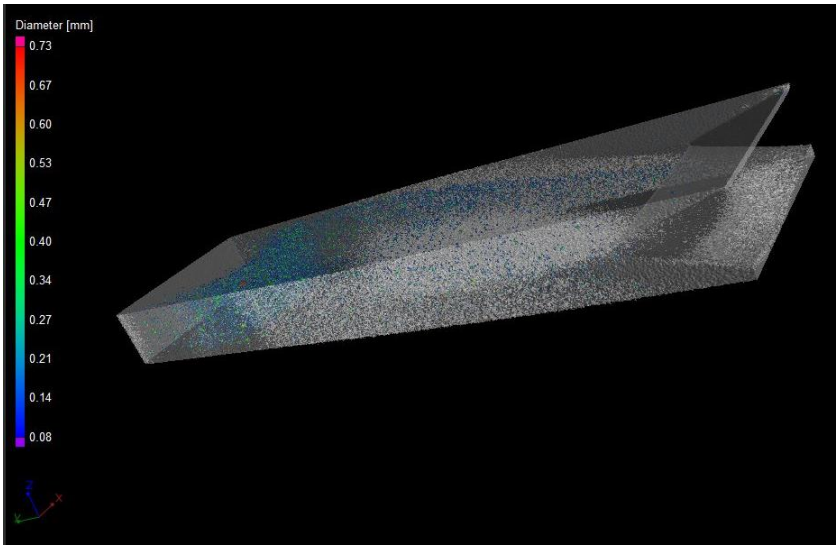

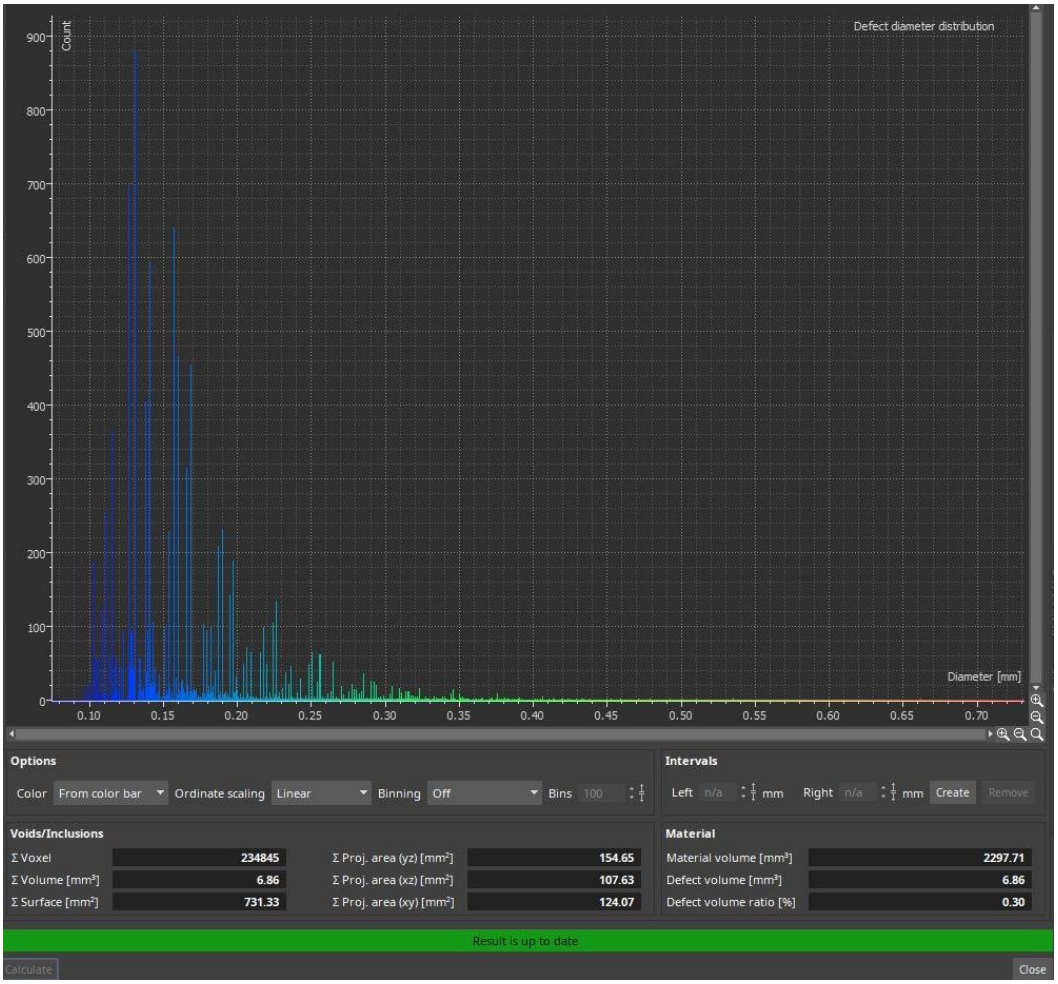

C. 45T Specimen-CT Results

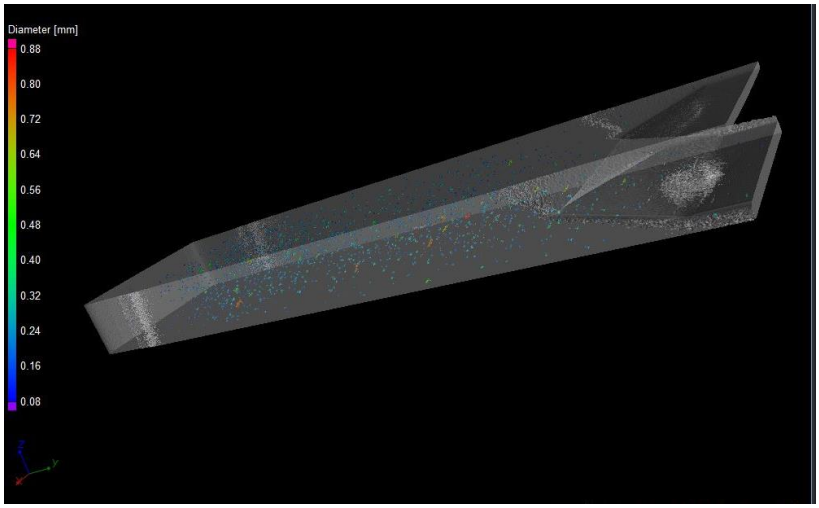

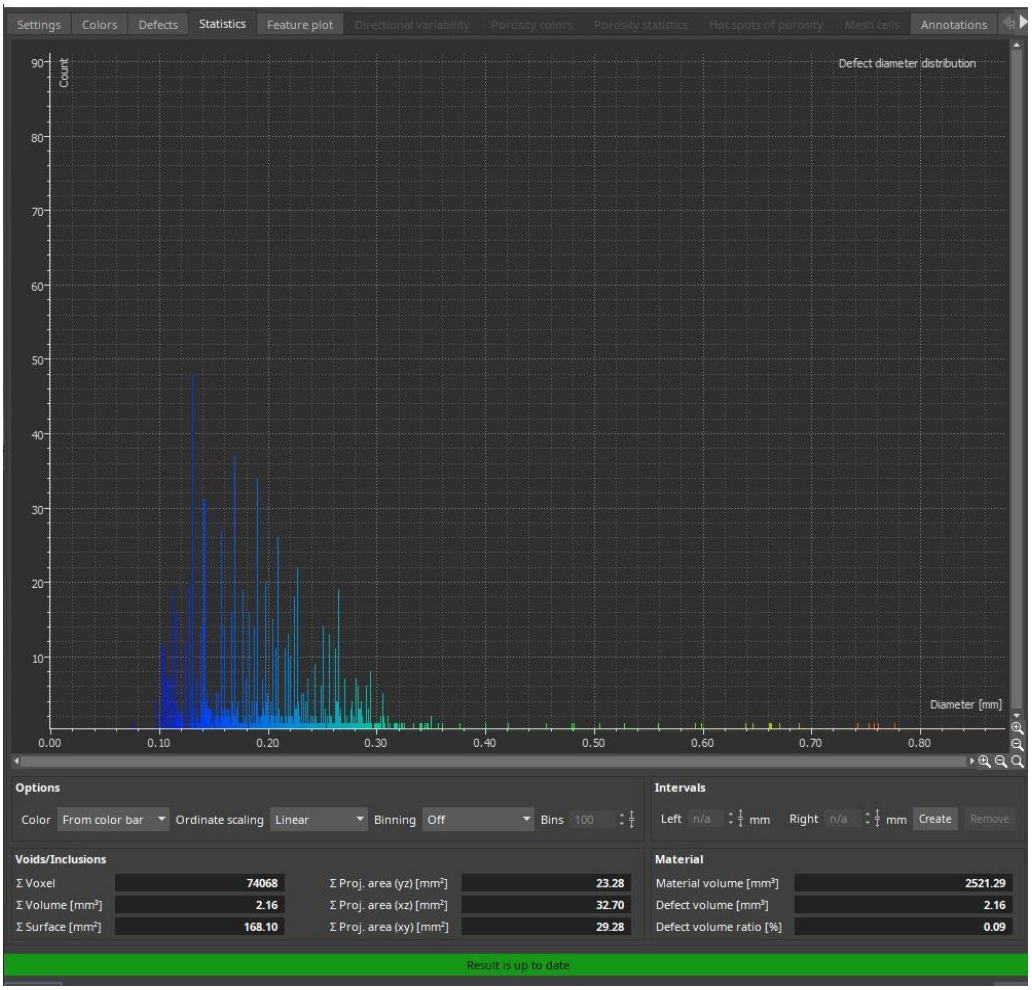

D. 90T Specimen-CT Results